# Synthetic Optimization and Electrochemical Studies of Delafossite $CuCrO_2$ for Solar Energy Conversion and Storage Applications

by

Amanda Leigh Chown

A dissertation submitted to the Graduate Faculty of
Auburn University
in partial fulfillment of the
requirements for the Degree of
Doctor of Philosophy

Auburn, Alabama
August 6, 2022

Keywords: Electrochemistry, Delafossite $CuCrO_2$, Electrochemical Impedance Spectroscopy, Hydrothermal Synthesis, Li-ion Batteries, Solar Cell Devices

Approved by

Dr. Byron H. Farnum, Chair, Assistant Professor Department of Chemistry
Dr. Christian R. Goldsmith, Professor Department of Chemistry
Dr. David Stanbury, Professor Emeritus Department of Chemistry
Dr. Ryan Comes, Assistant Professor Department of Physics
Dr. Majid Beidaghi, Associate Professor, Department of Mechanical Engineering

# Abstract

Metal oxides have been of great importance to the development of new energy conversion and storage technologies including heterojunction solar cells and Li-ion batteries. P-type delafossite $CuCrO_2$ is a metal oxide which is of interest for such applications due to its wide band gap and relatively high valence band edge. However, defects in p-type materials result in poor performance for solar cell devices compared to alternative metal oxides due to inferior charge separation at the metal oxide interface as well as possible increases in electron hole recombination. On the other hand, reports have been made on defect-induced $CuCrO_2$ having improved performance for ion battery application due to increased hole density, higher conductivity, and faster charge extraction which can improve ion intercalation. Researching the fundamental electrochemical properties of $CuCrO_2$ and the effects defects can have on those properties can aid in understanding the impact of surface states as recombination centers and redox capabilities, and how solar cell and battery applications can be impacted.

Electrochemical impedance spectroscopy (EIS) is one of the most utilized methods to characterize these electrodes in the context of energy applications. The utility of EIS stems from its ability to differentiate multiple interfaces (i.e. solid/electrolyte, solid/solid) within devices based on their frequency response to a modulated potential and the subsequent decoupling of resistive and capacitive circuit components. In ***Chapter 2***, examples are covered from the literature where EIS has been particularly important in the understanding of electronic properties related to metal oxide electrodes within energy storage devices, specifically ion batteries

Previous $CuCrO_2$ studies used a hydrothermal synthetic route which commonly leads to byproduct formation, making electrochemical characterization challenging. An important aspect

of this work is the consideration of $Cr^{3+}$ as the reductant used to reduce $Cu^{2+}$ to $Cu^{+}$, discussed in ***Chapter 3***. This was confirmed by detection and quantification of $CrO_4^{2-}$ as a product of hydrothermal synthesis in addition to the fact that $CuCrO_2$ purity was maximized at a ratio of 4:3 Cr:Cu, consistent with the proposed stoichiometric reaction: $4Cr^{3+} + 3Cu^{2+} + 20\ OH^{-} \rightarrow 3CuCrO_2 + CrO_4^{2-} + 10\ H_2O$. Using a 4:3 ratio of Cr:Cu starting materials and allowing the synthesis to proceed for 60 hours eliminates the presence of CuO beyond detection by powder X-ray diffraction (pXRD). Furthermore, washing the solid product in 0.5 M $NH_4OH$ removes $Cu_2O$ and $Cr_2O_3$ impurities, leaving behind the isolated $CuCrO_2$ product as confirmed using powder X-ray diffraction and inductively coupled plasma mass spectrometry (ICP-MS).

In ***Chapter 4***, $CuCrO_2$ was used to fabricate mesoporous thin films to study its electrochemical properties, where a strong $Li^{+}$ dependence was observed. A shift in $Cu^{2+/+}$ redox $E_{1/2}$ was observed as $[Li^{+}]$ in the electrolyte was increased from 0.03 V to 0.14 V vs $Fc^{+}$, in addition to the growth of a new redox feature at $E_{1/2} = -0.43$ V vs $Fc^{+/0}$, attributed to $Li^{+}$ occupation in $Cu^{+}$ vacancy sites and the ability for $Li^{+}$ to affect the Helmholtz layer due to increased surface charge. A 4% $Cu^{+}$ deficiency was determined by ICP-MS. Based on chronoamperometry experiments in which a series of electrolyte solutions were used, the growth in surface charge as $[Li^{+}]$ in electrolyte increased fit to a Langmuir binding isotherm where an equilibrium constant K was determined to be 0.057 $M^{-1}$ and a maximum surface charge of 15.5 mC. An increase in the surface charge from chronoamperometry as well as current from cyclic voltammetry as $[Li^{+}]$ increases is also observed. Comparing these results to those of $CuGaO_2$ films in which the aspect ratio is larger and the particles preferentially stack in which terminal redox active Cu–O is less exposed compared to those in $CuCrO_2$, it is conclusive that the morphology of delafossite particles plays an important role in electrochemical performance. Chronopotentiometry experiments on $CuCrO_2$ reveal a 7.8

mA h $g^{-1}$ charge capacity at cycle 2, but with a % cycling efficiency from 83% to 91% over 10 cycles. This and multiple cycling cyclic voltammetry (CV) experiments reveal the degradative behavior of the film, which was found to be related to the loss of Li-coupled redox activity. Nonetheless, the significant increase in surface charge and capacity with increased $Li^+$ can be used to further our understanding of surface defects and their effect on hole recombination in solar cell devices, as well as how $Li^+$ occupies surface sites for electrochemical energy storage application.

Finally, ***Chapter 5*** provides insight into future research directions based on conclusions drawn from previous chapters. An emphasis is made on preliminary results in which $CuCrO_2$ powder is washed in a pH 1 HCl solution to study the resulting electrochemical properties. Acid washing $CuCrO_2$ films for 12 – 336 hours was shown to lead to consistent increases in both surface charge and capacities compared to their base washed counterpart, with films made from $CuCrO_2$ washed for 96 hours lead to overall optimal electrochemical performance. These results are related to possible $Cu^+$ induced vacancies and morphological changes in the particles. Other interesting topics in ***Chapter 5*** include but are not limited to effects of varying the cation source in electrolyte solution, morphological changes, and doping, on the resulting electrochemical properties and stability of $CuCrO_2$.

# Acknowledgments

First, I would like to thank my dissertation committee. With your feedback and guidance throughout my graduate career, I have had a rewarding experience at Auburn University. Special thanks to each committee member for constructive intellectual conversations and feedback throughout the years. You have all made it possible for me to have a rewarding and successful graduate experience.

To Dr. Farnum, words cannot encompass how much you have been an exceptional mentor and PI through my time at Auburn. You have taught me what it means to be a great professor, scholar, and supervisor. You have taught me to push my own boundaries, and most importantly, you believed in me at times I did not believe in myself. Without you I truly could not have made it this far.

To my family, friends, and colleagues, thank you for supporting me through my time as a student both at Florida State and Auburn. A special thanks to my parents for all your unconditional love and words of encouragement. To former Farnum lab member and friend Alex Bredar, your advice and feedback through the years have been of immeasurable value and I will always look up to you as both a good friend and role model.

Finally, to my fiancée and best friend Kyle Musgrove, you have played a pivotal role in challenging me to be the best version of myself I can be in every aspect of my life. Your support and love have made these final years at Auburn priceless.

# Table of Contents

# List of Tables

## List of Figures

# List of Abbreviations

## *List of Analytical Instruments/Experiments*

| | |
|---|---|
| ATR-IR | Attenuated Total Reflectance Infrared Spectroscopy |
| CV | Cyclic Voltammetry |
| EDS | Energy Dispersive Spectroscopy |
| EIS | Electrochemical Impedance Spectroscopy |
| FTIR | Fourier-Transform Infrared Spectroscopy |
| HAADF | High Angle Annular Dark Field |
| HRTEM | High Resolution Transmission Electron Microscopy |
| ICP-MS | Inductively Coupled Plasma Mass Spectroscopy |
| MBE | Molecular Beam Epitaxy |
| pXRD | Powder X-ray Diffraction |
| SAED | Selected Area Electron Diffraction |
| SEM | Scanning Electron Microscopy |
| TEM | Transmission Electron Microscopy |
| TGA | Thermal Gravimetric Analysis |
| UV-vis | Ultraviolet-visible Spectroscopy |
| XPS | X-ray Photoelectron Spectroscopy |
| XRD | X-ray Diffraction |

## *List of Units*

| | |
|---|---|
| ° | Degree |
| $2\theta$ | The angle between the transmitted and reflected beam |

| | |
|---|---|
| A | Amp |
| a.u. | Arbitrary Units |
| C | Celsius; Coulomb |
| cP | Centipoise |
| eV | Electronvolt |
| g | gram |
| h | Hour |
| Hz | Hertz |
| J | Joule |
| K | Kelvin |
| L | Liter |
| M | Molar (moles $L^{-1}$) |
| m | Meter |
| mA h $g^{-1}$ | Specific Capacity |
| mol | Mole |
| ppb | parts per Billion |
| rpm | Revolutions per Minute |
| TW | Terawatts |
| V | Potential; Volt |
| $V_{OC}$ | Open Circuit Potential |
| Ω | Ohm |

***List of Terms***

| | |
|---|---|
| [ ] | Concentration (M) |
| A | Planar Electrode |
| AC | Alternating Current |
| An | Anode |
| C | Capacitance; Charge Rate |
| $C_0^*$ | Initial Concentration of the Analyte |
| Cat | Cathode |
| CE | Counter Electrode |
| $C_{int}/Q_1$ | Interfacial Capacitance |
| CPE | Constant Phase Element |
| $D_0$ | Diffusion Coefficient of the Analyte |
| DC | Direct Current |
| DSSCs | Dye-Sensitized Solar Cells |
| E | Modulated Potential |
| $e^-$ | Electron |
| $E_{1/2}$ | Half Wave Potential |
| $E_a$ | Activation Energy |
| $E_a/E_{pa}$ | Anode Potential/Anodic Peak Potential |
| $E_c/E_{pc}$ | Cathode Potential/Cathodic Peak Potential |
| F | Faradays Constant |
| $(\Delta)G$ | Change in Free Energy |
| I | Current Response |

| | |
|---|---|
| i | Current |
| IT | Current as a Function of Time |
| J-V | Current Density as a Function of Potential |
| K | Equilibrium Constant |
| k | Boltzmann Constant |
| $M_W$ | Molecular Weight |
| n | Number of Electrons |
| $nFA\Gamma_0/Q_{ads}$ | Adsorption Charge |
| NHE | Normal Hydrogen Electrode |
| PDF | Powder Diffraction File |
| pH | Potential Hydrogen |
| Q | Charge |
| $Q_{ads}$ | Adsorption Charge |
| $Q_{dl}$ | Double Layer Charge |
| $Q_{max}$ | Maximum Surface Charge |
| R | Resistance |
| R\|\|C | Parallel Circuit |
| $R_{ct}/R_1$ | Charge Transfer Resistance |
| RE | Reference Electrode |
| $R_s$ | Solution Resistance |
| $R_{sl}/C_{sl}$ | Surface Layer Formation |
| SCE | Saturated Calomel Electrode |
| SEI | Solid Electrolyte Interface |

| | |
|---|---|
| SHE | Standard Hydrogen Electrode |
| SI | Supplemental Information |
| T | Absolute Temperature |
| t | Time |
| TOSs | Transparent Oxide Semiconductors |
| WE | Working Electrode |
| wt. % | Weight Percent |
| Z or \|Z\| | Impedance |
| $Z_{Im}$ | Imaginary Component of Impedance |
| $Z_{Re}$ | Real Component of Impedance |
| σ | A term which describes the resistance associated with diffusion as a function of concentration of charge carriers and their diffusion coefficients |
| τ | Transition Time |
| υ | Scan Rate |
| φ | Phase Angle |
| χCr | Mole Fraction of Chromium |
| ω | Frequency |
| ω/ $Z_W$ | Warburg Impedance |

# Chapter 1

# An Introduction to Solar Energy Conversion and Storage, Metal Oxide Electrodes, and Electrochemical Techniques

## *1.1 Solar Energy Conversion and Storage*

The use of renewable energy sources is of interest due to the increase in world energy consumption. Predictions suggest global energy demands will reach 28 TW terawatts (TW) by 2050 and 46 TW of energy in 2100, which is over 2.5 times more energy than was consumed in 2016.[1] Additionally, a majority of energy is derived from fossil fuels with a small percentage of energy used being harvested by renewable sources. Both the increase in energy consumption and the underwhelming use of renewable energy sources are depicted in **Figure 1.1**.[2] With the increased demand for energy sources, solar and other energy conversion methods will become necessary as fossil fuels become scarcer and cannot supply the increased demand.

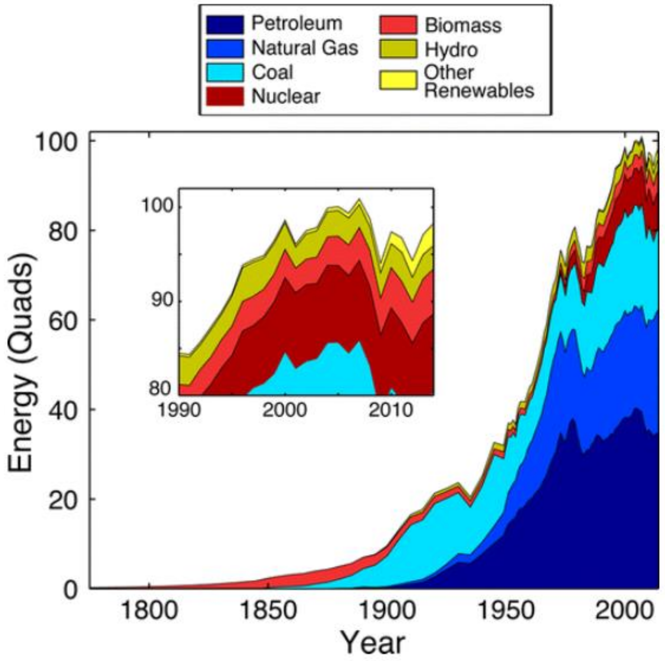

**Figure 1.1.** U.S. total energy consumption, by source, between 1775 and the present day. Data were collected from the U.S. Energy Information Administration.[1] (**Inset)** Detail of minor contributors to the U.S. energy mix since 1990. The “other renewables” category comprises primarily solar, wind, and geothermal energy. The ordinate unit “Quads” refers to quadrillion (1015) British thermal units, where 1 Quad = $1.055 \times 10^{18}$ J.[2]

With the increased demand for using renewable energy sources for energy conversion, harvesting solar energy has become a research field of high interest. The sun is the most abundant energy source available; more energy hits the Earth’s surface in the form of sunlight in a few hours than all of the energy consumed by the world’s population over the course of 1 year.[3] Solar cells and ion-batteries have been used to address the need for solar energy conversion and energy storage. However, current scientific challenges exist which impede current device performance. This includes a need to fundamentally understand the properties of semiconductors used in these devices in efforts to develop more efficient conversion and storage. Key research priorities include improving the chemical stability and lifetime of the semiconductors used in these applications, increasing the efficiency of energy harvest, and maximizing the capacitive limit of storage devices.

A variety of strategies can be implemented to combat the scientific limitations currently hindering solar energy conversion from becoming a practical alternative to fossil fuels. Solar energy can be converted to electrical, chemical, and thermal energy through a variety of processes; however, practical conversion efficiencies are currently below the theoretical limits.

Solar to thermal energy conversion is a process which generates energy by absorbing solar energy within liquid molecules (e.g. water) which are then used to generate heat or electricity. Generators can be powered by producing steam generated from heated water, producing electricity indirectly. In contrast, solar to electrical conversion can be accomplished directly using photovoltaic solar cells, which will be explained in future sections.

Solar to chemical fuel conversion, commonly known as photosynthesis, is a process in which plants convert solar energy using chlorophyll into chemical energy in the form of carbohydrates, as depicted by **Equation 1.1**. This process is generally very slow and converting solar energy to chemical fuel efficiently and cost-effectively is a challenge. Photoelectrical tandem cells have been proposed for use to convert solar energy directly to fuel by water splitting (i.e. artificial photosynthesis); however, a practical cell must be fabricated that optimizes cost and performance to justify replacing fossil fuels.[4]

$$6\ CO_2 + 6\ H_2O \rightarrow C_6H_{12}O_6 + 6\ O_2 \qquad \textbf{eq. 1.1)}$$

As the demand for energy sources continues to increase, the need to develop energy storage devices will also increase due to limitations of renewable energy conversion sources. Limitations may include weather fluctuations and the duration of night in which the sun is absent which would minimize solar harvest and presents a challenge. Furthermore, energy storage devices such as ion batteries can be implemented into the energy harvesting process in efforts to meet energy demands. Subsequent ***Sections 1.2-1.3*** outline the general scientific principles underlying photovoltaic solar cells and ion batteries.

### *1.2 Solar Cells*

Solar to electrical conversion is a process by which a photon can be captured using photovoltaic cells by exciting electrons across a semiconductor's bandgap to create electron-hole pairs that are charge separated, as seen in **Figure 1.2.** The materials used in the cells are generally semiconducting and sometimes doped in order to introduce free electrons (n-type material) or holes (p-type material) into the structure. The interfacial charge creates a voltage difference, which combined with the flow of electric current, generates electrical power directly from solar photons.

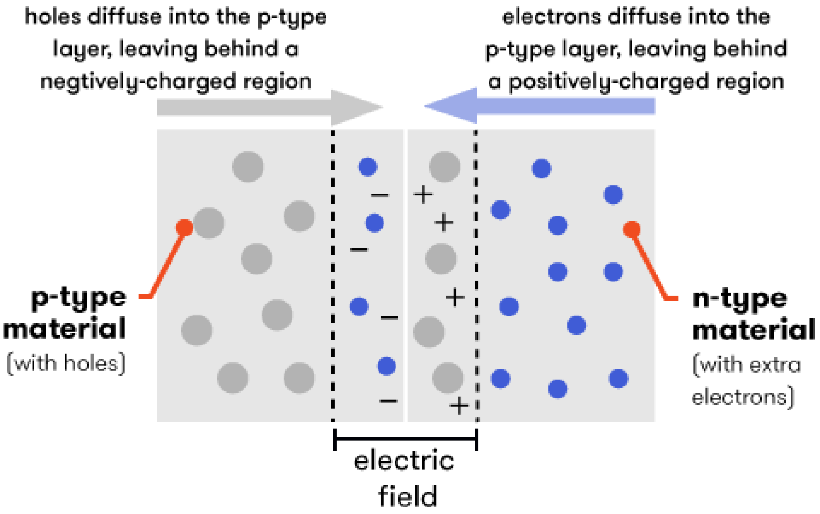

**Figure 1.2.** Diagram depicting the electric field generated in a p-n junction.[5]

Photovoltaic conversion efficiencies can be referred to in **Table 1.1**, as verified by the National Renewable Energy Laboratory.[6] Shockley and Queisser in 1961 established a theoretical efficiency limit of around 33.7% for a single p-n junction solar cell with a band gap of 1.4 eV (using an AM 1.5 solar spectrum) which has since been a target performance goal for researchers.[7] While silicon single crystal cells have generated 25% efficiency, current commercial products achieve only about 18% and other materials report even lower efficiencies. Silicon wafers are most commonly used but are also considered first-generation solar cells. Second-generation solar cells are made of thin film nanocrystalline materials that are less expensive than their crystalline silicon counterpart, but the efficiency of these cells is still low, as seen in **Table 1.1**. The future generation of solar cells would ideally have the efficiency of first-generation cells with the cost of second-generation cells, and can be produced by either using multiple junctions, carrier multiplication in which adsorption of a single photon results in multiple electron-hole pairs,[8] hot electron extraction,[9] or implementing novel materials to make thin films with higher efficiencies.

**Table 1.1.** Photovoltaic conversion efficiencies verified by the National Renewable Energy Laboratory, where the best experimental efficiencies are compared to experimental thermodynamic limits. Note that organic cell efficiencies up to 5% have been reported in the literature.

| | Laboratory Best | Thermodynamic Limit |
|---|---|---|
| **Single Junction** | | 31% |
| Silicon (crystalline) | 25% | |
| Silicon (nanocrystalline) | 10 % | |
| Gallium arsenide | 25 % | |
| Dye sensitized | 10 % | |
| Organic | 3 % | |
| **Multijunction** | 32% | 66% |
| Concentrated sunlight (single junction) | 28% | 41% |
| Carrier multiplication | | 42% |

There has been an increased interest in using solar cells as a renewable energy source over the past two decades. As a result, they have been extensively researched due to their low cost to produce and their potential to improve photovoltaic conversion efficiency, more specifically dye-sensitized solar cells (DSSCs). These will be discussed in further detail in ***section 1.2.1***.

### *1.2.1 Dye Sensitized Solar Cells*

In solar cells, an n-type and p-type interface are used for charge separation. As incident light excites electrons and promotes them into a higher energy state from the valence band, a p-n junction is created where free electrons from the n-type semiconductor diffuse across the junction to combine with holes, assuming electron-hole recombination does not take place from the excited electron into the conduction band of the p-type material. DSSCs are classified as a type of heterojunction solar cell in which two materials that are chemically different are adjacent to each other to form an interface.

DSSCs were originally invented in the late 1980s by O’Regan and Grätzel and is alternatively referred to as the Grätzel cell.[10] Rather than using a p-n junction to generate a current between semiconductors, DSSCs utilize either a p- or n-type semiconductor which has a photoactive molecular dye coated on the surface. In a n-type DSSC, incident light is absorbed by the molecular dye which excites electrons and allows them to flow toward the semiconductor. The electrons from the semiconductor then diffuse through the material and come into contact with the counter electrode to flow into the electrolyte back to the molecular dye for regeneration. The electrolyte can vary, but $I^-/I_3^-$ electrolyte solution is commonly used as depicted in **Figure 1.3**. Electrolyte solutions will be discussed in greater detail in ***Section 1.5.2***. P-type DSSCs work in a similar fashion with the exception that holes flow from the dye into the valence band of a p-type semiconductor rather than free electrons.

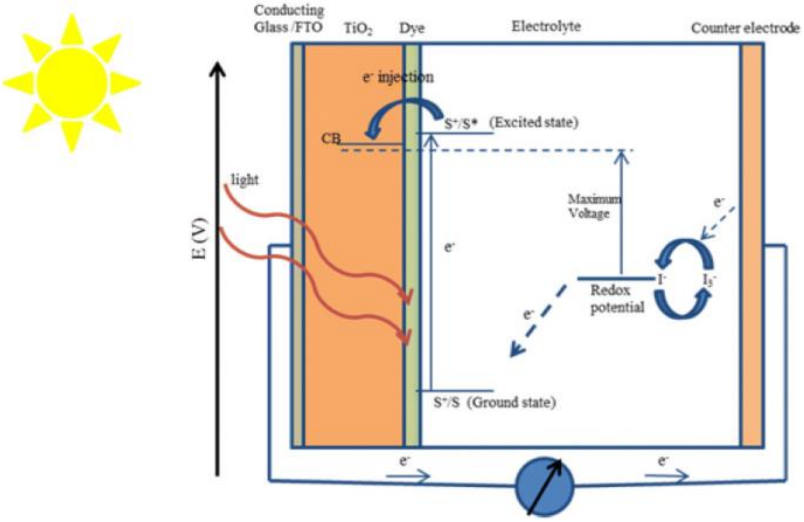

**Figure 1.3.** Diagram of a n-type DSSC where $TiO_2$ is the semiconductor used.[11]

In dye-sensitized solar cells, a variety of semiconductors have been researched and implemented into laboratory cells. $TiO_2$ has been widely studied as an n-type semiconductor and is suitable for many applications due to its stability, abundance, insolubility in water, and lack of toxicity. Due to $TiO_2$ being used as a common model in current research, a summary of $TiO_2$ characterization and influential research studies are summarized in ***Section 1.4***. Additionally, implementation of alternative metal oxides, both n- and p-type, is discussed in ***Section 1.4***.

### *1.3 Ion Batteries*

Energy storage is equally as important as energy conversion. While solar to electric energy conversion is possible using photovoltaic devices, we cannot harvest 100% of the available energy output from the sun. Additionally, nonideal weather and nighttime lead to periods where solar conversion is inefficient which makes solar energy storage equally important to research and for implementation. The effectiveness and overall performance of energy storage devices can be measured by the rate of energy lost in the storage process, the overall storage capacity of the device, the recharging rate, and the long-term cycling stability.

Ion batteries, specifically lithium-ion batteries, are the most popular energy storage devices used today and encompass over 90% of the global grid battery storage market due to their high energy density, high cycling lifetime, and are light weight.[12] By researching novel cathodic and anodic materials that are capable of increasing the storage capacity and stability of batteries, overall performance and global storage capabilities can be improved.

### *1.3.1 Battery Components and Operation*

The components of a lithium-ion battery are shown in **Figure 1.4**. As lithium ions and electrons are transferred from the cathode to the anode, charge is stored for future use. This is done via oxidation of the cathode and reduction of the anode. **Figure 1.5** shows a vertical potential diagram of a general lithium-ion battery cell.

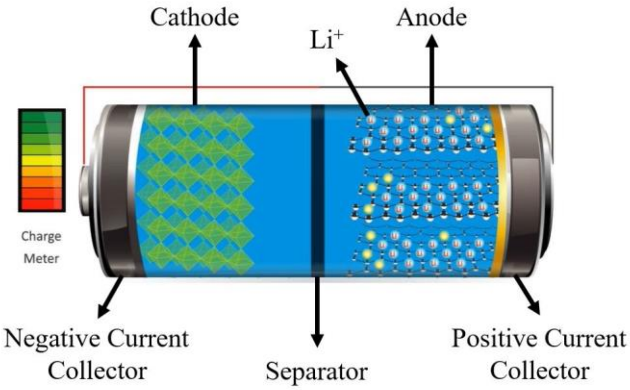

**Figure 1.4.** Components of a Li-ion battery.[13]

During discharge, as seen in **Figure 1.5** (left), lithium ions are removed from the anode (delithiation) and inserted into the cathode (lithiation) to accompany transfer of electrons from the anode to the cathode. It is important to note that as lithium ions are transferred between electrodes, reduction of metal sites occurs within the cathode, $\mathrm{Cat} + e^- + \mathrm{Li}^+ \rightarrow \mathrm{Li}^+\mathrm{Cat}^-$, and oxidation of metal sites within the anode, $\mathrm{Li}^+\mathrm{An}^- \rightarrow \mathrm{An} + e^- + \mathrm{Li}^+$ during discharge in order to charge balance the system.

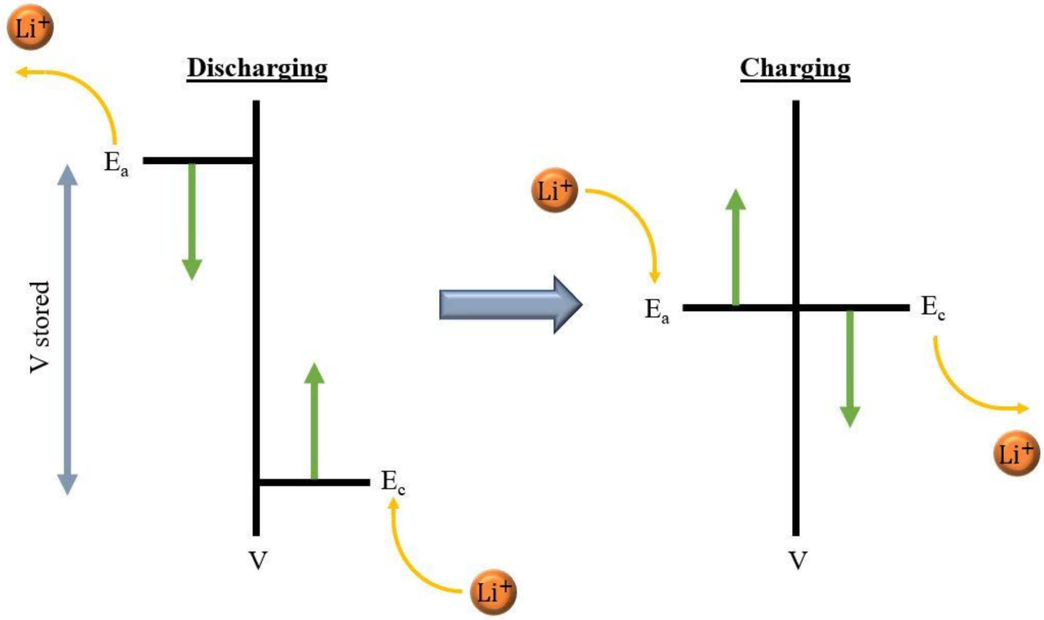

**Figure 1.5.** General vertical potential scale for the anode and cathode in a Li-ion battery during discharge from the charged state **(left)** vs. charging from the discharged state **(right)**. Green arrows indicate the direction in which the anode potential ($E_a$) and cathode potential ($E_c$) moves during each process. Orange arrows indicate the direction of $\mathrm{Li}^+$ movement.

Within a battery, the anode is typically graphite, and the cathode is typically a metal oxide material in conjunction with carbon black for enhanced conductivity. The graphite anode has a layered, planar structure where carbon atoms are arranged in a honeycomb lattice. The metal oxide cathode is composed of empty layers and interstitial channels, usually due to having edge-shared or corner-shared octahedra within the structure. These layers and interstitial channels allow for lithium ions to flow from one material to the other and intercalate into each material. Among p-type delafossite transition metal oxides, $CuCrO_2$ exhibits moderate conductivity, with high conductivity being reported for doped $CuCrO_2$, and may be a good candidate to be used as a cathodic material in Li-ion batteries.[14]

### *1.4 Implementation of Metal Oxides in Solar Energy Conversion and Storage Devices*

Metal oxides are commonly utilized in solar cell devices to control the flow of electrons (n-type oxides) or holes (p-type oxides) to the external circuit. Due to its original implementation in the Grätzel cell, $TiO_2$ quickly became a commonly studied n-type semiconducting oxide for use in solar cells.[15–17] Compared to other oxides, $TiO_2$ is more resistant to photocorrosion, has maximum quantum yields due to high photocatalytic activity, and has a wide band gap[18,19]. Anatase $TiO_2$ specifically has a band gap of 3.2 eV which is beneficial for allowing visible light to be absorbed by molecular dyes within DSSCs.[20] Nickel oxide (NiO) is an analogous p-type semiconductor that has been studied for DSSC applications due to its wide band gap and hole transport properties.

In terms of energy storage in ion batteries, lithium cobalt oxide (LCO), lithium manganese oxide (LMO), and lithium nickel manganese cobalt oxide (NMC) are all typical cathodic battery materials. LCO has a relatively short life span and low thermal stability with a reported specific capacity of 274 mA h $g^{-1}$, while LMO has a specific capacity of 148 mA h $g^{-1}$. However, even with improved stability, the cycle and shelf life of LMO is still limited.[21] NMC is one of the best performing materials currently available due to its fine tuning and the optimized ratio of nickel and manganese in the structure. Nickel has high specific energy but poor stability while manganese has low internal resistance in the formation of spinel structures but offers low specific energy. Combining both allows for the enhancement of both strengths, and the resulting measured specific capacity is 234 mA h $g^{-1}$.[21]

### *1.4.1 Delafossite $CuCrO_2$*

Copper chromium oxide ($CuCrO_2$) is a p-type metal oxide with applications in both DSSCs and Li-ion batteries. Delafossite $CuCrO_2$ can be synthesized in two distinct phases: the space group $P6_3/mmc$ (**Figure 1.6**, left) and $R\bar{3}m$ (Figure 1.19, right).[22] The most notable distinction between the two phases is that the hexagonal phase has a stacking sequence ABABAB while the rhombohedral phase has a stacking sequence ABCABCABC.

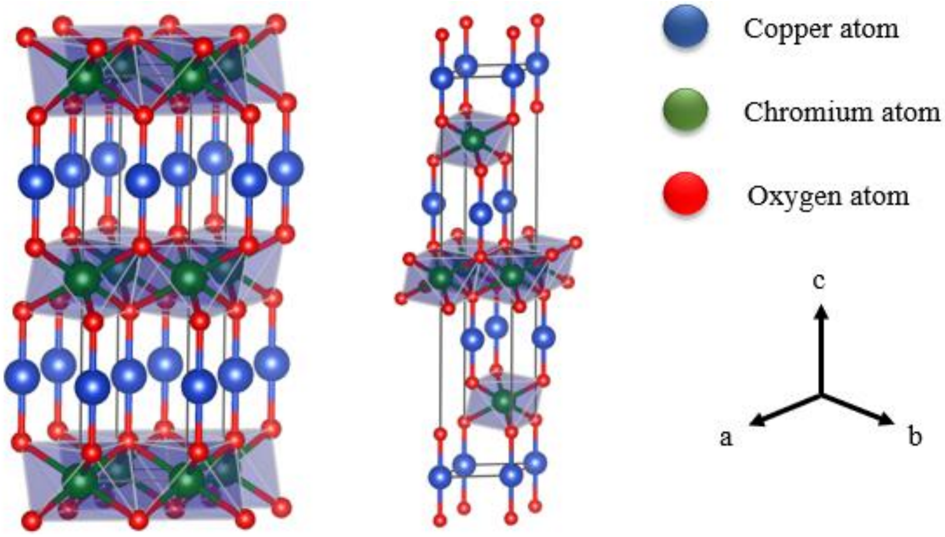

**Figure 1.6.** Comparison of delafossite $CuCrO_2$ hexagonal $p6_3/mmc$ crystal phase (mp-505562) **(left)** and trigonal $R\bar{3}m$ crystal phase (mp-510625) **(right)**.[22]

The use of CuCrO2 within p-type DSSCs has been well reported due to its wide band gap and relatively high valence band edge.[23–26] However, previous studies have concluded p-type transparent oxide semiconductors (TOSs) have inferior performance compared to their n-type counterparts, exhibiting short hole diffusion lengths which impede charge extraction.[27,28] One proposed reason for the inferior performance of p-type semiconductors is that electronic defects result in poor charge separation at the metal oxide interface. The proclivity of defects in $CuCrO_2$, in addition to byproduct formation, has been reported by Zhao et al.[29] An important defect common within $CuCrO_2$ is the presence of $Cu^+$ vacancies which lead to the oxidation of adjacent $Cu^{2+}$ atoms. This increases hole density and allows for higher conductivity and faster charge extraction which can allow for Li-ion intercalation and improve ion battery performance. However, higher hole density may also lead to poor solar cell performance through recombination of electron-hole pairs. Understanding how defects fundamentally influence charge transport properties of semiconducting materials is of great importance, and from further research it may be conclusively important to tune the material and induce or restrict defect formation based on the application.

### *1.5 Electrochemistry*

Electrochemistry is a sub-field of chemistry in which characteristics of an analyte or solid-state material in an electrochemical cell can be studied to observe changes in potential or current directly correlated to chemical changes. While a variety of electroanalytical methods are used to study the electrochemical processes of materials, a select few are highly utilized for these studies: electrochemical impedance spectroscopy, cyclic voltammetry, chronoamperometry, and chronocoulometry. The following sections describe the experimental setup and theory behind electroanalytical chemistry in addition to these techniques.

### *1.5.1 Experimental Setup*

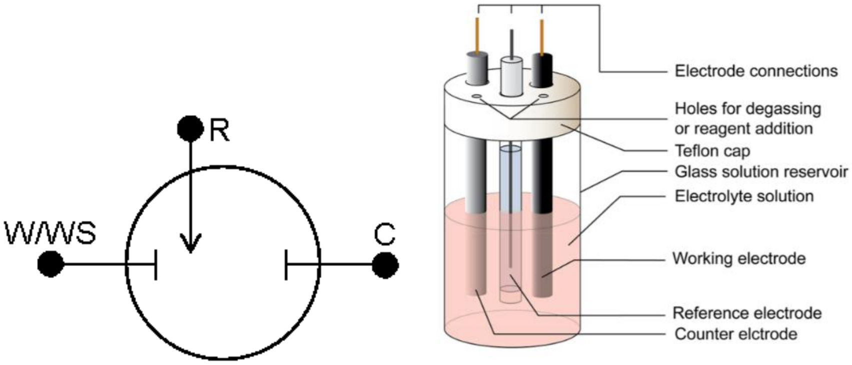

**Figure 1.7.** General setup for a 3-electrode cell.[30]

Most electrochemical experiments, and all the experiments conducted within this thesis, are done using a 3-electrode cell depicted in **Figure 1.7**. In this setup, a working electrode and reference electrode are connected to a counter electrode. Having a counter electrode present in the system allows for potential changes of the working electrode to be measured independent of changes in potential at the counter electrode by measuring only half of the cell, ensuring accuracy and preventing potential drift.

The working electrode is the electrode in which the reaction of interest is occurring. Glassy carbon and platinum are commonly used as working electrodes in aqueous electrochemistry, but solid-state materials can also be fabricated into thin films to function as the working electrode.

The reference electrode is used to measure the potential without passing any current through the working electrode. Reference electrodes are chemically stable and have a well-known, reversible potential. A wide variety of reference electrodes are used during experimentation and have well documented reversible potential relationships which can be used interchangeably for comparison among experiments. Standard reduction potentials for common reference electrodes are displayed in **Figure 1.8**, where the normal hydrogen electrode (NHE) and standard hydrogen electrode (SHE) is considered to have a reduction potential of 0 V, defining the zero point on the electrochemical scale. While not displayed in **Figure 1.8**, it is important to note that the reduction potential for ferrocene$^{3+/2+}$ in acetonitrile is -400 mV versus Ag/AgCl. Ferrocene is used for all experiments as an internal standard, and it is also measured before and after every electrochemical experiment conducted to ensure no potential drifts have occurred to validate the data collected.

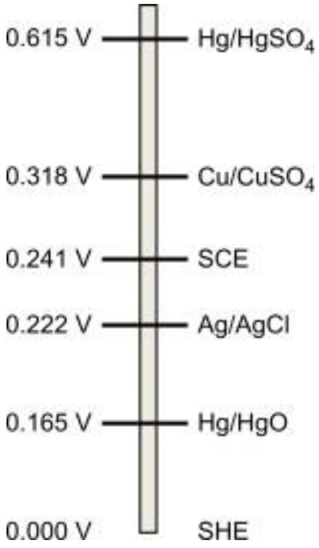

**Figure 1.8.** Reduction potentials versus SHE/NHE for commonly used reference electrodes.

In contrast to the reference electrode, the counter electrode allows for the flow of current between it and the working electrode by closing the current circuit in the electrochemical cell. Because of this interaction between the counter and working electrode, the reference electrode permits the observation of potential changes in the working electrode accurately. Gold and platinum are commonly used counter electrodes as they are relatively inert materials and will not participate in the electrochemical reaction.

### *1.5.2 Electrolyte Solutions*

An electrolyte is crucial for operation in both aqueous and nonaqueous electrochemistry because the ions in solution move in accordance with their charge and the applied potential; this neutralizes the charge of the ions and ensures the reaction proceeds as a system's potential is modified and current is generated as ions move through solution. Generally speaking, as an electric potential is applied to the electrochemical cell, the cations in the electrolyte solution travel toward the electrode which has an abundance of electrons, and the anions travel toward the electrode with an excess of holes.

The double layer, also referred to as the Helmholtz layer due to its discovery and reported phenomena in 1853 by Hermann Helmholtz, is the interface formed between a solid surface and electrolyte solution.[31] Specifically, electrodes with an excess of electrons or holes will attract their ion counterpart from electrolyte solution while repelling ions with the same charge. This results in the formation of a double layer between the solid surface and bulk solution, as depicted in **Figure 1.9**.[31,32] Within the double layer, a diffuse region can be seen between the outer Helmholtz layer and the bulk solution; the observance of a diffuse region is a phenomena which is specific to semiconductor materials. Mott-Schottky analysis can be useful for determining semiconductive properties based on the observed capacitance in the diffuse region to estimate electron donor density and flat band potential values. Conclusively, these phenomena contribute to the charge transfer and charge accumulation in battery and solar cell devices.

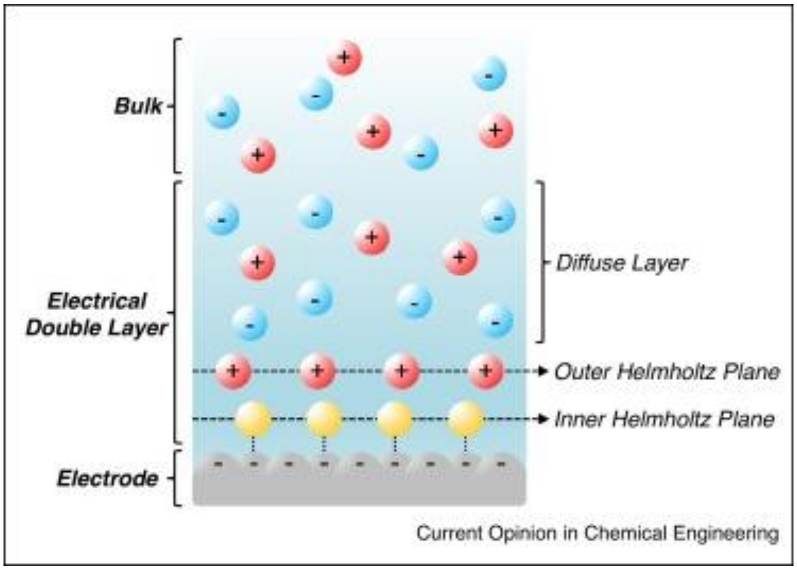

**Figure 1.9.** Schematic diagram of the electrical double layer.[32]

A variety of electrolyte solutions are used in electrochemistry, but superior solutions are easy to prepare, permit high conductivity, have low viscosity which reduces charge carrier transport resistance, and have high conversion efficiency for DSSCs. Liquid electrolytes are the most commonly used transport medium for DSSCs and have also produced the highest efficiencies reported in literature.[33] Lithium perchlorate ($LiClO_4$) and tetrabutylammonium perchlorate ($TBAClO_4$) are widely used electrolytes due to their low viscosity and high conductivity. Perchlorates in nonaqueous solutions have wide potential windows, with reports exceeding 3 V.[34,35] This allows ion batteries to store large amounts of energy, and solar cells to perform charge carrier transport, at extreme potentials beyond the stability window of aqueous electrolytes.

Iodide triiodide ($I^-/I_3^-$) electrolyte solution is also commonly used in DSSCs due to its stability, rapid dye regeneration, and most importantly the slow recombination kinetics between the electrons in the semiconductor used and triiodide which ensures good efficiency in solar cell performance.[36]

### *1.5.3 Electrochemical Impedance Spectroscopy (EIS) Theory and Background*

One of the most complex yet informative electroanalytical methods is electrochemical impedance spectroscopy (EIS), an AC technique that measures the current response (I) as both resistive and capacitive behavior of an electrochemical system while varying the frequency (ω) of a modulated potential (E). While the ideal resistor abides by Ohm's Law, R = E/I, and maintains a resistance independent of frequency, real-world circuits are often much more complex and the behavior observed deviates from Ohm's Law. We can redefine the circuit elements by introducing the concept of impedance, which is the measure of current resistivity by the circuit but is analyzed as a sum of sinusoidal functions, as seen in **Figure 1.10**. Because a modulated potential (E) is measured at fixed frequencies (ω), the resulting current (I) measured has the same frequency but is shifted due to differences in the phase angle. Relationships between current and potential as a function of time can be expressed to define impedance at a fixed frequency, shown in **Equations 1.2-1.4**.

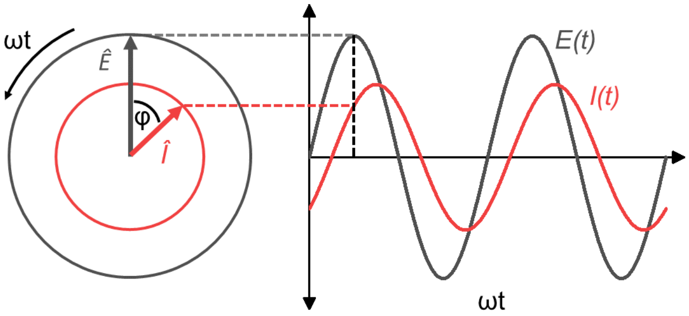

**Figure 1.10.** Sinusoidal representation of current as a function of potential where impedance can be measured by taking the relationship of E(t) and I(t) into consideration.[37]

Applied potential $E(t) = |E_0|\sin(\omega t)$ **eq. 1.2)**

Observed current $I(t) = |I_0|\sin(\omega t + \varphi)$ **eq. 1.3)**

Impedance $Z(\omega) = E(t)/I(t)$ **eq. 1.4)**

In a typical EIS experiment, the modulation frequency is sampled over a wide range (~1 mHz to 1 MHz) for a fixed applied potential ($E_{app}$) on top of which the small modulation amplitude $|E_0|$ is applied such that $E(t) = E_{app} + |E_0|\sin(\omega t)$. When the frequency range is completed, $E_{app}$ is shifted to a new value and the process is repeated. For a single potential, experiments may take anywhere from a few seconds to tens of minutes depending on the frequency range of interest. Therefore, it is not uncommon for experiments to take many hours to fully collect EIS data over a wide potential range and/or with a small step size between applied potentials.

Collected data is then interpreted using a variety of plots. The most important is the Nyquist plot, in which impedance is plotted as a complex number ($j = -1^{1/2}$) according to **Equation 1.5** with $Z_{Im}$ (Z”) along the y-axis and $Z_{Re}$ (Z’) along the x-axis (**Figure 1.11**). Each data point in a Nyquist plot represents a different frequency with ω decreasing from left to right. At infinitely low frequencies, the applied potential is essentially constant, and this condition is often relevant when relating EIS data to other DC electrochemical techniques such as cyclic voltammetry. For each frequency, the impedance is defined by a vector originating from the origin with magnitude |Z| and phase angle φ. These two terms are defined with respect to $Z_{Re}$ and $Z_{Im}$ by **Equations 1.6-1.7**.

$Z(\omega) = |Z|(\cos(\varphi) - j\sin(\varphi)) = Z_{Re} - Jz_{Im}$ **eq. 1.5)**

$|Z| = (Z_{Re}^2 + Z_{Im}^2)^{\frac{1}{2}}$ **eq. 1.6)**

$\tan\varphi = Z_{Im}/Z_{Re}$ **eq. 1.7)**

The data collected over the selected potential range for the studied electrochemical circuit can be plotted in a variety of ways to provide information regarding the resistive and capacitive elements of the circuit. Nyquist plots are generated using derived real and imaginary components of the impedance, $Z_{Re}$ and $Z_{Im}$, respectively, at different frequencies to provide insight into circuit elements including solution resistance (a shift in the Nyquist plot along the x-axis), faradaic and non-faradaic capacitance due to charge transfer and accumulation (a semicircle or collection of semicircles), ion diffusion (an upward slope feature extending from the semicircle at the low frequency region), and a takeoff region at low frequencies which is ideally 45˚ with respect to the $Z_{Re}$ axis, as seen in **Figure 1.11 (left)**. Angles which deviate toward higher or lower angles correspond to higher capacitance or higher resistance, respectively. Additionally, widely used Bode Phase and Bode Z plots can also be plotted which show impedance $|Z|$ or phase angle $\varphi$ across the modulated frequency range as seen in **Figure 1.11 (right)**. Bode plots are sometimes advantageous to use in conjunction to Nyquist plots because smaller features from capacitive and resistive elements are easier to identify in Bode plots while larger features in Nyquist plots are overwhelming and make deciphering elements in complex circuits more challenging.

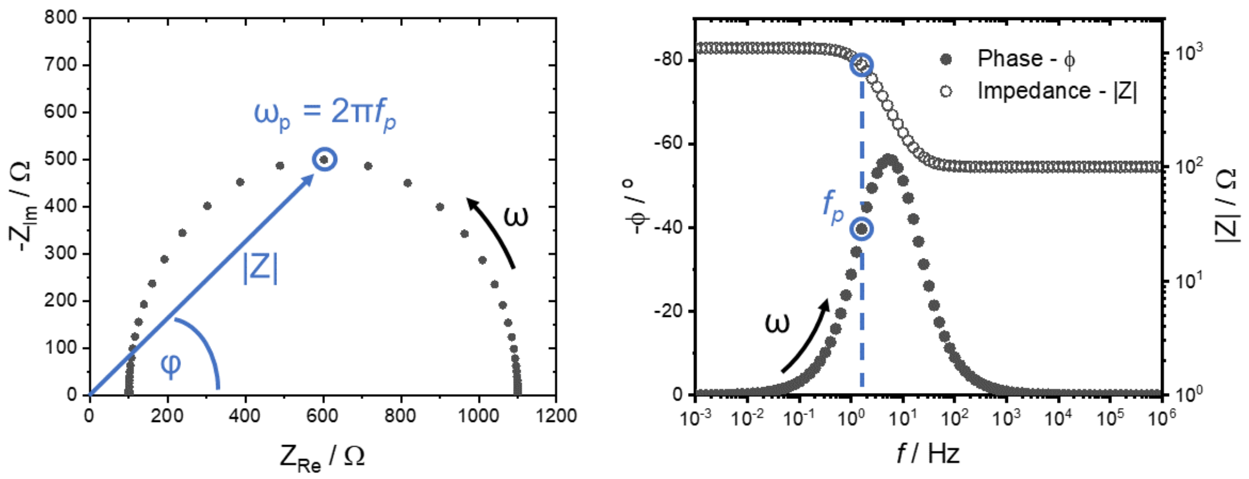

**Figure 1.11.** A simple representation of a Nyquist plot **(left)** and a combined Bode phase-|Z| plot **(right)** for a simple Randles circuit.[37]

More quantitative data relating to each circuit element, in addition to a physical understanding of the circuit, can be determined by fitting and modeling the EIS data. A basic and common circuit model, the Randles circuit, is shown in **Figure 1.12** and contains the primary elements of all electrochemical circuits where a solution resistance is observed followed by a resistance and capacitance of the material studied. Resistors represent faradaic charge transfer reactions across interfacial layers while capacitors represent non-faradaic charge accumulation at either solid-solid or solid-liquid interfaces. In some cases, capacitors are replaced by constant phase elements (CPE) for systems in which the capacitor behavior is not ideal. These nonidealities are caused by inhomogeneous electrode surfaces which directly influences the observed double layer capacitance. A model with CPE elements includes an additional β value ranging from 0 to 1, where 1 represents an ideal capacitor and values lower than one deviate from ideality. Mesoporous electrodes and thin films with porous characteristics are often modeled with CPE elements.

Solution resistance is directly correlated to the diffusion of ions through electrolyte solution, and as previously discussed, a low viscosity solution is ideal to minimize solution resistance.

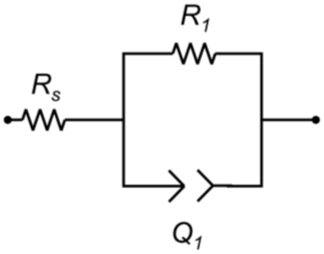

**Figure 1.12.** Diagram of a simple Randles circuit where Faradaic current is correlated with a charge transfer resistance ($R_{ct}$ or $R_1$) and non-Faradaic current is correlated with an interfacial capacitance ($C_{int}$ or $Q_1$). A series resistance term, $R_s$, is shown to represent resistance due to wires, contacts, and solutions.[37]

Other more complex and commonly used EIS models are provided with explanations of circuit elements and useful conditions in EIS review literature.[37] A complex model worth mentioning was used to fit EIS data for mesoporous p-type $CuGaO_2$ thin films, shown in **Figure 1.13**.[38] Due to similar characteristics of this film to that of p-type $CuCrO_2$ thin films, the equivalent circuit models used for both materials are similar in nature.

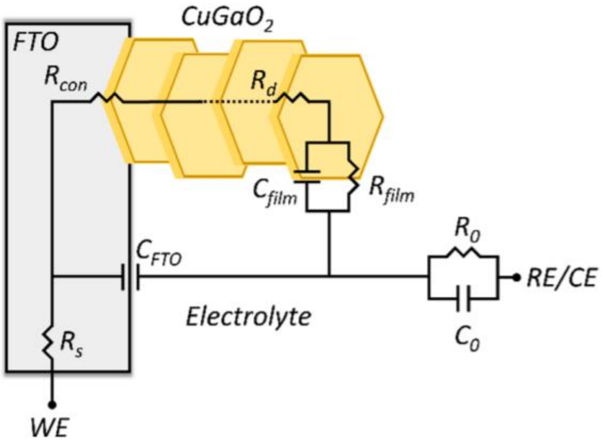

**Figure 1.13.** Schematic diagram of the equivalent circuit model used to fit data for mesoporous $CuGaO_2$ thin film EIS data.[38]

It is important to note that multiple models can be generated to fit the same set of data with a reasonable level of accuracy; however, not all models are physically relevant, and their interpretation of the real-world circuit can be incorrect. Furthermore, it is important that when fitting EIS data to a model that the user can justify the physical relevance of the model used to explain the capacitive and resistive elements of the entire system.

An extensive review of EIS studies and modeling for solar cell applications has been published.[37] In this review as well as in ***Chapter 2*** of this thesis, an extensive review of previous EIS studies and modeling for application in ion batteries is also provided.

### *1.5.4 Cyclic Voltammetry: Scan Rate Dependence and Kinetics Plots*

While EIS is an AC technique that gives insight into the capacitive and resistive elements of an electrochemical circuit, cyclic voltammetry (CV) is a DC technique which shows capacitive and resistive elements of a circuit simultaneously. While the data acquired from CV is not as detailed as EIS, its ease of use and relatively simple analytical interpretation makes it a viable and common technique used in literature.

As a linear potential sweep is applied to an electrochemical system at a designated scan rate, the resulting current is measured for the system to provide insight into redox activity. Oxidative events happen as the potential applied sweeps positively, and reductive events occur as the potential sweeps in a negative direction. As an oxidation or reduction event begins to occur, an onset is observed where oxidation or reduction occurs at the surface of the working electrode until a peak maximum is reached. At the anodic and cathodic peak potentials ($E_{pa}$ and $E_{pc}$ in **Figure 1.14**), the measured current is limited by the diffusion kinetics of the analyte from the bulk solution to the electrode surface; this results in a decrease in the observed current until a steady-state has been reached and the redox event can be visualized in the voltammogram. The halfwave potential, $E_{1/2}$, lies halfway between the potentials of the $E_{pa}$ and $E_{pc}$ for a redox event at which the oxidized species and reduced species are at equal concentrations. Preparation and analytical details further describing the fundamentals of CV can be referenced here.[30]

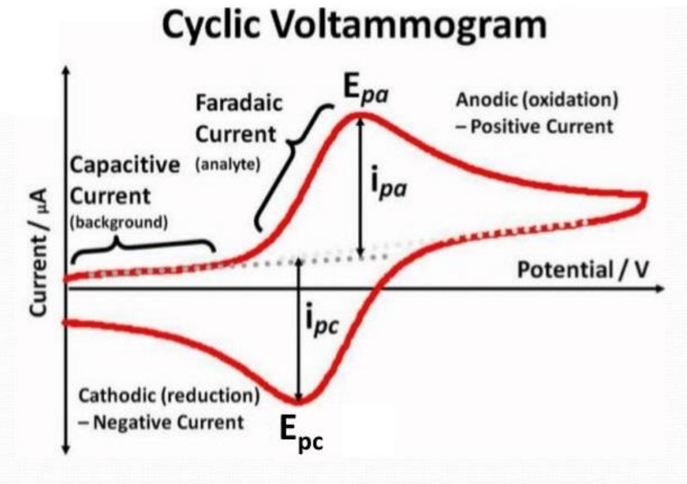

**Figure 1.14.** Schematic representation of a reversible cyclic voltammogram.[39]

Scan rate dependence studies can be done using cyclic voltammetry to extract information pertaining to the kinetics of electron-transfer reactions occurring at the electrode surface. After conducting CV at various scan rates, oxidative and reductive peak currents for observed redox processes can then be plotted as log current versus log scan rate as depicted in **Figure 1.15**. The plot reveals two linear slopes: a slope close to a value of 1 at lower scan rates, and a slope close to a value of 1/2 at higher scan rates. A slope of 1 indicates that electron transfer is not kinetically limited by diffusion. A slope of 1/2 indicates electron transfer is limited by diffusion. Because fabricated mesoporous thin films do not have a flat metal surface, both diffusion and electron transfer can commonly be seen as contributing factors to the rate limiting kinetics of the system. Diffusion coefficients and additional information regarding the kinetics of the system can be determined through Anson plot analysis using chronoamperometry.

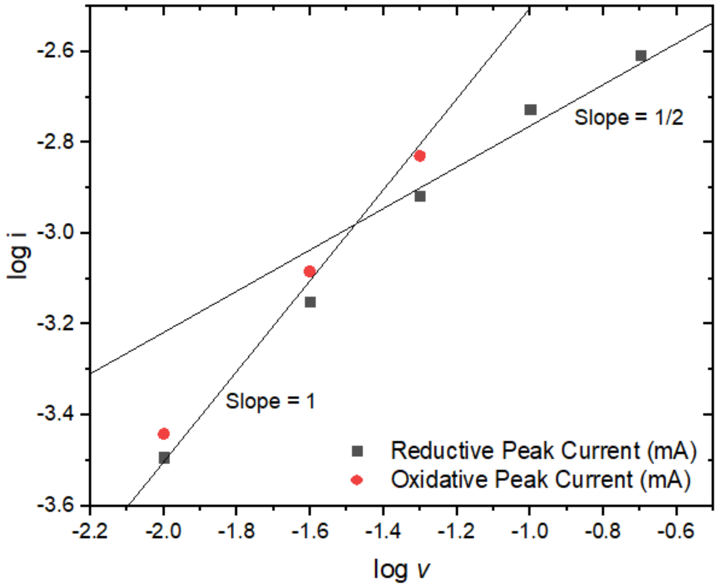

**Figure 1.15.** A log i-*v* plot constructed by deriving $E_{pa}$ and $E_{pc}$ values from square root normalized scan rate dependent cyclic voltammograms for a mesoporous $CuCrO_2$ thin film electrode.

### *1.5.5 Chronoamperometry: Amperometric IT Curves and Anson Plots*

Chronoamperometry is used to study kinetic events of an electrochemical system that occur because of redox reactions, diffusion, and adsorption at the electrode surface. During this experiment, a fixed potential is applied to the working electrode and the current response is measured as a function of time which outputs an amperometric IT curve, as seen in **Figure 1.16**, where τ represents the amount of time a potential is applied before stepping to a subsequent potential.

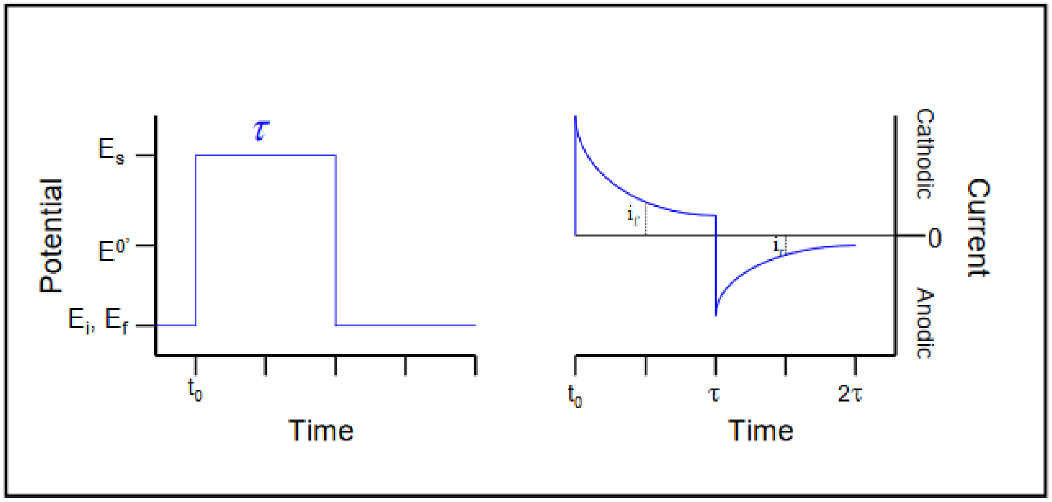

**Figure 1.16.** Schematic diagram of a chronoamperometry experiment outputting an IT curve.[40]

Anson plots are especially useful for quantifying electrode reactions of adsorbed species and can be derived using chronoamperometry data and studying the Anson equation to describe change in current as a function of time. The Cottrell equation (**Equation 1.6**) is used to describe the behavior of the current (i) in a planar electrode in potential-step experiments with respect to time (t). The current is dependent on the area of the planar electrode (A), the diffusion coefficient of the analyte ($D_0$), and the initial concentration of the analyte ($C_0^*$). Integration of the Cottrell equation with respect to time yields the Anson equation (**Equation 1.7**) and allows for the direct comparison of charge (Q) as a function of time. This relationship describes the rate of charge accumulation in the system. Additional variables can be introduced to the equation for systems where double layer charge ($Q_{dl}$) and charge due to redox active sites within a thin film electrode ($nFA\Gamma_0$) are present. These concepts can be visualized in the generic Anson plot shown in **Figure 1.17**.

$$i(t) = \frac{nFAD_0^{\frac{1}{2}}C_0^*}{\pi^{\frac{1}{2}}t^{\frac{1}{2}}} \qquad \textbf{eq. 1.6)}$$

$$Q = \frac{nFAD_0^{\frac{1}{2}}C_0^*t^{\frac{1}{2}}}{\pi^{\frac{1}{2}}} + Q_{dl} + nFA\Gamma_0 \qquad \textbf{eq. 1.7)}$$

It is important to note that for solution-based electrochemistry, kinetic limitations may arise. Charge Q can be measured and compared at different potential steps and differences due to kinetics can be easily visualized in an Anson plot. Consider a double potential step chronoamperometry experiment in which the first potential held is negative and reduction occurs (forward step), and the second potential held is positive and oxidation occurs (reverse step) as depicted in **Figure 1.16**. The reduced species can be reoxidized to its original state during the reverse step if those species are within a close enough proximity to the electrode. If the kinetics of the system are slow enough such that the reduced species travel away from the electrode before oxidation is permitted, those species would remain electrochemically inactive during the reverse step. This would furthermore lead to a decrease in charge observed during the reverse step. This can be seen in **Figure 1.17** (right) where the forward reaction in the Anson plot is plotted as a function of $t^{1/2}$ (top axis), whereas the reverse reaction is plotted as a function of $\tau^{1/2} + (t-\tau)^{1/2} - t^{1/2}$ (bottom axis) which accounts for the charge that is measured for the electrochemically reversible species during the reverse step. The total charge for reversible species on the reverse step can be determined using **Equation 1.8**.

$$Q_r = \frac{2NFAC_0D_0^{\frac{1}{2}}}{\pi^{\frac{1}{2}}}[\tau^{\frac{1}{2}} + (t-\tau)^{\frac{1}{2}} - t^{\frac{1}{2}}] \qquad \textbf{eq. 1.8)}$$

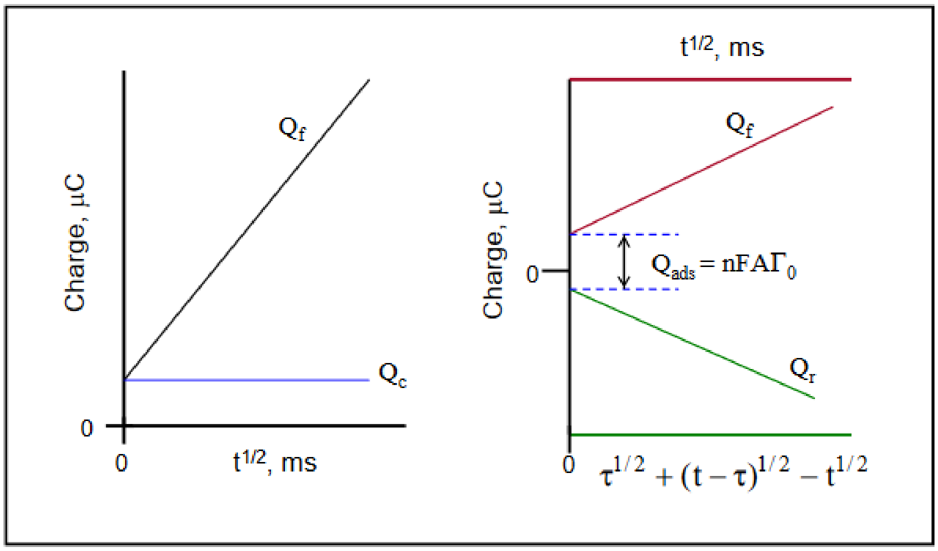

**Figure 1.17.** A general diagram of an Anson plot and relevant features.[40]

### *1.5.6 Chronocoulometry: Chronopotentiometry*

Whereas chronoamperometry experiments involve applying a constant potential to measure the resulting current as a function of time, chronopotentiometry is a useful technique in which a constant current is applied to the system over time to study potential changes in the system, making this a galvanostatic technique. This is especially useful when studying materials for energy storage in batteries because the data can be easily interpreted to study the charge and discharge capacities, as well as long term cycling efficiencies and corrosion rate.

As a fixed current is applied, the redox active species will be reduced or oxidized at a constant rate depending on whether or not the system is charging or discharging. The potential of the working electrode moves to values similar to what is seen at the $E_{1/2}$ potential observed in cyclic voltammograms for a redox event. Over time, the concentration of oxidized or reduced species will change at the interface and once the redox event has completely oxidized or reduced the target species, the potential at the transition time ($\tau$) will shift to more positive or negative values until a new oxidation or reduction event begins (**Figure 1.18**).[41]

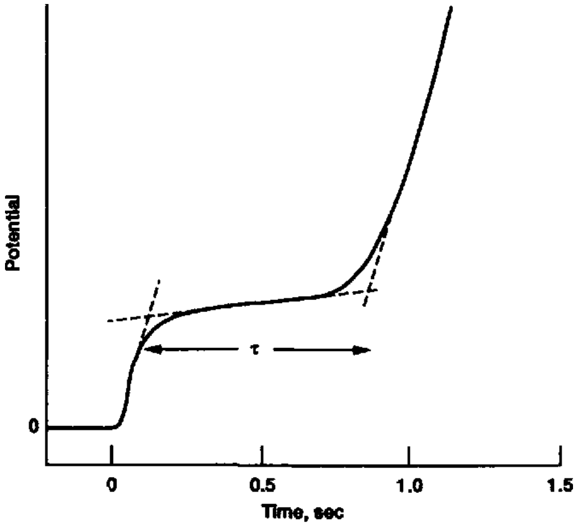

**Figure 1.18.** Schematic diagram of a chronopotentiogram.[42]

### *1.6 Conclusions*

The increased energy demand globally has led to an interest in developing solar and other renewable energy conversion methods in addition to energy storage devices to satisfy the projected increase in energy consumption. Among these strategies is the development and advancement of solar cell devices, but scientific limitations are currently hindering the application of solar energy conversion as an alternative to fossil fuels. Limitations include high cost and underwhelming efficiency limits of first- and second-generation solar cells relative to the Schockley-Queisser limit. Understanding the fundamental electrochemical properties of alternative p-type semiconducting materials, such as delafossite $CuCrO_2$, will ultimately aid in fabrication tailored to achieving higher efficiency limits while maintaining low costs.

Additionally, defects have been shown to enhance the performance of ion battery materials by increasing hole density, allowing for higher conductivity and faster charge extraction. However, inducing defects resulting in higher hole density may lead to inefficient solar cell performance due to electron recombination. Conclusively, it is important to study fundamentally the role defects have on electrochemical characterization for both solar energy conversion and storage devices, and to tune the material and induce or restrict defect formation based on the application.

In this thesis, the synthesis and characterization of delafossite $CuCrO_2$ is reported for the purpose of fundamentally understanding the roles of defect states and how application in solar cells and Li-ion batteries may be compromised or enhanced. In the next few chapters fundamental details related to these ideas will be discussed. ***Chapter 2*** expands on how EIS can be utilized to study metal oxides and the resistive and capacitive elements within the electrochemical circuit for ion battery research and application. A hydrothermal synthetic route was optimized to grow delafossite $CuCrO_2$ nanoparticles, and the role of $Cr^{3+}$ as the reducing agent in the reaction was extensively studied and reported in ***Chapter 3***. While some electrochemical characterization has been done on $CuCrO_2$, the findings are scarce in literature. In ***Chapter 4***, we provide extensive electrochemical characterization of optimized pristine $CuCrO_2$. Such electrochemical studies revealed a significant $Li^+$ dependence on the $Cu^{2+/+}$ redox events observed by CV in addition to the surface charge of $CuCrO_2$. Morphological studies were also conducted in which $CuCrO_2$ was compared electrochemically to $CuGaO_2$ in which the $CuGaO_2$ particles were more anisotropic and larger in nature. This revealed the importance of particle morphology and the exposure of Cu-terminated faces. Degradation studies are also discussed in more detail. Finally, studies on defect states of $CuCrO_2$ and how their properties are influenced are scarce. Introduction of defect states, specifically cationic vacancies, into host intercalation compounds can effectively influence the electrochemical properties of electrode materials for lithium storage.[43] Understanding fundamentally how defects influence the properties of p-type $CuCrO_2$ will allow for a greater understanding of how such defect states may impede or enhance the material's ability to perform as a cathodic material in Li-ion batteries. ***Chapter 5*** explores proposed research directions based on preliminary results. This includes varying the pH of $CuCrO_2$ washing solutions, and how exposure to an acidic environment may influence the defect states present in the material and the resulting surface charge and measured specific capacity. Other research directions discussed include but are not limited to morphologically tuning delafossite $CuCrO_2$ and the resulting effects on electrochemical characterization, as well as approaches that can be explored to improve the cycling stability of $CuCrO_2$. Furthermore, the efficiency and overall performance of solar cells and Li-ion batteries can be refined for commercial application based on the results sought by this research.

### *1.7 References*

1. Tao, C. S.; Jiang, J.; Tao, M. Natural Resource Limitations to Terawatt-Scale Solar Cells. *Sol. Energy Mater. Sol. Cells* **2011**, *95* (12), 3176–3180.
2. McKone, J. R.; Crans, D. C.; Martin, C.; Turner, J.; Duggal, A. R.; Gray, H. B. Translational Science for Energy and Beyond. *Inorg. Chem.* **2016**, *55* (18), 9131–9143.
3. Lewis, N. S. Introduction: Solar Energy Conversion. *Chem. Rev.* **2015**, *115* (23), 12631–12632.
4. Sivula, K. Solar-to-Chemical Energy Conversion with Photoelectrochemical Tandem Cells. *Chimia (Aarau)* **2013**, *67* (3), 155–161.
5. Holmes, A.; Fletcher, N. From Sunlight to Electricity. Australian Academy of Science. https://www.science.org.au/curious/technology-future/solar-pv.
6. Crabtree, G. W.; Lewis, N. S. Solar Energy Conversion. *Physics Today* **2007**, *60* (3), 37–42.
7. Shockley, W.; Queisser, H. J. Detailed Balance Limit of Efficiency of *P-n* Junction Solar Cells. *J. Appl. Phys.* **1961**, *32* (3), 510–519.
8. Padilha, L. A.; Stewart, J. T.; Sandberg, R. L.; Bae, W. K.; Koh, W.-K.; Pietryga, J. M.; Klimov, V. I. Carrier Multiplication in Semiconductor Nanocrystals: Influence of Size, Shape, and Composition. *Acc. Chem. Res.* **2013**, *46* (6), 1261–1269.
9. Ahmed, I.; Shi, L.; Pasanen, H.; Vivo, P.; Maity, P.; Hatamvand, M.; Zhan, Y. There Is Plenty of Room at the Top: Generation of Hot Charge Carriers and Their Applications in Perovskite and Other Semiconductor-Based Optoelectronic Devices. *Light Sci. Appl.* **2021**, *10* (1), 174.
10. O'Regan, B.; Grätzel, M. A Low-Cost, High-Efficiency Solar Cell Based on Dye-Sensitized Colloidal $TiO_2$ Films. *Nature* **1991**, *353* (6346), 737–740.
11. Sharma, K.; Sharma, V.; Sharma, S. S. Dye-Sensitized Solar Cells: Fundamentals and Current Status. *Nanoscale Res. Lett.* **2018**, *13* (1), 381.
12. Zablocki, A. Fact Sheet, Energy Storage, 2019. Environmental and Energy Study Institute. https://www.eesi.org/papers/view/energy-storage-2019.
13. How Does a Lithium-ion Battery Work?, 2017. Office of Energy Efficiency and Renewable Energy. https://www.energy.gov/eere/articles/how-does-lithium-ion-battery-work.
14. Nagarajan, R.; Draeseke, A. D.; Sleight, A. W.; Tate, J. *P* -Type Conductivity in $CuCr_{1-x}Mg_xO2$ Films and Powders. *J. App. Phys.* **2001**, *89* (12), 8022–8025.
15. Zhen, C.; Wu, T.; Chen, R.; Wang, L.; Liu, G.; Cheng, H.-M. Strategies for Modifying $TiO_2$ Based Electron Transport Layers to Boost Perovskite Solar Cells. *ACS Sustainable Chem. Eng.* **2019**, *7* (5), 4586–4618.
16. Bai, Y.; Mora-Seró, I.; De Angelis, F.; Bisquert, J.; Wang, P. Titanium Dioxide Nanomaterials for Photovoltaic Applications. *Chem. Rev.* **2014**, *114* (19), 10095–10130.
17. Toyoda, T.; Shen, Q. Quantum-Dot-Sensitized Solar Cells: Effect of Nanostructured TiO2 Morphologies on Photovoltaic Properties. *J. Phys. Chem. Lett.* **2012**, *3* (14), 1885–1893.
18. Yang, Y.; Ling, Y.; Wang, G.; Liu, T.; Wang, F.; Zhai, T.; Tong, Y.; Li, Y. Photohole Induced Corrosion of Titanium Dioxide: Mechanism and Solutions. *Nano Lett.* **2015**, *15* (10), 7051–7057.
19. Hernández, S.; Hidalgo, D.; Sacco, A.; Chiodoni, A.; Lamberti, A.; Cauda, V.; Tresso, E.; Saracco, G. Comparison of Photocatalytic and Transport Properties of $TiO_2$ and ZnO

Nanostructures for Solar-Driven Water Splitting. *Phys. Chem. Chem. Phys.* **2015**, *17* (12), 7775–7786.

20. Dette, C.; Pérez-Osorio, M. A.; Kley, C. S.; Punke, P.; Patrick, C. E.; Jacobson, P.; Giustino, F.; Jung, S. J.; Kern, K. $TiO_2$ Anatase with a Bandgap in the Visible Region. *Nano Lett.* **2014**, *14* (11), 6533–6538.
21. Nitta, N.; Wu, F.; Lee, J. T.; Yushin, G. Li-Ion Battery Materials: Present and Future. *Materials Today* **2015**, *18* (5), 252–264.
22. Jain, A.; Ong, S. P.; Hautier, G.; Chen, W.; Richards, W. D.; Dacek, S.; Cholia, S.; Gunter, D.; Skinner, D.; Ceder, G.; Persson, K. A. Commentary: The Materials Project: A Materials Genome Approach to Accelerating Materials Innovation. *APL Materials* **2013**, *1* (1), 011002.
23. Jiang, T.; Li, X.; Bujoli-Doeuff, M.; Gautron, E.; Cario, L.; Jobic, S.; Gautier, R. Modulation of Defects in Semiconductors by Facile and Controllable Reduction: The Case of p-Type $CuCrO_2$ Nanoparticles. *Inorg. Chem.* **2016**, *55* (15), 7729–7733.
24. Dimple, D.; Lebègue, S.; Pastore, M. Dye Anchoring on CuCrO2 Surfaces for P-Type Dye-Sensitized Solar Cell Applications: An Ab Initio Study. *ACS Appl. Energy Mater.* **2021**, *4* (6), 6180–6190.
25. Kim, J.; Kendall, O.; Ren, J.; Murdoch, B. J.; McConville, C. F.; van Embden, J.; Della Gaspera, E. Highly Conductive and Visibly Transparent P-Type $CuCrO_2$ Films by Ultrasonic Spray Pyrolysis. *ACS Appl. Mater. Interfaces* **2022**, *14* (9), 11768–11778.
26. Sun, M.; Shu, J.; Zhao, C.; Wu, J.; Guo, H.; Guo, Y.; Yin, X.; Lin, Y.; Tan, Z.; He, M.; Wang, L. Interface Modification with $CuCrO_2$ Nanocrystals for Highly Efficient and Stable Planar Perovskite Solar Cells. *ACS Appl. Mater. Interfaces* **2022**, *14* (11), 13352–13360.
27. Kawazoe, H.; Yasukawa, M.; Hyodo, H.; Kurita, M.; Yanagi, H.; Hosono, H. P-Type Electrical Conduction in Transparent Thin Films of $CuAlO_2$. *Nature* **1997**, *389* (6654), 939–942.
28. Hautier, G.; Miglio, A.; Ceder, G.; Rignanese, G.-M.; Gonze, X. Identification and Design Principles of Low Hole Effective Mass P-Type Transparent Conducting Oxides. *Nat. Commun.* **2013**, *4* (1), 2292.
29. Zhao, R.-D.; Zhang, Y.-M.; Liu, Q.-L.; Zhao, Z.-Y. Effects of the Preparation Process on the Photocatalytic Performance of Delafossite $CuCrO_2$. *Inorg. Chem.* **2020**, *59* (22), 16679–16689.
30. Elgrishi, N.; Rountree, K. J.; McCarthy, B. D.; Rountree, E. S.; Eisenhart, T. T.; Dempsey, J. L. A Practical Beginner’s Guide to Cyclic Voltammetry. *J. Chem. Educ.* **2018**, *95* (2), 197–206.
31. Helmholtz, H. Ueber Einige Gesetze Der Vertheilung Elektrischer Ströme in Körperlichen Leitern Mit Anwendung Auf Die Thierisch-Elektrischen Versuche. *Annalen der Physik* **1853**, *165* (6), 211–233.
32. Dunwell, M.; Yan, Y.; Xu, B. Understanding the Influence of the Electrochemical Double-Layer on Heterogeneous Electrochemical Reactions. *Curr. Opin. Chem. Eng.* **2018**, *20*, 151–158.
33. Sudhakar, Y. N.; Selvakumar, M.; Bhat, D. K. Chapter 4 - Biopolymer Electrolytes for Solar Cells and Electrochemical Cells. *Biopolymer Electrolytes* **2018**; pp 117–149.
34. Richardson, T. J. Secondary Batteries – Lithium Rechargeable Systems – Lithium-Ion, Overcharge Protection Shuttles. In *Encyclopedia of Electrochemical Power Sources* **2009**; pp 404–408.

35. Tomiyasu, H.; Shikata, H.; Takao, K.; Asanuma, N.; Taruta, S.; Park, Y.-Y. An Aqueous Electrolyte of the Widest Potential Window and Its Superior Capability for Capacitors. *Sci. Rep.* **2017**, *7* (1), 45048.
36. Boschloo, G.; Hagfeldt, A. Characteristics of the Iodide/Triiodide Redox Mediator in Dye-Sensitized Solar Cells. *Acc. Chem. Res.* **2009**, *42* (11), 1819–1826.
37. Bredar, A. R. C.; Chown, A. L.; Burton, A. R.; Farnum, B. H. Electrochemical Impedance Spectroscopy of Metal Oxide Electrodes for Energy Applications. *ACS Appl. Energy Mater.* **2020**.
38. Bredar, A. R. C.; Blanchet, M. D.; Comes, R. B.; Farnum, B. H. Evidence and Influence of Copper Vacancies in P-Type $CuGaO_2$ Mesoporous Films. *ACS Appl. Energy Mater.* **2019**, *2* (1), 19–28.
39. Almoiqli, M. Nanostructured ICP-CNT Electrodes for Capacitive Deionisation and Water Clean Up. Doctor of Philosophy thesis, Intelligent Polymer Research Institute, Department of Chemistry, University of Wollongong, Australia. **2014**.
40. Richard, K. Chronoamperometry. *Analytical Chemistry: The Basic Concepts*. Chemistry LibreTexts; **2020**. https://chem.libretexts.org/Bookshelves/Analytical_Chemistry/Supplemental_Modules_(Analytical_Chemistry)/Analytical_Sciences_Digital_Library/JASDL/Courseware/Analytical_Electrochemistry%3A_The_Basic_Concepts.
41. Mortimer, R. J. Spectroelectrochemistry, Methods and Instrumentation. In *Encyclopedia of Spectroscopy and Spectrometry (Third Edition)*; Lindon, J. C., Tranter, G. E., Koppenaal, D. W., Eds.; Academic Press: Oxford, **2017**; pp 172–177.
42. Bansal, N. AD-A 274 776 ( 1 Chronopotentiometry of Refractory Metals 1 . . . Actinides and Oxyanions in Molten Salts : A Review. Chemistry, Materials Science. https://www.semanticscholar.org/paper/AD-A-274-776-(-1-Chronopotentiometry-of-Refractory-Bansal/6f00c1d93b16bfa925ff32c10817d840c9836c9e.
43. Ma, J.; Li, W.; Morgan, B. J.; Światowska, J.; Baddour-Hadjean, R.; Body, M.; Legein, C.; Borkiewicz, O. J.; Leclerc, S.; Groult, H.; Lantelme, F.; Laberty-Robert, C.; Dambournet, D. Lithium Intercalation in Anatase Titanium Vacancies and the Role of Local Anionic Environment. *Chem. Mater.* **2018**, *30* (9), 3078–3089.

# Chapter 2

# Overview of EIS for Ion Battery Applications

*This chapter was reproduced from the following publication:

Bredar, A.R.C.†; Chown, Amanda L.†; Burton, Andricus†; Farnum, Byron H.

*ACS Appl. Energy Mater*. **2020**, 3 (1), 66-98 †Equal Contribution

## *2.1. Overview*

A variety of metal oxides have been studied as cathodes and anodes in rechargeable ion batteries used for electrochemical energy storage.[1–50] EIS can be a useful technique for researching these materials by providing insight on corrosion rate of the metal oxide electrode during multiple charge and discharge cycles (i.e. long term cycling efficiency) and ion diffusion into the metal oxide. The most well-studied type of ion battery using EIS is the Li-ion battery[20–27,51–57] due to its commercialization in many portable electronics, however, other Na-ion[1,6,15,28,32,58] and divalent ion batteries, particularly Zn-ion batteries,[49,50,59–61] have also been investigated using this technique. Lithium ion batteries primarily consist of a cathode, anode, and lithium containing electrolyte present in the form of a solution, solid, or gel electrolyte.[62] The cathode material consists of a lithiated transition metal oxide and the anode is typically graphite, however, researchers have also explored anodic metal oxides.[63] Upon charging the battery, oxidation of the transition metal oxide cathode is coupled with de-intercalation of $Li^+$ ions. Concomitantly, reduction of the anode results in $Li^+$ intercalation between graphite layers. Redox half reactions for each of these processes are shown in **Equations 2.1-2.2** for the case of a $LiCoO_2$ cathode and graphite (C) anode. As lithium ions are transferred between electrodes, electrochemical energy is stored as the potential difference between the electrodes is increased. During discharge, intercalation of $Li^+$ occurs at the cathode upon reduction and de-intercalation occurs at the anode upon oxidation.

$Li_{1-x}CoO_2 + xLi^+ + xe^- \rightarrow LiCoO_2$ Cathode **eq. 2.1)**

$C + xLi^+ + xe^- \rightarrow Li_xC$ Anode **eq. 2.2)**

The reversibility of this process depends greatly on the structure and electrochemical properties of the metal oxide cathode. Oxides such as $LiCoO_2$, $LiNiO_2$, and $LiMnO_2$ possess layered structures where $Li^+$ ions are able to diffuse in and out of the host oxide.[2,39–41,43,58] Other important oxides such as spinel $LiMn_2O_4$ and it substituted derivatives (e.g. $LiNi_{0.5}Mn_{1.5}O_4$) possess interstitial sites where the occupancy by $Li^+$ is variable.[21,22,64–67] Importantly, the charge storage capacity of a metal oxide host is limited to the reversible solid-solution range of $Li^+$ intercalation in the cathode host structure for a given redox potential of the transition metal cation.[62]

Important features of ion battery electrodes which have been studied by EIS include formation of passivation layers at the surface of cathodes and anodes, charge transfer to the metal oxide electrode, and $Li^+$ diffusion in the solid state. Passivation layers, also known as solid electrolyte interface (SEI) layers in the Li-ion battery literature, are routinely observed on the cathode and anode surface due to chemical reactivity between the electrodes and electrolyte. The SEI layer can have both detrimental and beneficial effects, including loss in battery capacity over time but enhancement of the cycling efficiency. The formation of passivation layers is modeled using additional parallel R||C circuits such as Models B and C discussed above.[41] Importantly, the resistance of the SEI layer is believed to be the result of Li-ion migration through the layer the growth of such layers over extended cycles leads to higher resistance.[7,22,24,38,53–55] The impedance of solid state ion diffusion, on the other hand, is described by a Warburg element at low frequency.[16,31,39,44,68] **Figure 2.1** shows a description of this behavior provided by Aurbach et al. where the additional arc assigned to formation of a passivation layer (i.e. surface film) occurs at high frequency while the charge transfer resistance associated with energy storage appears in the mid-frequency range.[68] Note that the linear portion at low frequency reveals information about $Li^+$ diffusion as described by Warburg impedance.

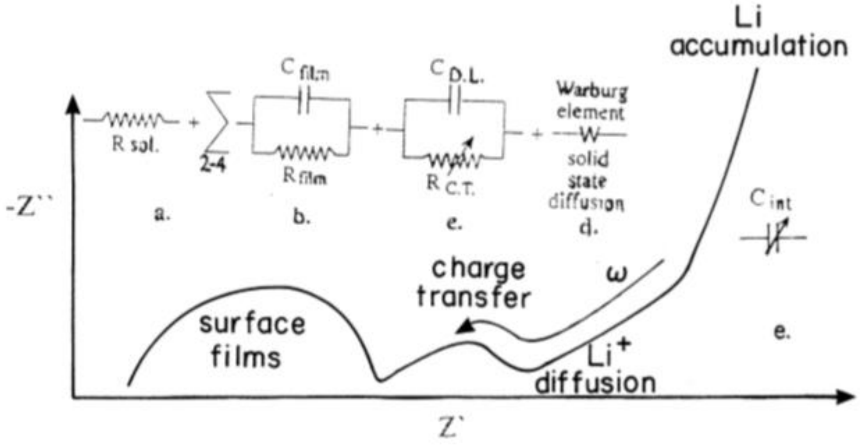

**Figure 2.1.** A general impedance spectra illustration for lithiated electrode and the equivalent circuit analog. Reprinted with permission from Elsevier.[68]

In the following sections we discuss specific examples of EIS studies on metal oxides used as cathode and anode materials. We do not cover every example available in the literature and instead give a brief discussion of examples which use EIS to elucidate particularly important features of metal oxide electrodes in the context of ion batteries.

### *2.2. Li-Ion Cathode Materials*

Lithium cobalt oxide is the archetype cathode material for Li-ion batteries.[62,69,70] This layered oxide allows for a variable number of $Li^+$ ions to intercalate between layers of edge-shared cobalt oxide octahedra upon local redox changes in the cobalt oxidation state.[40,71–73] Early studies by Goodenough revealed the presence of passivating surface layers that form by adsorption/decomposition of the electrolyte on the surface of $LiCoO_2$.[41] The observed EIS data revealed two semicircles (**Figure 2.2**), a deviation from the expected response of one semicircle representing charge transfer to the transition metal and a high frequency linear region describing diffusion of $Li^+$. The new semicircle appeared at high frequency and increased in size over time. A thorough comparison of equivalent circuit models to account for the second arc resulted in the proposed equivalent circuit shown in **Figure 2.2**. Here, a second R||C circuit is included to account for surface layer formation ($R_{sl}$, $C_{sl}$) and a second Warburg diffusion element is included to account for diffusion of $Li^+$ within the porous electrode structure ($Z'_W$). The surface layer formation was attributed to polymerization of propylene carbonate at the electrode surface with $R_{sl}$ increasing over a 22 hour period as the layer grew in thickness.

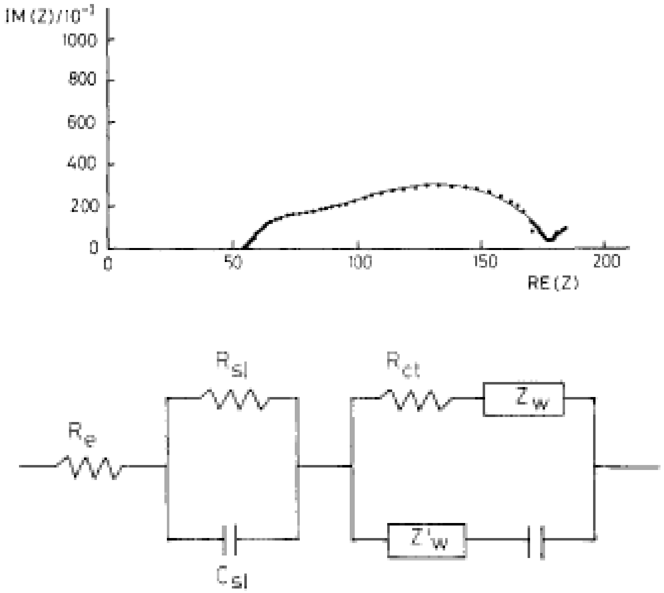

**Figure 2.2. (top)** Nyquist plot showing ESI data for a $Li_{0.65}CoO_2$ cathode at potentials up to 4.5 V vs. lithium and **(bottom)** the equivalent circuit used for fitting. The parallel $R_{sl}||C_{sl}$ circuit describes

the presence of a surface layer on the electrode with a high frequency response. Reprinted with permission from the Electrochemical Society.[41]

Another common observation of Li-ion battery cathodes is an increase in $R_{ct}$ associated with oxidation/reduction of the transition metal over an extended number of charge-discharge cycles.[23,24,40] This observation has been attributed to decomposition of the cathode material, which leads to losses in energy storage. Zhang et al. studied $LiCoO_2$ with a $Li_{10}GeP_2S_{12}$ solid state electrolyte where EIS was used to analyze capacitance fade and increased impedance at the cathode/solid electrolyte interface after being subjected to long-term cycling.[23] Overall, batteries experienced a loss of ~10% storage capacity over the first 100 cycles. **Figure 2.3** shows Nyquist plots collected at the beginning and end of this cycling range where all three semicircle arcs are observed to increase in size after 100 cycles. The mid frequency arc was assigned to charge transfer with the LiCoO2 cathode which increased from 9 $\Omega$ cm$^2$ to 118 $\Omega$ cm$^2$ along with a decreased capacitance. Scanning electron microscopy found that $LiCoO_2$ particles were fractured following extended cycling, hypothesized to result in a loss of contact with the solid-state electrolyte. Electron energy loss spectroscopy also showed migration of cobalt ions from $LiCoO_2$ into the SEI layer which grew in size over the cycling range. This growth can be observed by large increase in resistance for the high frequency arc in the Nyquist plot. The low frequency arc was assigned to the anode/electrolyte interface.

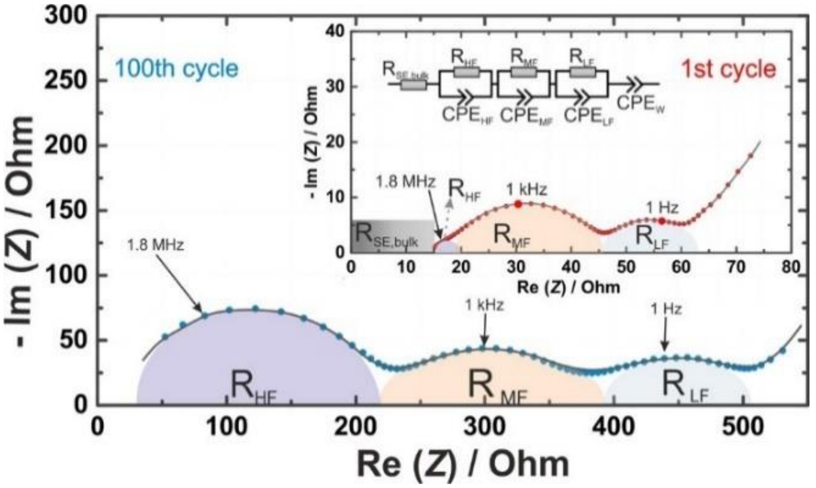

**Figure 2.3.** Nyquist plots after 1 charge cycle **(inset)** vs. 100 charge cycles at 3.6 V vs. In/InLi. After 100 cycles, decomposition of the $LiCoO_2$ cathode during cycling was observed as an increase in resistance for the semicircle arc in the mid frequency region, while formation of a surface layer at the $LiCoO_2$/electrolyte interface was observed as an increase in resistance for the arc at high frequency. Reprinted with permission from the American Chemical Society.[23]

Lou et al. have followed the decomposition of $LiCoO_2$ and the formation of surface layers using energy dispersive spectroscopy (EDS) and EIS as a function of cycle number.[24] Batteries were charged and discharged at 0.6 C (C = charge rate) with a 30% depth of discharge for 100, 400, 800, 1600, 2000 and 2400 cycles. The O:Co ratio rose from 2.34 to 2.96 as the cycling proceeded which suggested slow SEI growth as the cycle number increased. The SEI layer was hypothesized to consist of $Li_2CO_3$ based on FTIR data in conjunction with the increase in oxygen content. We note that the ratio may also be explained by a loss of cobalt from the metal oxide. Consistent with results discussed in other studies, the Nyquist plots for EIS data showed a steady increase in both the high frequency arc assigned to resistance ($R_p$) of the SEI layer and the mid frequency arc assigned to charge transfer with $LiCoO_2$ ($R_{ct}$). The linear feature at low frequency was assigned to Warburg diffusion of $Li^+$ ions, however, this feature was not modeled in this study.

Efforts to stabilize cathodes from decomposition and formation of passivating surface layers have focused on the use of additives to the battery electrolyte.[21,24,30,31,37,40] As a recent example, Wu et al. compared EIS data of $LiCoO_2$ cathodes and graphite anodes with and without the additive 4-propyl-[1,3,2]dioxathiolane-2,2-dioxide (PDTD) over multiple charge-discharge cycles. As seen in **Figure 2.4**, there was a significant increase in surface layer resistance ($R_f$) and $R_{ct}$ over 150 cycles for both $LiCoO_2$ and graphite. However, the presence of PDTD as an additive stabilized both electrodes, exhibiting smaller increases in $R_f$ and $R_{ct}$ over the same cycling period. The influence of PDTD is thought to help stabilize the $LiCoO_2$ surface from leaching cobalt ions and forming surface layers.[40]

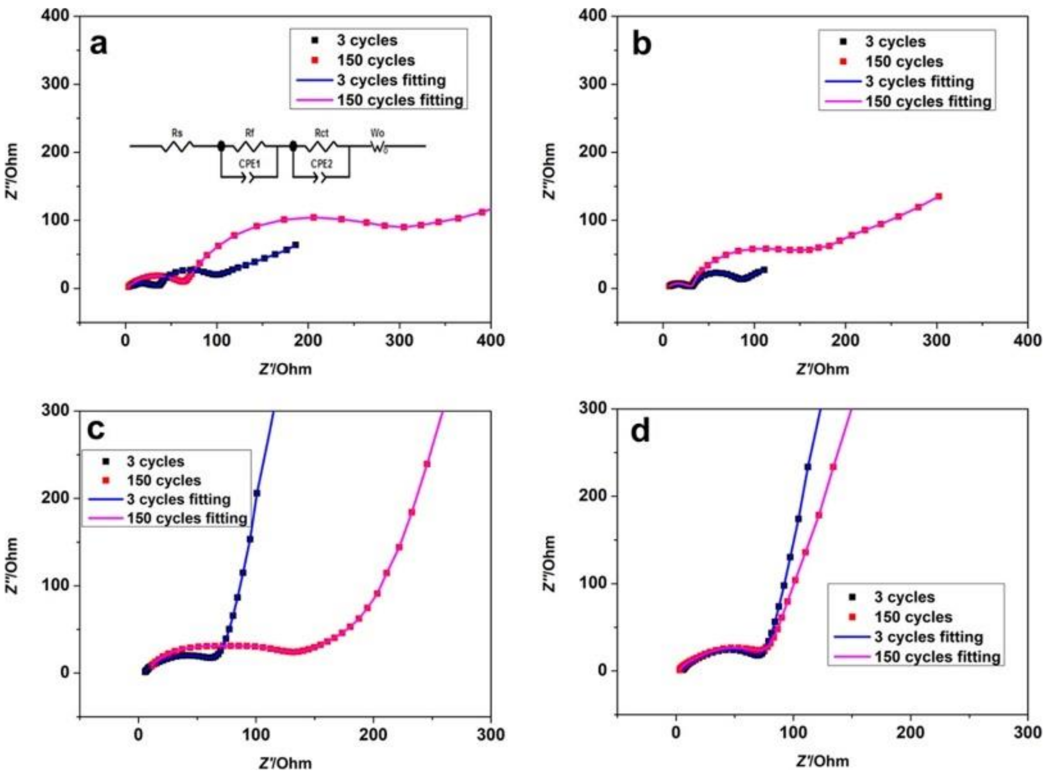

**Figure 2.4.** Nyquist plots showing discharge of $LiCoO_2$ cathodes **a)** and graphite anodes **b)** collected in electrolytes without **c)** and with **d)** the additive PDTD at the discharge state (~3.0 V). Large increases in $R_f$ and $R_{ct}$ without PDTD indicated decomposition of the electrodes over extended cycles. Inclusion of PDTD limited these increases over the same cycling period. Reprinted with permission from the American Chemical Society.[40]

In other studies of $LiCoO_2$, controlling the porosity and grain size of the electrode has been found to influence the EIS results.[2,13,25] Annealing $Co_3O_4$ and CoO at 350 °C resulted in optimal Li storage performance with high discharge capacities and good long-term cycling stability; at higher annealing temperatures, a larger grain size was attainable which led to a smaller semicircle in the EIS data indicating low resistance from surface film formation.[2]

Electron transport through the metal oxide may also be observed by EIS, however, most electrodes are designed to be highly conductive by mixing the metal oxide with carbon black as a composite. Zhuang et al. was able to observe electron transport for $LiMn_2O_4$ as a function of both charging voltage (3.5 – 4.3 V) and temperature using EIS.[21] As with other Li-ion battery studies, three features were generally observed in the Nyquist plot: two semicircle arcs at high and middle frequencies and a linear Warburg feature at low frequency. These features were assigned to Li-ion migration through the SEI film, charge-transfer through the electrode/electrolyte interface, and solid-state diffusion of $Li^+$ ions in the electrode matrix, respectively. However, over the potential range of 3.5 - 3.7 V, an additional semicircle arc in the middle-to-high frequency region was observed. To investigate the origins of this feature, EIS experiments were performed as a function of temperature. Below 20 $^{o}$C, the middle-to-high arc could frequency be well resolved, however, above 20 °C, the semicircles in the high and middle-to-high frequency ranges began to overlap. This suggested that the semicircle observed in the high frequency region at room temperature may actually be comprised of two distinct features, as seen in **Figure 2.5**. These two features were proposed to be due to Li-ion migration through the SEI film at high frequency, as is typically discussed, and electronic transport through the cathode at middle-to-high frequency. Also notable in this study is the predictable dependence of charge transfer resistance and Warburg diffusion as a function of temperature. For low temperatures, $R_{ct}$ is quite large and therefore Warburg diffusion cannot be observed over the finite frequency range. However, as the temperature is increased, $R_{ct}$ drops precipitously and the Warburg feature can be clearly observed.

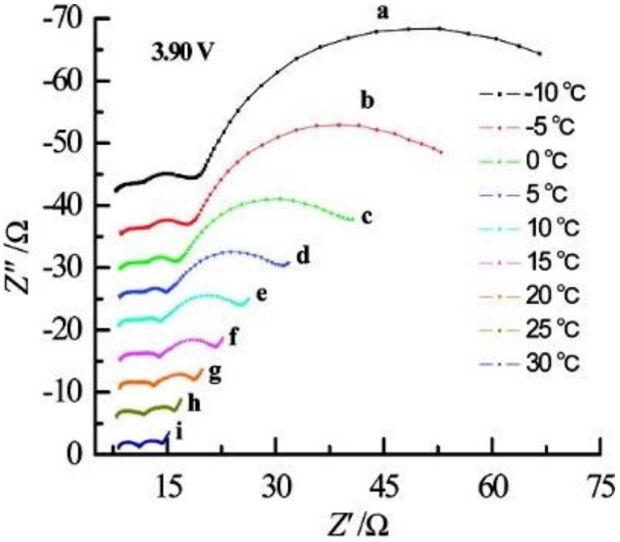

**Figure 2.5.** Nyquist plots at various temperatures for a spinel $LiMn_2O_4$ cathode at 3.90 V. At low temperatures, a third semicircle arc was observed in the middle-to-high frequency range assigned to electron transport inside the cathode. Reprinted with permission from the American Chemical Society.[21]

### *2.3. Li-Ion Anode Materials*

Copper(II) oxide has been studied as an anode material for Li-ion batteries where the reduction of copper(II) to copper metal results in reversible formation of $Li_2O$ according to the reaction $CuO + 2Li^+ + 2e^- \rightarrow Cu + Li_2O$. The morphological dependence of the CuO electrode has been a particular area of focus in terms of EIS studies.[31,32,35,54,74] Wang et al. have investigated the difference in electrochemical behavior of leaf-like, oatmeal-like, and hollow-spherical CuO structures.[35] SEM images are provided in **Figure 2.6** to show morphological differences among the CuO samples. Charge storage capacity and long-term cycling efficiency was found to be weakest for the oatmeal-like structure and EIS was able to provide justification for these results. Figure 2.6 shows Nyquist plots collected for each structure along with the equivalent circuits used to model these data. A noticeably larger $R_f$ resistance was observed for the oatmeal structure ($R_f$

= 321.1 Ω) than the leaf ($R_f$ = 45.7 Ω) and hollow-sphere (Rf = 43.8 Ω) structures. Similar to the discussion above for cathode materials, the $R_f$ resistance is attributed to the formation of a passivation layer at the solid/electrolyte interface, which are attributed to decreased charge storage capacity. The lower porosity of the oatmeal structure was proposed to be the main culprit in the higher surface film resistance.

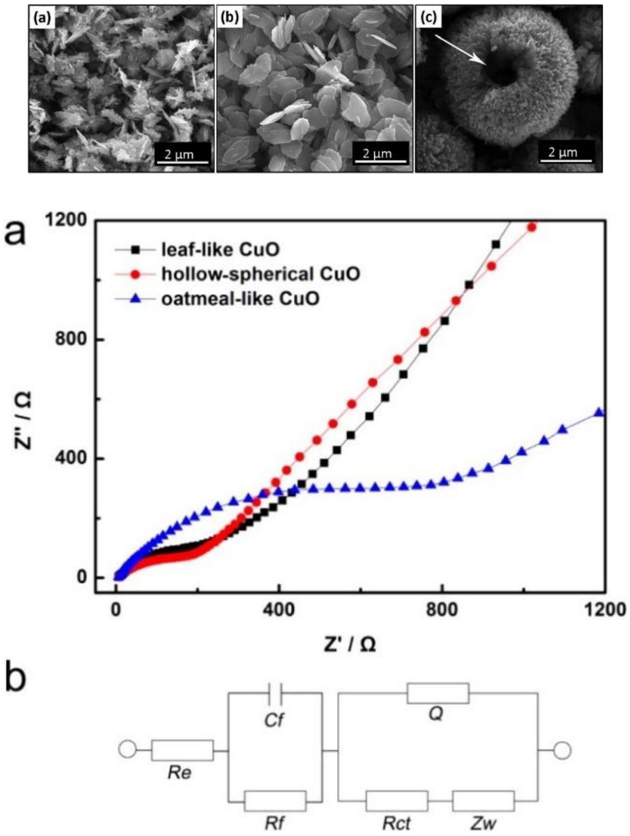

**Figure 2.6. (top)** SEM images of CuO after calcination with **a)** leaf-like, **b)** oatmeal-like, and **c)** hollow-spherical morphologies. **(middle)** Nyquist plots of CuO samples showing a higher surface film resistance in the oatmeal-like structure at the open circuit potential. **(bottom)** Equivalent circuit used for modeling. Reprinted with permission from the American Chemical Society.[35]

While the morphology of the anode can impact the charge storage capacity and cycling efficiency, the nanostructure of the SEI layer on the anode also affects the electrochemical behavior of the battery during cycling and can be analyzed using EIS. Huang et al. studied the formation of the SEI layer on CuO nanowires following the conversion of CuO to Cu and $Li_2O$.[38] A Nyquist plot is shown in **Figure 2.7** where the formation of the SEI layer can be observed as a function of the applied potential vs $Li^+$/Li. At potentials greater than 1.0 V, the impedance response was capacitive from charge accumulation on the CuO electrode. However, once a potential of 1.0 V was applied, CuO was reduced to Cu and $Li_2O$ and a depressed semicircle was observed, characteristic for the formation of an SEI layer. As the potential was lowered from 1.0 V to 0.025 V, the semicircle became more well defined. It was determined that as the potential begins to approach 0 V, the ionic resistance for $Li^+$ migration through the SEI layer decreased, however, the thickness of the layer increased. This was determined by transmission electron microscopy collected for samples after each applied potential. The thickness of the SEI layer grew from 3 nm at 1.0 V vs $Li^+$/Li to 14 nm upon deposition of Li metal. The decrease in ionic resistance was proposed to be the result of a dense, ionically conductive amorphous layer at lower potentials and highlighted the importance of the structure of the SEI layer and not just its thickness.

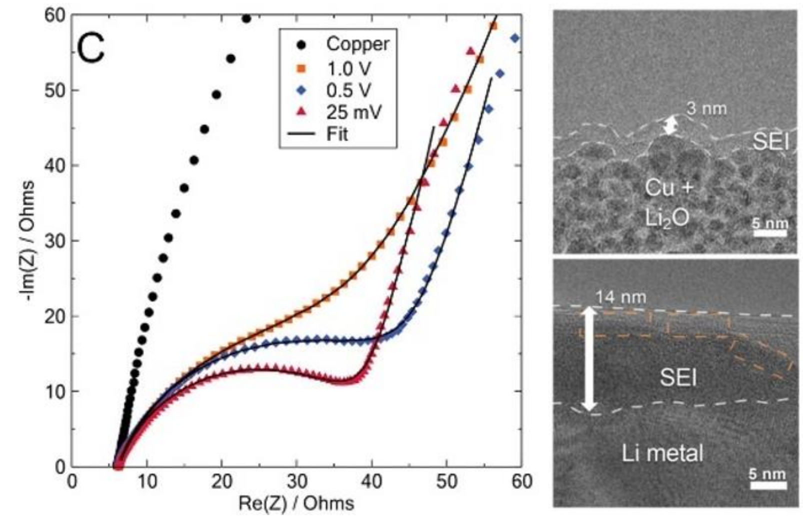

**Figure 2.7. (left)** Nyquist plots before the growth of SEI (Copper) in addition to SEI formation at 1.0 V, 0.5 V, and 0.025 V vs. Li/Li$^+$. Transmission electron micrographs of electrode surfaces following an applied potential of 1.0 V **(top right)** and < 0.0 V **(bottom right)** showing the formation of the SEI layer. Reprinted with permission from the American Chemical Society.[38]

$TiO_2$ has also been an interesting material studied for anode applications in Li-ion batteries, but as the direct anode and as a coating material for the anode to enhance overall stability and performance.[75–78] Qiu et al. used EIS to study $TiO_2$ reduced graphite nanocomposites as the active anode material in Li-ion batteries. The conductivity of the reduced graphene oxide nanosheets was found to facilitate the charge-transfer process in Li-ion batteries.[78] As an anode material, the structural and morphological characteristics of oxygen deficient anatase $TiO_2$ using EIS has been reported.[79–84] Liu et al. studied $TiO_2$ electrodes in an aqueous Li-ion battery and the decomposition of inorganic compounds (LiF, $Li_2CO_3$, and $Li_2O$) on the surface of $TiO_2$ using EIS in conjunction to scanning electron microscopy.[84] Balogun et al. studied the capacity and long term cycling capabilities of oxygen-deficient $TiO_2$/$Li_4Ti_5O_{12}$ ($TiO_2$/LTO) where $Li_4Ti_5O_{12}$ is a chemically lithiated phase grown from $TiO_2$.[82] $Li_4Ti_5O_{12}$ is of interest because of its well-defined potential for

$Li^+$ intercalation at 1.55 V vs $Li^+/Li$. Comparison of $TiO_2$ nanosheets and $TiO_2$/LTO nanosheet electrodes with and without annealing under an $H_2$ environment (H-$TiO_2$/LTO) revealed the lowest charge transfer resistance for H-$TiO_2$/LTO electrodes and the highest $R_{ct}$ for $TiO_2$ electrodes. This was attributed to a higher concentration of oxygen vacancies in the H-$TiO_2$/LTO electrode, as measured by XPS and TGA experiments.

### *2.4. Na-Ion and Zn-Ion Batteries*

Various monovalent and divalent ions in addition to $Li^+$ have been explored in metal oxide ion battery research. In particular, $Na^+$ has been frequently used as a monovalent ion in studying electrochemical performance of battery materials via EIS.[85] Huang et al. explored silver-containing α-$MnO_2$ cathode derivatives, $Ag_xMn_8O_{16}$, where x = 1.22 or 1.66 as a host material for intercalation of $Li^+$ and $Na^+$.[58] These oxides possess a 2 x 2 tunnel structure where cations can intercalate. The use of $Ag^+$ further controls tunnel size and helps stabilize the structure. EIS studies showed that a significant decrease was observed in $R_{ct}$ associated with charge transfer to the oxide when $Na^+$ intercalated in and out of the structure (**Figure 2.8**). $R_{ct}$ stabilized at a consistent value once 4 electron equivalents of $Na^+$ were intercalated into the structure of $Ag_{1.22}Mn_8O_{16}$ and 1 electron equivalent for $Ag_{1.66}Mn_8O_{16}$, showing that stable structures were obtained at these conditions. This data was contrasted with results for $Li^+$ intercalation where a gradual increase in $R_{ct}$ was observed as more $Li^+$ ions were incorporated. This result was explained based on the similar ionic radii of $Na^+$ and $Ag^+$, which led to very little structure displacement upon intercalation.

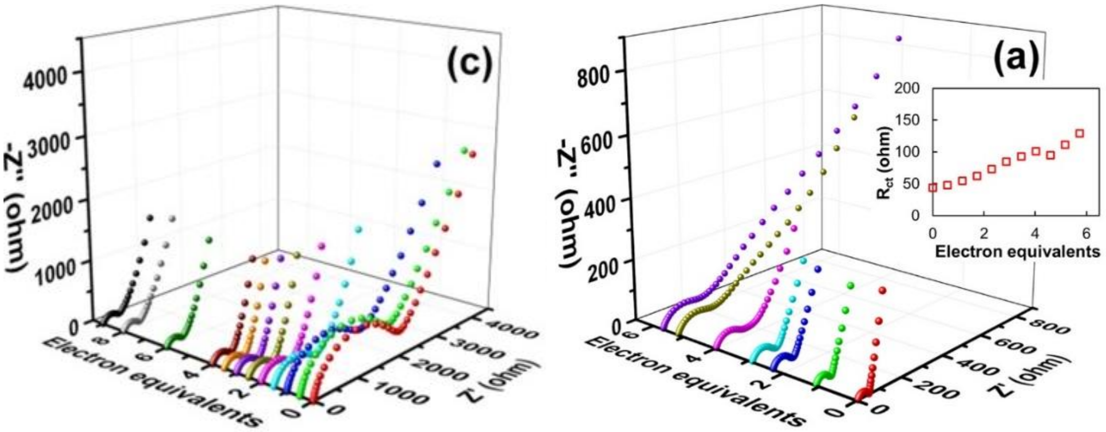

**Figure 2.8.** Comparison of Nyquist plots obtained from $Na^+$ intercalation **(left)** and $Li^+$ intercalation **(right)** into $Ag_{1.22}Mn_8O_{16}$ cathodes. Intercalation of $Na^+$ resulted in decreased charge transfer resistance and intercalation of $Li^+$ resulted in increased charge transfer resistance. Reprinted with permission from the American Chemical Society.[58]

Wang et al. has used EIS to compare $NaCrO_2$ (NCO) powders synthesized via a decomposition reaction, $NaCrO_2$ powders synthesized via a simple decomposition reaction followed by calcination (Ig-NCO) and a solid-state reaction (s-NCO) as cathode materials for Na-ion batteries.[28] These synthetic conditions produce different morphological which impact the capacity and long-term cycling capabilities of the materials. Studies using TEM and HRTEM reveal that Ig-NCO is made of large particles layered in multiple stacking sheets, whereas the s-NCO product is within the sub-micron range and has a flakelike particle morphology with distinct edges and an affinity to aggregate. F**igure 2.9** shows EIS curves of Ig-NCO and s-NCO cathodes in the charged state of 3.6 V after different cycles at 0.1 C (charge rate). The Nyquist plots reveal two semicircles and a linear feature which represent the resistance of the surface film $R_f$, the charge transfer resistance $R_{ct}$, and the Warburg impedance $Z_w$, respectively, as discussed previously for Li-ion battery EIS studies. As the cycling number increased from 50 to 500, $R_f$ for both oxides increased as the surface layer grew, however, $R_{ct}$ decreased for Ig-NCO and increased for s-NCO. The smaller charge transfer resistance observed in Ig-NCO was attributed to suppression of side reactions due to its small specific surface area and highly (110)-oriented morphology, allowing improved intercalation and deintercalation of $Na^+$ during cycling.[28]

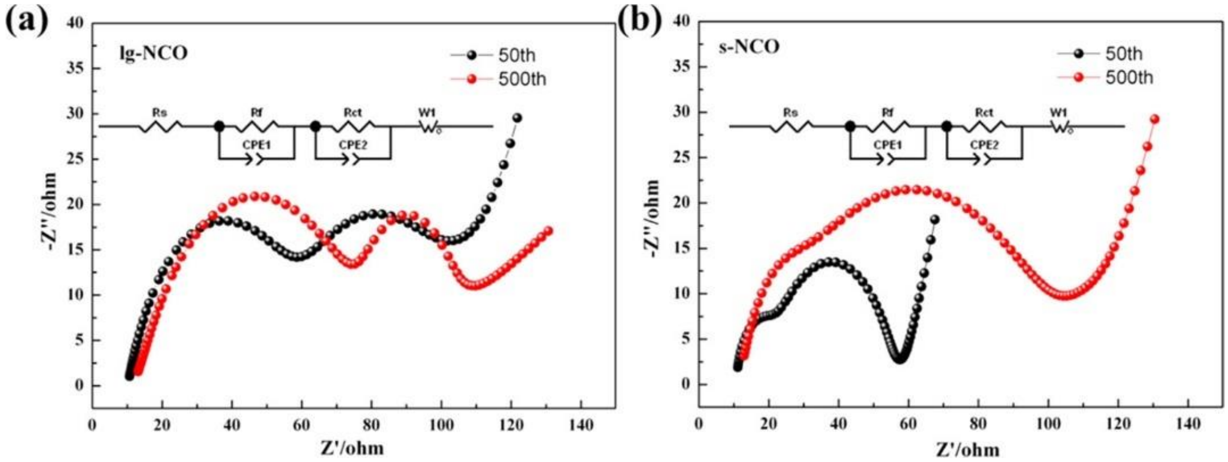

**Figure 2.9.** Nyquist plots and their respective equivalent circuits for Ig-NCO electrodes **(left)** and s-NCO electrodes **(right)** measured in the charged state of 3.6 V after a different number of cycles. Reprinted with permission from the American Chemical Society.[28]

Metal oxide anodes such as CuO have also been studied as anode materials for Na-ion batteries with similar reactivity as described for lithium (i.e. $CuO + 2Na^+ + 2e^- \rightarrow Cu + Na_2O$). Nanoflake, nanoellipsoid, and nanorod structures were compared by Rath et al. using EIS to determine the diffusion coefficients of $Na^+$ for each structure.[32] $R_{ct}$ at the electrode/electrolyte interface of the nanorods was significantly lower than what was observed in the other nanostructures, therefore, the Warburg diffusion feature could be clearly resolved. In this case, $Z_{Re}$ can be plotted directly versus $\omega^{-1/2}$ and the diffusion coefficient obtained from the slope based on **Equations 2.3-2.4**. **Figure 2.10** shows $Z_{Re}$ vs. $\omega^{-1/2}$ along with determined diffusion coefficients for each nanostructure. The larger diffusion coefficient determined for the nanorod morphology was attributed to a more favorable diffusion path along the length of the rod compared with the other nanostructures.

$$Z_{Re} = R_e + R_{ct} + \sigma\omega^{-\frac{1}{2}} \qquad \textbf{eq. 2.3)}$$

$$D_{Na^+} = \frac{R^2T^2}{2A^2n^4F^4C_0^2\sigma^2} \qquad \textbf{eq. 2.4)}$$

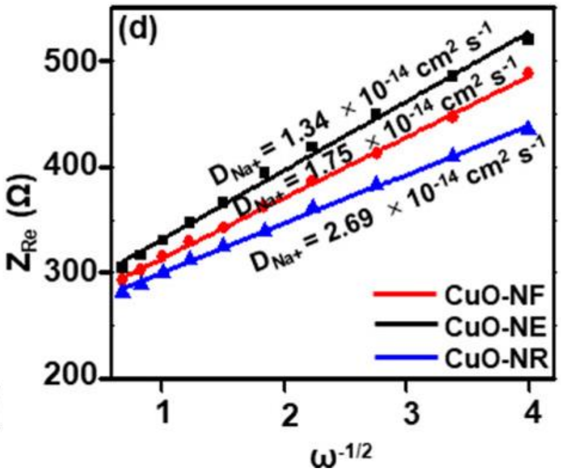

**Figure 2.10.** $Z_{Re}$ vs. $\omega^{-1/2}$ plot in the low frequency region for CuO nanorod, nanoellipsoid, and nanoflake electrodes used as anodes in Na-ion batteries. Reprinted with permission from the American Chemical Society.[32]

Exploration of divalent ion batteries using EIS have mostly focused on $Zn^{2+}$,[49,59,61,86] however, some studies have appeared for $Mg^{2+}$.[87–89] In the case of $ZnMnO_2$ batteries, correlations have been deduced using EIS between applied strain and the ionic conductivities of polyacrylamide hydrogel electrolytes.[60] When compressional strain was increased to 22.2%, a dramatic decrease in resistance was observed, which was attributed to a shortened ionic transport distance as the compressional strain increases, thereby improving the efficiency of ionic migration. Zn/$\delta$-$MnO_2$ cells have also been studied using EIS to compare different cycling points, with equivalent circuit models provided for fitting as seen in **Figure 2.11** to ultimately analyze the voltage and capacity of the material after long-term cycling.[50] The additional circuit component seen in equivalent circuit 2 represents the growth of an additional passivation layer which is likely due to electrolyte decomposition. During cycling, small changes were seen in the resistance due to the electrolyte and the capacitance for the passivation layer. $R_{ct}$ decreased and $CPE_{ct}$ increased up to 30 cycles which could be explained by an increase in the surface area of the active materials.

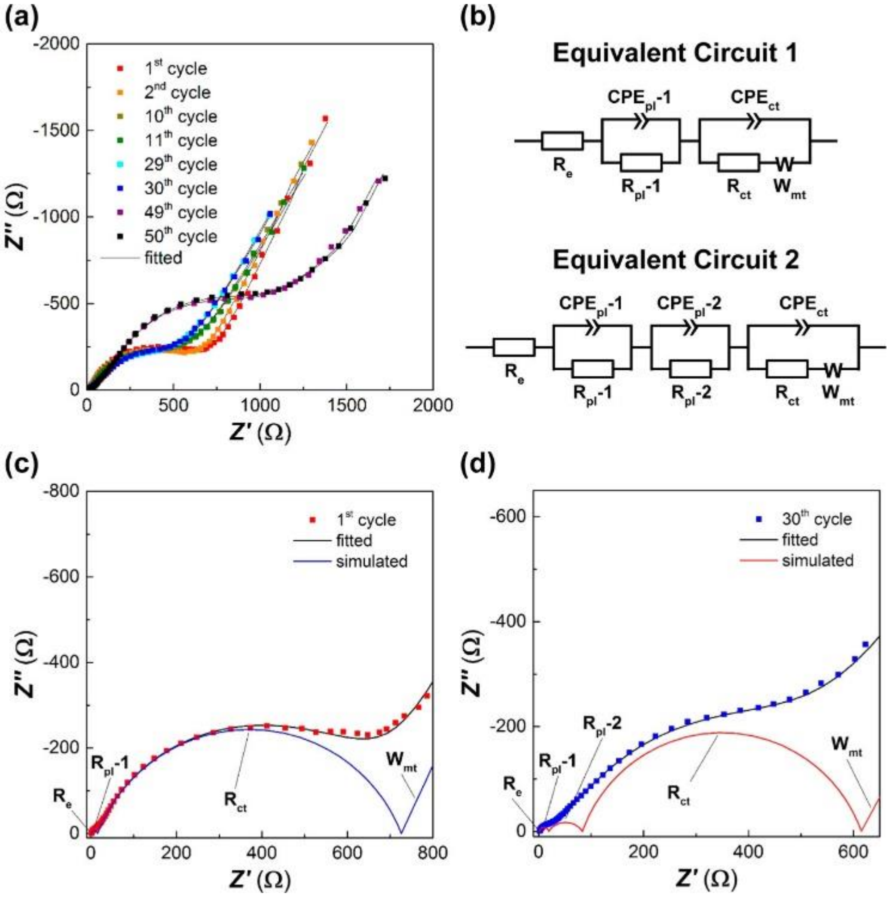

**Figure 2.11. (top left)** Nyquist plots of Zn/$\delta$-$MnO_2$ cells at different cycle numbers. **(top right)** Equivalent circuits. **(bottom left)** Nyquist plots zoomed in for the first cycle showing minimal

contribution for surface layers. **(bottom right)** Nyquist plots zoomed in for the 30th cycle showing larger contributions from surface layers. Reprinted with permission from the American Chemical Society.[50]

### *2.5. Conclusions and Outlook*

In conclusion, EIS is a highly versatile technique that can be used to study metal oxide electrodes in a wide variety of energy applications. The key feature of this electrochemical method is the frequency dependence exhibited by fundamental circuit elements used to describe the flow of current through the metal oxide interface. Modeling EIS data to well-supported equivalent circuits is a critical aspect toward gaining physically relevant information. Detailed studies as a function of modulation frequency and applied potential can reveal significant information about the capacitance of electronic states and their resistance for electron transfer.

In terms of ion batteries, understanding the role of surface passivation layers that occurs at anodes and cathodes is of great importance for energy storage. Extended battery cycling has shown a continuous increase in these layers which contributes to higher overall resistance for electrical energy storage and thus degraded battery performance. EIS has proven to be important in this regard and will continue to be used to analyze new metal oxide electrodes as they are discovered. While metal oxides are commercially used for Li-ion batteries, a push to develop metal oxide battery electrodes for application in alternative ion batteries is of great interest. Low-toxicity battery components that are environmentally friendly and composed of earth abundant metals are ideal for future advancements in energy storage devices. Candidates include both alternative monovalent ion batteries such as $Na^+$ and $K^+$ as well as multivalent ion batteries such as $Zn^{2+}$ and $Ca^{2+}$. As metal oxides are investigated to be implemented in alternative ion batteries, EIS will prove to be a useful analytical technique to measure their performance capabilities for these relatively new and scarcely studied applications.

## *2.6 References*

1. Li, D.; Zhou, J.; Chen, X.; Song, H. Amorphous Fe2O3/Graphene Composite Nanosheets with Enhanced Electrochemical Performance for Sodium-Ion Battery. *ACS Appl. Mater. Interfaces* **2016**, *8* (45), 30899–30907.
2. Zhu, J.; Sharma, Y. K.; Zeng, Z.; Zhang, X.; Srinivasan, M.; Mhaisalkar, S.; Zhang, H.; Hng, H. H.; Yan, Q. Cobalt Oxide Nanowall Arrays on Reduced Graphene Oxide Sheets with Controlled Phase, Grain Size, and Porosity for Li-Ion Battery Electrodes. *J. Phys. Chem. C* **2011**, *115* (16), 8400–8406.
3. Wang, X.; Han, X.; Lim, M.; Singh, N.; Gan, C. L.; Jan, M.; Lee, P. S. Nickel Cobalt Oxide-Single Wall Carbon Nanotube Composite Material for Superior Cycling Stability and High-Performance Supercapacitor Application. *J. Phys. Chem. C* **2012**, *116* (23), 12448–12454.
4. Kwon, Y. H.; Minnici, K.; Huie, M. M.; Takeuchi, K. J.; Takeuchi, E. S.; Marschilok, A. C.; Reichmanis, E. Electron/Ion Transport Enhancer in High Capacity Li-Ion Battery Anodes. *Chem. Mater.* **2016**, *28* (18), 6689–6697.
5. Thangadurai, V.; Pinzaru, D.; Narayanan, S.; Baral, A. K. Fast Solid-State Li Ion Conducting Garnet-Type Structure Metal Oxides for Energy Storage. *J. Phys. Chem. Lett.* **2015**, *6* (2), 292–299.
6. Zhu, H.; Lee, K. T.; Hitz, G. T.; Han, X.; Li, Y.; Wan, J.; Lacey, S.; Cresce, A. von W.; Xu, K.; Wachsman, E.; Hu, L. Free-Standing Na2/3Fe1/2Mn1/2O2@Graphene Film for a Sodium-Ion Battery Cathode. *ACS Appl. Mater. Interfaces* **2014**, *6* (6), 4242–4247.
7. Bhaway, S. M.; Chen, Y.-M.; Guo, Y.; Tangvijitsakul, P.; Soucek, M. D.; Cakmak, M.; Zhu, Y.; Vogt, B. D. Hierarchical Electrospun and Cooperatively Assembled Nanoporous Ni/NiO/MnOx/Carbon Nanofiber Composites for Lithium Ion Battery Anodes. *ACS Appl. Mater. Interfaces* **2016**, *8* (30), 19484–19493.
8. Jeong, G. H.; Bae, H.-B.; Choi, D.; Kim, Y. H.; Yoon, S.; Kim, S.-W. Highly Stable Metal Mono-Oxide Alloy Nanoparticles and Their Potential as Anode Materials for Li-Ion Battery. *J. Phys. Chem. C* **2012**, *116* (45), 23851–23857.
9. Di Lecce, D.; Campanella, D.; Hassoun, J. Insight on the Enhanced Reversibility of a Multimetal Layered Oxide for Sodium-Ion Battery. *J. Phys. Chem. C* **2018**, *122* (42), 23925–23933.
10. Kumar Sen, U.; Shaligram, A.; Mitra, S. Intercalation Anode Material for Lithium Ion Battery Based on Molybdenum Dioxide. *ACS Appl. Mater. Interfaces* **2014**, *6* (16), 14311–14319.
11. Rock, S. E.; Wu, L.; Crain, D. J.; Krishnan, S.; Roy, D. Interfacial Characteristics of a PEGylated Imidazolium Bistriflamide Ionic Liquid Electrolyte at a Lithium Ion Battery Cathode of LiMn2O4. *ACS Appl. Mater. Interfaces* **2013**, *5* (6), 2075–2084.
12. Qian, D.; Xu, B.; Cho, H.-M.; Hatsukade, T.; Carroll, K. J.; Meng, Y. S. Lithium Lanthanum Titanium Oxides: A Fast Ionic Conductive Coating for Lithium-Ion Battery Cathodes. *Chem. Mater.* **2012**, *24* (14), 2744–2751.
13. Zhang, L.; Pu, J.; Jiang, Y.; Shen, Z.; Li, J.; Liu, J.; Ma, H.; Niu, J.; Zhang, H. Low Interface Energies Tune the Electrochemical Reversibility of Tin Oxide Composite Nanoframes as Lithium-Ion Battery Anodes. *ACS Appl. Mater. Interfaces* **2018**, *10* (43), 36892–36901.
14. Butala, M. M.; Danks, K. R.; Lumley, M. A.; Zhou, S.; Melot, B. C.; Seshadri, R. MnO Conversion in Li-Ion Batteries: In Situ Studies and the Role of Mesostructuring. *ACS Appl. Mater. Interfaces* **2016**, *8* (10), 6496–6503.

15. Bucher, N.; Hartung, S.; Franklin, J. B.; Wise, A. M.; Lim, L. Y.; Chen, H.-Y.; Weker, J. N.; Toney, M. F.; Srinivasan, M. P2–$Na_xCo_yMn_{1-y}O_2$ (y = 0, 0.1) as Cathode Materials in Sodium-Ion Batteries—Effects of Doping and Morphology To Enhance Cycling Stability. *Chem. Mater.* **2016**, *28* (7), 2041–2051.
16. Huang, H.; Feng, T.; Gan, Y.; Fang, M.; Xia, Y.; Liang, C.; Tao, X.; Zhang, W. TiC/NiO Core/Shell Nanoarchitecture with Battery-Capacitive Synchronous Lithium Storage for High-Performance Lithium-Ion Battery. *ACS Appl. Mater. Interfaces* **2015**, *7* (22), 11842–11848.
17. Sun, J.; Lv, C.; Lv, F.; Chen, S.; Li, D.; Guo, Z.; Han, W.; Yang, D.; Guo, S. Tuning the Shell Number of Multishelled Metal Oxide Hollow Fibers for Optimized Lithium-Ion Storage. *ACS Nano* **2017**, *11* (6), 6186–6193.
18. Smith, P. F.; Brady, A. B.; Lee, S.-Y.; Bruck, A. M.; Dooryhee, E.; Wu, L.; Zhu, Y.; Takeuchi, K. J.; Takeuchi, E. S.; Marschilok, A. C. Deliberately Designed Atomic-Level Silver-Containing Interface Results in Improved Rate Capability and Utilization of Silver Hollandite for Lithium-Ion Storage. *ACS Appl. Mater. Interfaces* **2018**, *10* (1), 400–407.
19. Bock, D. C.; Tappero, R. V.; Takeuchi, K. J.; Marschilok, A. C.; Takeuchi, E. S. Mapping the Anode Surface-Electrolyte Interphase: Investigating a Life Limiting Process of Lithium Primary Batteries. *ACS Appl. Mater. Interfaces* **2015**, *7* (9), 5429–5437.
20. Kim, S.; Cho, W.; Zhang, X.; Oshima, Y.; Choi, J. W. A Stable Lithium-Rich Surface Structure for Lithium-Rich Layered Cathode Materials. *Nat Commun* **2016**, *7* (1), 1–8.
21. Zhuang, Q.-C.; Wei, T.; Du, L.-L.; Cui, Y.-L.; Fang, L.; Sun, S.-G. An Electrochemical Impedance Spectroscopic Study of the Electronic and Ionic Transport Properties of Spinel $LiMn_2O_4$. *J. Phys. Chem. C* **2010**, *114* (18), 8614–8621.
22. Oh, G.; Hirayama, M.; Kwon, O.; Suzuki, K.; Kanno, R. Bulk-Type All Solid-State Batteries with 5 V Class $LiNi_{0.5}Mn_{1.5}O_4$ Cathode and $Li_{10}GeP_2S_{12}$ Solid Electrolyte. *Chem. Mater.* **2016**, *28* (8), 2634–2640.
23. Zhang, W.; Richter, F. H.; Culver, S. P.; Leichtweiss, T.; Lozano, J. G.; Dietrich, C.; Bruce, P. G.; Zeier, W. G.; Janek, J. Degradation Mechanisms at the $Li_{10}GeP_2S_{12}/LiCoO_2$ Cathode Interface in an All-Solid-State Lithium-Ion Battery. *ACS Appl. Mater. Interfaces* **2018**, *10* (26), 22226–22236.
24. Lou, S.; Shen, B.; Zuo, P.; Yin, G.; Yang, L.; Ma, Y.; Cheng, X.; Du, C.; Gao, Y. Electrochemical Performance Degeneration Mechanism of $LiCoO_2$ with High State of Charge during Long-Term Charge/Discharge Cycling. *RSC Adv.* **2015**, *5* (99), 81235–81242.
25. Osaka, T.; Mukoyama, D.; Nara, H. Review—Development of Diagnostic Process for Commercially Available Batteries, Especially Lithium Ion Battery, by Electrochemical Impedance Spectroscopy. *J. Electrochem. Soc.* **2015**, *162* (14), A2529–A2537.
26. Patil, S. B.; Kim, I. Y.; Gunjakar, J. L.; Oh, S. M.; Eom, T.; Kim, H.; Hwang, S.-J. Phase Tuning of Nanostructured Gallium Oxide via Hybridization with Reduced Graphene Oxide for Superior Anode Performance in Li-Ion Battery: An Experimental and Theoretical Study. *ACS Appl. Mater. Interfaces* **2015**, *7* (33), 18679–18688.
27. Medvedev, A. G.; Mikhaylov, A. A.; Grishanov, D. A.; Yu, D. Y. W.; Gun, J.; Sladkevich, S.; Lev, O.; Prikhodchenko, P. V. GeO2 Thin Film Deposition on Graphene Oxide by the Hydrogen Peroxide Route: Evaluation for Lithium-Ion Battery Anode. *ACS Appl. Mater. Interfaces* **2017**, *9* (10), 9152–9160.

28. Wang, Y.; Li, W.; Hu, G.; Peng, Z.; Cao, Y.; Gao, H.; Du, K.; Goodenough, J. B. Electrochemical Performance of Large-Grained $NaCrO_2$ Cathode Materials for Na-Ion Batteries Synthesized by Decomposition of $Na_2Cr_2O_7 \cdot 2H_2O$. *Chem. Mater.* **2019**, *31* (14), 5214–5223.
29. Zamani, N.; Modarresi-Alam, A. R.; Noroozifar, M. Synthesis and Application of Phosphorus/$Co_3O_4$–CuO Hybrid as High-Performance Anode Materials for Lithium-Ion Batteries. *ACS Omega* **2018**, *3* (4), 4620–4630.
30. Wang, Y.; Cao, L.; Huang, J.; Kou, L.; Li, J.; Wu, J.; Liu, Y.; Pan, L. Improved Li-Storage Properties of $Cu_2V_2O_7$ Microflower by Constructing an in Situ CuO Coating. *ACS Sustainable Chem. Eng.* **2019**, *7* (6), 6267–6274.
31. Xiang, J. Y.; Tu, J. P.; Qiao, Y. Q.; Wang, X. L.; Zhong, J.; Zhang, D.; Gu, C. D. Electrochemical Impedance Analysis of a Hierarchical CuO Electrode Composed of Self-Assembled Nanoplates. *J. Phys. Chem. C* **2011**, *115* (5), 2505–2513.
32. Rath, P. C.; Patra, J.; Saikia, D.; Mishra, M.; Tseng, C.-M.; Chang, J.-K.; Kao, H.-M. Comparative Study on the Morphology-Dependent Performance of Various CuO Nanostructures as Anode Materials for Sodium-Ion Batteries. *ACS Sustainable Chem. Eng.* **2018**, *6* (8), 10876–10885.
33. Liu, Y.; Wang, W.; Gu, L.; Wang, Y.; Ying, Y.; Mao, Y.; Sun, L.; Peng, X. Flexible CuO Nanosheets/Reduced-Graphene Oxide Composite Paper: Binder-Free Anode for High-Performance Lithium-Ion Batteries. *ACS Appl. Mater. Interfaces* **2013**, *5* (19), 9850–9855.
34. Venkatachalam, S.; Zhu, H.; Masarapu, C.; Hung, K.; Liu, Z.; Suenaga, K.; Wei, B. In-Situ Formation of Sandwiched Structures of Nanotube/$Cu_xO_y$/Cu Composites for Lithium Battery Applications. *ACS Nano* **2009**, *3* (8), 2177–2184.
35. Wang, C.; Li, Q.; Wang, F.; Xia, G.; Liu, R.; Li, D.; Li, N.; Spendelow, J. S.; Wu, G. Morphology-Dependent Performance of CuO Anodes via Facile and Controllable Synthesis for Lithium-Ion Batteries. *ACS Appl. Mater. Interfaces* **2014**, *6* (2), 1243–1250.
36. Klein, F.; Pinedo, R.; Berkes, B. B.; Janek, J.; Adelhelm, P. Kinetics and Degradation Processes of CuO as Conversion Electrode for Sodium-Ion Batteries: An Electrochemical Study Combined with Pressure Monitoring and DEMS. *J. Phys. Chem. C* **2017**, *121* (16), 8679–8691.
37. Lu, P.; Li, C.; Schneider, E. W.; Harris, S. J. Chemistry, Impedance, and Morphology Evolution in Solid Electrolyte Interphase Films during Formation in Lithium Ion Batteries. *J. Phys. Chem. C* **2014**, *118* (2), 896–903.
38. Huang, W.; Boyle, D. T.; Li, Y.; Li, Y.; Pei, A.; Chen, H.; Cui, Y. Nanostructural and Electrochemical Evolution of the Solid-Electrolyte Interphase on CuO Nanowires Revealed by Cryogenic-Electron Microscopy and Impedance Spectroscopy. *ACS Nano* **2019**, *13* (1), 737–744.
39. Ogihara, N.; Itou, Y.; Sasaki, T.; Takeuchi, Y. Impedance Spectroscopy Characterization of Porous Electrodes under Different Electrode Thickness Using a Symmetric Cell for High-Performance Lithium-Ion Batteries. *J. Phys. Chem. C* **2015**, *119* (9), 4612–4619.
40. Wu, S.; Lin, Y.; Xing, L.; Sun, G.; Zhou, H.; Xu, K.; Fan, W.; Yu, L.; Li, W. Stabilizing LiCoO2/Graphite at High Voltages with an Electrolyte Additive. *ACS Appl. Mater. Interfaces* **2019**, *11* (19), 17940–17951.
41. Thomas, M. G. S. R.; Bruce, P. G.; Goodenough, J. B. AC Impedance Analysis of Polycrystalline Insertion Electrodes: Application to $Li_{1-x}CoO_2$. *J. Electrochem. Soc.* **1985**, *132* (7), 1521–1528.

42. Huang, Y. F.; Ruan, W. H.; Lin, D. L.; Zhang, M. Q. Bridging Redox Species-Coated Graphene Oxide Sheets to Electrode for Extending Battery Life Using Nanocomposite Electrolyte. *ACS Appl. Mater. Interfaces* **2017**, *9* (1), 909–918.
43. Bojinov, M.; Geronov, Y.; Pistoia, G.; Pasquali, M. Impedance of the Li Electrode in Li/$Li_xMnO_2$ Accumulators at Open-Circuit Voltage. *J. Electrochem. Soc.* **1993**, *140* (2), 294–299.
44. Wu, M.-S.; Chang, H.-W. Self-Assembly of NiO-Coated ZnO Nanorod Electrodes with Core–Shell Nanostructures as Anode Materials for Rechargeable Lithium-Ion Batteries. *J. Phys. Chem. C* **2013**, *117* (6), 2590–2599.
45. Zhou, G.; Wang, D.-W.; Yin, L.-C.; Li, N.; Li, F.; Cheng, H.-M. Oxygen Bridges between NiO Nanosheets and Graphene for Improvement of Lithium Storage. *ACS Nano* **2012**, *6* (4), 3214–3223.
46. Park, J. R.; Macdonald, D. D. Impedance Studies of the Growth of Porous Magnetite Films on Carbon Steel in High Temperature Aqueous Systems. *Corros. Sci.* **1983**, *23* (4), 295–315.
47. MacDonald, D. D.; Pound, B. G.; Lenhart, S. J. The Application of Electrochemical Impedance Spectroscopy for Characterizing the Degradation of Ni(OH)2/NiOOH Electrodes. *J. Power Sources* **1990**, *29* (3), 477–502.
48. Justin, P.; Meher, S. K.; Rao, G. R. Tuning of Capacitance Behavior of NiO Using Anionic, Cationic, and Nonionic Surfactants by Hydrothermal Synthesis. *J. Phys. Chem. C* **2010**, *114* (11), 5203–5210.
49. Wang, L.; Cao, X.; Xu, L.; Chen, J.; Zheng, J. Transformed Akhtenskite $MnO_2$ from $Mn_3O_4$ as Cathode for a Rechargeable Aqueous Zinc Ion Battery. *ACS Sustainable Chem. Eng.* **2018**, *6* (12), 16055–16063.
50. Han, S.-D.; Kim, S.; Li, D.; Petkov, V.; Yoo, H. D.; Phillips, P. J.; Wang, H.; Kim, J. J.; More, K. L.; Key, B.; Klie, R. F.; Cabana, J.; Stamenkovic, V. R.; Fister, T. T.; Markovic, N. M.; Burrell, A. K.; Tepavcevic, S.; Vaughey, J. T. Mechanism of Zn Insertion into Nanostructured δ-$MnO_2$: A Nonaqueous Rechargeable Zn Metal Battery. *Chem. Mater.* **2017**, *29* (11), 4874–4884.
51. Wang, H.; Mao, N.; Shi, J.; Wang, Q.; Yu, W.; Wang, X. Cobalt Oxide-Carbon Nanosheet Nanoarchitecture as an Anode for High-Performance Lithium-Ion Battery. *ACS Appl. Mater. Interfaces* **2015**, *7* (4), 2882–2890.
52. Laman, F. C. Impedance Studies for Separators in Rechargeable Lithium Batteries. *J. Electrochem. Soc.* **1993**, *140* (4), L51–L53.
53. Chen, M.; Chen, D.; Liao, Y.; Zhong, X.; Li, W.; Zhang, Y. Layered Lithium-Rich Oxide Nanoparticles Doped with Spinel Phase: Acidic Sucrose-Assistant Synthesis and Excellent Performance as Cathode of Lithium Ion Battery. *ACS Appl. Mater. Interfaces* **2016**, *8* (7), 4575–4584.
54. Chen, K.; Xue, D. Room-Temperature Chemical Transformation Route to CuO Nanowires toward High-Performance Electrode Materials. *J. Phys. Chem. C* **2013**, *117* (44), 22576–22583.
55. Verrelli, R.; Scrosati, B.; Sun, Y.-K.; Hassoun, J. Stable, High Voltage $Li_{0.85}Ni_{0.46}Cu_{0.1}Mn_{1.49}O_4$ Spinel Cathode in a Lithium-Ion Battery Using a Conversion-Type CuO Anode. *ACS Appl. Mater. Interfaces* **2014**, *6* (7), 5206–5211.

56. Zhao, K.; Sun, C.; Yu, Y.; Dong, Y.; Zhang, C.; Wang, C.; Voyles, P. M.; Mai, L.; Wang, X. Surface Gradient Ti-Doped $MnO_2$ Nanowires for High-Rate and Long-Life Lithium Battery. *ACS Appl. Mater. Interfaces* **2018**, *10* (51), 44376–44384.
57. Huang, G.; Yin, D.; Zhang, F.; Li, Q.; Wang, L. Yolk@Shell or Concave Cubic NiO–$Co_3O_4$@C Nanocomposites Derived from Metal–Organic Frameworks for Advanced Lithium-Ion Battery Anodes. *Inorg. Chem.* **2017**, *56* (16), 9794–9801.
58. Huang, J.; Poyraz, A. S.; Lee, S.-Y.; Wu, L.; Zhu, Y.; Marschilok, A. C.; Takeuchi, K. J.; Takeuchi, E. S. Silver-Containing α-$MnO_2$ Nanorods: Electrochemistry in Na-Based Battery Systems. *ACS Appl. Mater. Interfaces* **2017**, *9* (5), 4333–4342.
59. Wang, K.; Zhang, X.; Han, J.; Zhang, X.; Sun, X.; Li, C.; Liu, W.; Li, Q.; Ma, Y. High-Performance Cable-Type Flexible Rechargeable Zn Battery Based on $MnO_2$@CNT Fiber Microelectrode. *ACS Appl. Mater. Interfaces* **2018**, *10* (29), 24573–24582.
60. Wang, Z.; Mo, F.; Ma, L.; Yang, Q.; Liang, G.; Liu, Z.; Li, H.; Li, N.; Zhang, H.; Zhi, C. Highly Compressible Cross-Linked Polyacrylamide Hydrogel-Enabled Compressible Zn–$MnO_2$ Battery and a Flexible Battery–Sensor System. *ACS Appl. Mater. Interfaces* **2018**, *10* (51), 44527–44534.
61. Sun, W.; Wang, F.; Hou, S.; Yang, C.; Fan, X.; Ma, Z.; Gao, T.; Han, F.; Hu, R.; Zhu, M.; Wang, C. Zn/$MnO_2$ Battery Chemistry With $H^+$ and $Zn^{2+}$ Coinsertion. *J. Am. Chem. Soc.* **2017**, *139* (29), 9775–9778.
62. Goodenough, J. B.; Park, K.-S. The Li-Ion Rechargeable Battery: A Perspective. *J. Am. Chem. Soc.* **2013**, *135* (4), 1167–1176.
63. Reddy, M. V.; Subba Rao, G. V.; Chowdari, B. V. R. Metal Oxides and Oxysalts as Anode Materials for Li Ion Batteries. *Chem. Rev.* **2013**, *113* (7), 5364–5457.
64. Nakayama, M.; Taki, H.; Nakamura, T.; Tokuda, S.; Jalem, R.; Kasuga, T. Combined Computational and Experimental Study of Li Exchange Reaction at the Surface of Spinel $LiMn_2O_4$ as a Rechargeable Li-Ion Battery Cathode. *J. Phys. Chem. C* **2014**, *118* (47), 27245–27251.
65. Dedryvère, R.; Foix, D.; Franger, S.; Patoux, S.; Daniel, L.; Gonbeau, D. Electrode/Electrolyte Interface Reactivity in High-Voltage Spinel $LiMn_{1.6}Ni_{0.4}O_4/Li_4Ti_5O_{12}$ Lithium-Ion Battery. *J. Phys. Chem. C* **2010**, *114* (24), 10999–11008.
66. Jiang, Q.; Liu, D.; Zhang, H.; Wang, S. Plasma-Assisted Sulfur Doping of $LiMn_2O_4$ for High-Performance Lithium-Ion Batteries. *J. Phys. Chem. C* **2015**, *119* (52), 28776–28782.
67. Lu, D.; Li, W.; Zuo, X.; Yuan, Z.; Huang, Q. Study on Electrode Kinetics of $Li^+$ Insertion in $Li_xMn_2O_4$ ($0 \leq x \leq 1$) by Electrochemical Impedance Spectroscopy. *J. Phys. Chem. C* **2007**, *111* (32), 12067–12074.
68. Aurbach, D. Review of Selected Electrode–Solution Interactions Which Determine the Performance of Li and Li Ion Batteries. *J. Power Sources* **2000**, *89* (2), 206–218.
69. Mizushima, K.; Jones, P. C.; Wiseman, P. J.; Goodenough, J. B. $Li_xCoO_2$ ($0<x<-1$): A New Cathode Material for Batteries of High Energy Density. *Mate Res Bull* **1980**, *15* (6), 783–789.
70. Johnston, W. D.; Heikes, R. R.; Sestrich, D. The Preparation, Crystallography, and Magnetic Properties of the $Li_xCo_{(1-x)}O$ System. *J. Phys. Chem. Solids* **1958**, *7* (1), 1–13.
71. Sauvage, F.; Tarascon, J.-M.; Baudrin, E. In Situ Measurements of Li Ion Battery Electrode Material Conductivity: Application to $Li_xCoO_2$ and Conversion Reactions. *J. Phys. Chem. C* **2007**, *111* (26), 9624–9630.

72. Lu, W.; Zhang, J.; Xu, J.; Wu, X.; Chen, L. In Situ Visualized Cathode Electrolyte Interphase on $LiCoO_2$ in High Voltage Cycling. *ACS Appl. Mater. Interfaces* **2017**, *9* (22), 19313–19318.
73. Tan, H.; Takeuchi, S.; Bharathi, K. K.; Takeuchi, I.; Bendersky, L. A. Microscopy Study of Structural Evolution in Epitaxial $LiCoO_2$ Positive Electrode Films during Electrochemical Cycling. *ACS Appl. Mater. Interfaces* **2016**, *8* (10), 6727–6735.
74. Harilal, M.; G. Krishnan, S.; Pal, B.; Reddy, M. V.; Ab Rahim, M. H.; Yusoff, M. M.; Jose, R. Environment-Modulated Crystallization of $Cu_2O$ and CuO Nanowires by Electrospinning and Their Charge Storage Properties. *Langmuir* **2018**, *34* (5), 1873–1882.
75. Liu, H.; Li, W.; Shen, D.; Zhao, D.; Wang, G. Graphitic Carbon Conformal Coating of Mesoporous $TiO_2$ Hollow Spheres for High-Performance Lithium Ion Battery Anodes. *J. Am. Chem. Soc.* **2015**, *137* (40), 13161–13166.
76. Zhang, L.; Gu, X.; Yan, C.; Zhang, S.; Li, L.; Jin, Y.; Zhao, S.; Wang, H.; Zhao, X. Titanosilicate Derived $SiO_2/TiO_2$@C Nanosheets with Highly Distributed $TiO_2$ Nanoparticles in $SiO_2$ Matrix as Robust Lithium Ion Battery Anode. *ACS Appl. Mater. Interfaces* **2018**, *10* (51), 44463–44471.
77. Wang, Y.-Q.; Gu, L.; Guo, Y.-G.; Li, H.; He, X.-Q.; Tsukimoto, S.; Ikuhara, Y.; Wan, L.-J. Rutile-$TiO_2$ Nanocoating for a High-Rate $Li_4Ti_5O_{12}$ Anode of a Lithium-Ion Battery. *J. Am. Chem. Soc.* **2012**, *134* (18), 7874–7879.
78. Qiu, J.; Zhang, P.; Ling, M.; Li, S.; Liu, P.; Zhao, H.; Zhang, S. Photocatalytic Synthesis of $TiO_2$ and Reduced Graphene Oxide Nanocomposite for Lithium Ion Battery. *ACS Appl. Mater. Interfaces* **2012**, *4* (7), 3636–3642.
79. Sundaramurthy, J.; Aravindan, V.; Suresh Kumar, P.; Madhavi, S.; Ramakrishna, S. Electrospun $TiO_2{-}\delta$ Nanofibers as Insertion Anode for Li-Ion Battery Applications. *J. Phys. Chem. C* **2014**, *118* (30), 16776–16781.
80. Zheng, J.; Liu, L.; Ji, G.; Yang, Q.; Zheng, L.; Zhang, J. Hydrogenated Anatase $TiO_2$ as Lithium-Ion Battery Anode: Size–Reactivity Correlation. *ACS Appl. Mater. Interfaces* **2016**, *8* (31), 20074–20081.
81. Salman, M. S.; Park, A. R.; Cha, M. J.; Choi, Y.; Jang, S. K.; Tan, L.; Yoo, P. J.; Choe, W.-S. Lysozyme-Templated Meso-Macroporous Hollow $TiO_2$ for Lithium Ion Battery Anode. *ACS Appl. Nano Mater.* **2018**, *1* (2), 698–710.
82. Balogun, M.-S.; Zhu, Y.; Qiu, W.; Luo, Y.; Huang, Y.; Liang, C.; Lu, X.; Tong, Y. Chemically Lithiated $TiO_2$ Heterostructured Nanosheet Anode with Excellent Rate Capability and Long Cycle Life for High-Performance Lithium-Ion Batteries. *ACS Appl. Mater. Interfaces* **2015**, *7* (46), 25991–26003.
83. Ha, J. U.; Lee, J.; Abbas, M. A.; Lee, M. D.; Lee, J.; Bang, J. H. Designing Hierarchical Assembly of Carbon-Coated $TiO_2$ Nanocrystals and Unraveling the Role of $TiO_2$/Carbon Interface in Lithium-Ion Storage in $TiO_2$. *ACS Appl. Mater. Interfaces* **2019**, *11* (12), 11391–11402.
84. Liu, D.; Yu, Q.; Liu, S.; Qian, K.; Wang, S.; Sun, W.; Yang, X.-Q.; Kang, F.; Li, B. Evolution of Solid Electrolyte Interface on $TiO_2$ Electrodes in an Aqueous Li-Ion Battery Studied Using Scanning Electrochemical Microscopy. *J. Phys. Chem. C* **2019**, *123* (20), 12797–12806.
85. Ren, W.; Zhou, W.; Zhang, H.; Cheng, C. ALD TiO2-Coated Flower-like $MoS_2$ Nanosheets on Carbon Cloth as Sodium Ion Battery Anode with Enhanced Cycling Stability and Rate Capability. *ACS Appl. Mater. Interfaces* **2017**, *9* (1), 487–495.

86. Deng, J.; Wang, X.; Duan, X.; Liu, P. Facile Preparation of $MnO_2$/Graphene Nanocomposites with Spent Battery Powder for Electrochemical Energy Storage. *ACS Sustainable Chem. Eng.* **2015**, *3* (7), 1330–1338.
87. Rashad, M.; Li, X.; Zhang, H. Magnesium/Lithium-Ion Hybrid Battery with High Reversibility by Employing $NaV_3O_8 \cdot 1.69H_2O$ Nanobelts as a Positive Electrode. *ACS Appl. Mater. Interfaces* **2018**, *10* (25), 21313–21320.
88. Wang, L.; Asheim, K.; Vullum, P. E.; Svensson, A. M.; Vullum-Bruer, F. Sponge-Like Porous Manganese(II,III) Oxide as a Highly Efficient Cathode Material for Rechargeable Magnesium Ion Batteries. *Chem. Mater.* **2016**, *28* (18), 6459–6470.
89. Truong, Q. D.; Kempaiah Devaraju, M.; Tran, P. D.; Gambe, Y.; Nayuki, K.; Sasaki, Y.; Honma, I. Unravelling the Surface Structure of $MgMn_2O_4$ Cathode Materials for Rechargeable Magnesium-Ion Battery. *Chem. Mater.* **2017**, *29* (15), 6245–6251.

# Chapter 3

# Defining the Role of $Cr^{3+}$ as a Reductant in the Hydrothermal Synthesis of $CuCrO_2$ Delafossite

*This chapter was reproduced from the following publication:

Chown, Amanda L.; Farnum, Byron H. *Inorg. Chem.* **2022**, 61 (21), 8349-8355

## *3.1 Introduction*

Transparent oxide semiconductors (TOSs), named for both their semiconducting properties and their transparency to visible light due to having a wide band gap, are often used in heterojunction solar cells as charge transport layers. $TiO_2$, $SnO_2$, and ZnO are primary examples of n-type TOSs which have been used as electron transport layers in dye-sensitized solar cells, quantum dot solar cells, organic photovoltaics, and perovskite solar cells.[132–137] Examples of p-type TOSs include NiO and the family of $CuMO_2$ delafossites, of which $CuCrO_2$ has been applied as a hole transport layer in various solar cells in addition to solar fuel devices such as dye-sensitized photoelectrosynthesis cells.[23,138]

Previous studies have pointed to inferior performance for p-type TOSs in comparison to their n-type counterparts, exhibiting short hole diffusion lengths which impede charge extraction.[26,27] It has been proposed that this is due to electronic defects which result in poor charge separation at the metal oxide interface. Specifically, the proclivity of such defects and byproducts in $CuCrO_2$ synthesis has been linked to the synthetic method, as recently reported by Zhao et al.[28] Understanding these defects thus requires synthetic control of the desired material; however, the synthetic methods used to make delafossite $CuCrO_2$ have been cumbersome. Previous studies required temperatures above 500° C and high pressure environments, commonly leading to the phase transition into spinel $CuCr_2O_4$.[139,140] Poeppelmeier developed a hydrothermal synthetic method with $Cu_2O$ and $Cr(OH)_3$ precursors to make $CuCrO_2$ under relatively low temperature conditions, albeit with long reaction times and large particle sizes.[141] In contrast, the hydrothermal synthesis of *nanocrystalline* delafossite materials is typically achieved with metal salt precursors such as $Cu(NO_3)_2$ and $Cr(NO_3)_3$.[142–144] These routes can be prone to result in cuprite ($Cu_2O$) and/or tenorite (CuO) side products during the reaction. This has been proposed to result from a gradient in temperature between the walls of the Teflon cup and the solution at the center of the Parr bomb, introducing different thermodynamic environments which may favor byproduct formation.[142]

One aspect of the hydrothermal synthesis from metal salts that has not been addressed is the role of $Cr^{3+}$ as a reductant in the conversion of $Cu^{2+}$ to $Cu^{+}$. Although $Cu^{+}$ is the desired oxidation state for $CuCrO_2$, $Cu^{+}$ is unstable in aqueous solution at room temperature, and thus $Cu^{2+}$ precursors must be used when starting with metal salts. Ethylene glycol has been used as a reductant for the synthesis of $CuGaO_2$ where $Ga^{3+}$ is redox inert. Likewise, synthesis of $CuFeO_2$ has been achieved with either ethylene glycol or $Fe^{2+}$ as the reductant. Despite the obvious need for a reductant, published synthetic procedures for $CuCrO_2$ from metal salt precursors have not included a secondary reductant or discussed the redox activity of $Cr^{3+}$ such that no stoichiometric reaction has been established for the overall synthesis. Given the challenges of competitive binary oxide formation present in the ternary $CuCrO_2$ synthesis in addition to the possible consumption of $Cr^{3+}$ due to redox activity, understanding the optimized stoichiometry for Cr:Cu is an important parameter for achieving pure phase $CuCrO_2$.

Here, we report on the hydrothermal synthesis and optimization of $CuCrO_2$ in an effort to produce nanocrystalline material in the absence of unwanted byproducts. By optimizing the synthetic conditions for the growth of $CuCrO_2$, photo/electrochemical studies may be more reproducible and the material may be better understood fundamentally for further applications. Here we show that the ratio of starting materials, in addition to the production of chromate, clearly has an influence on byproduct formation, where a 4:3 ratio of $Cr^{3+}$ and $Cu^{2+}$ nitrate salts is optimal for hydrothermal synthesis of $CuCrO_2$.

## *3.2 Experimental Section*

### *3.2.1 Synthesis of $CuCrO_2$ Nanocrystals*

Hydrothermal synthesis of delafossite $CuCrO_2$ nanocrystals was conducted according to a preparation method previously reported in the literature.[141,145] Chromium nitrate nonahydrate [$Cr(NO_3)_3 \cdot 9\ H_2O$] (Alfa Aesar, 98.5%) and copper nitrate hemipentahydrate [$Cu(NO_3)_2 \cdot 2.5\ H_2O$] (Alfa Aesar, 98%+) were added to 70 mL deionized $H_2O$ (18MΩ cm, Milli-Q) and stirred in an ice bath. The molar ratio of chromium to copper precursors (Cr:Cu) was varied to generate two series of reaction conditions. Series 1 contained Cr:Cu ratios from 0.5 – 10 in which the total metal concentration was held constant at [Cr] + [Cu] = 0.5 M. Series 2 contained Cr:Cu ratios from 0.5 – 2 in which [Cu] = 0.21 M was fixed. After addition of the precursors to cold water, a minimum of 7.03 g KOH (VWR Analytical) was added and a final targeted $pH > 13$ was recorded to ensure basicity of the solution and visual confirmation of metal hydroxide formation in solution.

The mixture was then stirred and transferred equally to three 45 mL Teflon cups and sealed in acid digestion bombs (Parr). The bombs were placed in a box furnace (Lindberg Blue M) and heated to 240 ˚C for 12 – 60 hours, depending on the procedure. The bombs were removed from the furnace and the reaction mixtures were centrifuged to separate the solid products, which were combined to form a single solid product. This solid was analyzed for structural characterization prior to being suspended in 0.5 M $NH_4OH$ (28 vol %, BDH) solution for 24 hours. Following this step, any dissolved solid was rinsed with ethanol, sonicated in ethanol, and vortexed for 3 cycles to remove impurities and to clean the product. The remaining product was allowed to dry in ethanol under a fume hood before the final drying step in a vacuum oven (Lindberg Blue M) at 60 ˚C.

### *3.2.2 Analysis of $CrO_4^{2-}$*

In order to study the role of $Cr^{3+}$ as a reducing agent, the chromate produced from each reaction was quantified spectrophotometrically. Standard, tech-grade $Na_2Cr_2O_7$ was added to a basic solution with a pH ≥ 13 containing KOH in Millipore $H_2O$ to prepare standard chromate solutions at known concentrations. At pH 13, $Cr_2O_7^{2-}$ dissociates completely to form two equivalents of $CrO_4^{2-}$.[146] The extinction coefficient of the absorbance peak for $CrO_4^{2-}$ at 372 nm was then quantified using UV-visible absorbance spectroscopy. The pH of post synthesis solutions were found to be in excess of 13, ensuring $CrO_4^{2-}$ quantification. An Agilent Cary 8454 UV-Vis spectrophotometer was used to study both the standard and experimental concentrations of chromate ions in solution.

### *3.2.3 Structural Characterization*

Powder X-ray diffraction (pXRD) data was collected using a Rigaku SmartLab X-Ray diffractometer with a Cu Kα source in a Bragg-Brentano geometry. XRD data were processed using SmartLab Studio II software. Scanning electron microscopy (SEM) images were collected using a Hitachi S-4700. Transmission electron microscopy (TEM) images were collected using a Thermo Scientific Talos F200X with EDS. Inductively coupled plasma mass spectrometry (ICP-MS) was collected using an Agilent 7900 Quadrupole ICP-MS system with a high temperature

(>6000°K) plasma source. All samples were dissolved in trace metal-free concentrated nitric acid by means of hydrothermal acid digestion in Teflon Parr bombs at 200 ˚C for 5 hours. A serial dilution was performed using a trace metal-free 2% nitric acid solution to acquire an ICP-ready solution with a targeted sample concentration between 0 and 200 ppb.

## *3.3 Results and Discussion*

### *3.3.1 Time Dependent Synthesis*

A 1:1 ratio of Cr:Cu starting material has been commonly used in the literature to produce delafossite $CuCrO_2$. However, the time required to undergo the condensation reaction of the precursors, as seen in **Figure 3.1**, is unclear. While some previously report 60 hour reactions[141,147], others have reported producing $CuCrO_2$ under shorter reaction times.[28,148] Before further synthetic optimization, we explored the time dependence of the reaction using the hydrothermal synthetic route to determine if allowing the synthesis to proceed for a longer period of time improves the overall quality of the product.

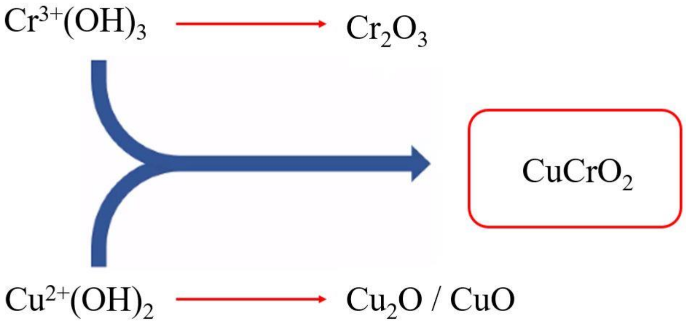

**Figure 3.1.** Illustration of the general condensation reaction producing the delafossite metal oxide $CuCrO_2$ with competitive formation of binary oxides $Cu_2O$, CuO, and $Cr_2O_3$.

As seen in **Figure 3.2**, a series of reactions were conducted where the ratio of Cr:Cu starting materials was fixed at 1:1 with 0.5 M total starting materials (i.e. 0.25 M each), and the reaction time was varied from 12, 24, 36, 48, and 60 hours. Under the 12 hour synthesis condition, it is apparent that three distinct peaks at 35.5º, 38.8˚, and 48.8˚ are present. These peaks are specific to the diffraction pattern for CuO (tenorite; PDF #00-041-0254). A broad shoulder peak near 37º was also evident and could be assigned to either $Cu_2O$ or $CuCrO_2$. Diffractograms were found to be unchanged from 12-48 hrs; however, as the reaction time increased to 60 hours, the peaks associated with CuO decreased in intensity and the predominant peaks in the diffractogram were found to be 31.0˚, 36.2˚, and 61.7˚, characteristic of the (006), (012), and (110) peaks, respectively for delafossite $CuCrO_2$ (PDF #00-039-0247). Notably, even at 60 hrs, residual peaks for CuO were still observed at 38.8˚ and 48.8˚. This could suggest that CuO is a precursor to $CuCrO_2$ formation or that $Cu^{2+}$ is insufficiently reduced to $Cu^{+}$. Based on these results the synthetic time was fixed at 60 hrs for all subsequent experiments to allow for optimal formation of $CuCrO_2$.

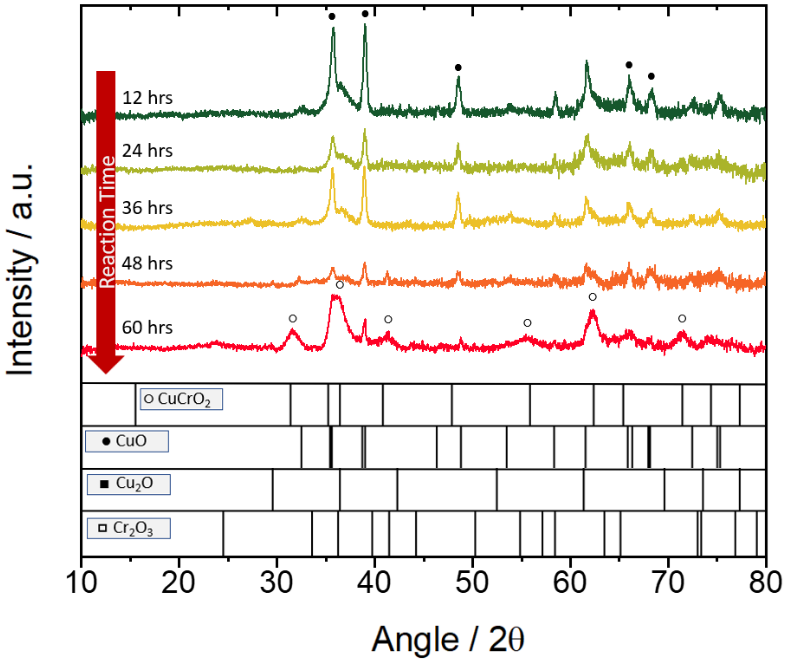

**Figure 3.2.** pXRD diffractograms obtained from unwashed solid products resulting from a 1:1 Cr:Cu ratio with various reaction times from 12 to 60 hrs. Standard diffraction patterns for CuO (PDF 00-041-0254), $Cu_2O$ (PDF 00-005-0667), $Cr_2O_3$ (PDF 00-038-1479), and $CuCrO_2$ (PDF 00-039-0247) are shown for comparison.

### *3.3.2 Series 1: 0.5 M Fixed Concentration of Reactants*

To investigate the role of $Cr^{3+}$ as a reductant, metal oxide powders were synthesized using a constant total concentration of metal [Cr] + [Cu] = 0.5 M while the moles of $Cu(NO_3)_2$ and $Cr(NO_3)_3$ were adjusted in order to vary the ratio of Cr:Cu from 0.50 to 2.00. XRD data for the unwashed solids are shown in **Figure 3.3a**. Reaction parameters for the series can be found in **Table S3.1** for additional clarity. Control experiments with only 0.5 M $Cu(NO_3)_2$ or $Cr(NO_3)_3$ are also shown for reference in **Figure S3.1**. Clear changes in the diffractograms were observed as a function of Cr:Cu ratio with Cr:Cu = 0.50 and 0.67 showing sharp, pronounced peaks for CuO (35.5˚, 38.8˚, and 48.8˚) and much smaller, broad peaks for $CuCrO_2$ (31.0˚, 36.2˚, and 61.7˚). The broad peaks of $CuCrO_2$ indicate nanocrystalline particle sizes. Under the condition where only $Cu(NO_3)_2$ was present (Cr:Cu = 0.00), CuO was the only observed product. When looking at Cr:Cu = 1.00, 1.15, and 1.33 diffractograms, it is evident that the broad peaks assigned to $CuCrO_2$ became dominant while those for CuO were greatly diminished, being undetectable for Cr:Cu = 1.33. At the highest Cr:Cu = 2.00, CuO could not be detected by pXRD.

To determine the limit of detection of CuO, pXRD data was collected for varying mixtures of NaCl and CuO standards, as seen in **Figure S3.2**. It is evident that even at 1 wt. % CuO, peaks identified as CuO were present in the powder mixtures. Therefore, an absence of CuO peaks can be assigned to <1% impurity.

Additionally, peaks associated with $Cu_2O$ and $Cr_2O_3$ were present in **Figure 3.2a**. Washing the solid product with 0.5 M $NH_4OH$ for 24 hrs resulted in the removal of peaks assigned to $Cu_2O$ and $Cr_2O_3$, however, CuO peaks were persistent (**Figure 3.3b**). The base washing reactions corresponding to the removal of $Cu_2O$ and $Cr_2O_3$ from the final solid product are shown in **Equations 3.1-3.2**. These results show that $CuCrO_2$ of high purity could be synthesized using a Cr:Cu ratio greater than 1.33 coupled with a secondary washing step in $NH_4OH$. These results also suggest that many literature procedures which utilize a 1:1 Cr:Cu ratio may have CuO impurities.

$$Cu_2O + 4NH_4OH \rightarrow 2[Cu(NH_3)_2]OH + 3H_2O \qquad \textbf{eq. 3.1)}$$

$$Cr_2O_3 + 6NH_4OH \rightarrow 2Cr(OH)_3 + 3(NH_4)_2O \qquad \textbf{eq. 3.2)}$$

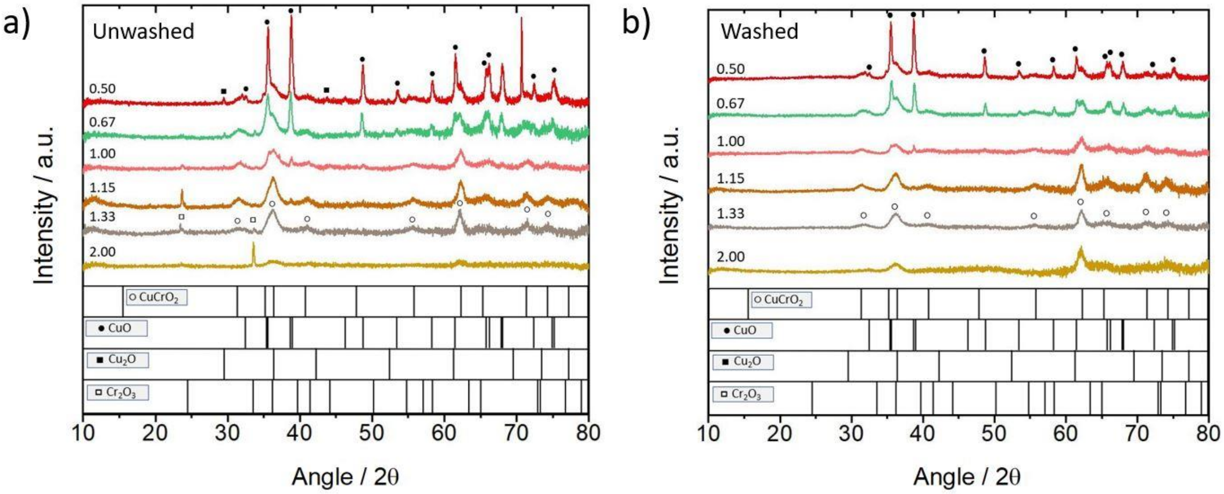

**Figure 3.3.** Powder diffractograms obtained for solid products for the indicated Cr:Cu ratios with a reaction time of 60 hrs. In all cases, the [Cr] + [Cu] = 0.5 M. Peaks from $CuCrO_2$ are identified using (o) and peaks from CuO are identified using (●). Noteworthy peaks from $Cu_2O$ and $Cr_2O_3$ are denoted using (▪) and (▫), respectively. **a)** unwashed samples. **b)** samples after being washed in 0.5 M $NH_4OH$ solution for 24 hrs.

The product formation as a function of Cr:Cu ratio strongly suggests that $Cr^{3+}$ acts as a reductant for conversion of $Cu^{2+}$ to $Cu^{+}$. In the absence of $Cr^{3+}$ or with a Cr:Cu ratio $< 1.00$, CuO was predominately formed, whereas with higher ratios, the $Cu^{+}$ containing $CuCrO_2$ was the dominant product. A proposed redox reaction for the overall formation of $CuCrO_2$ is shown in **Equation 3.2** where one $Cr^{3+}$ is able to reduce three equivalents of $Cu^{2+}$ to $Cu^{+}$, resulting in a balanced stoichiometry of 4:3 Cr:Cu (1.33). In further support of this, calculated Pourbaix diagrams reported by Beverskog show that reduction of $Cu^{2+}$ by $Cr^{3+}$ is thermodynamically favorable at elevated temperatures with $\Delta G = -0.33$ eV at 200 ˚C (see SI for further details).[149,150] **Equation 3.2** was confirmed by the presence of $CrO_4^{2-}$ as the oxidized product, as determined by UV-visible absorbance spectra collected for the post-synthesis reaction liquid (**Figure 3.4a**). The concentration of $CrO_4^{2-}$ produced for each Cr:Cu ratio was then calculated using the extinction coefficient of the absorbance feature at 372 nm, measured to be 4,835 $M^{-1}$ $cm^{-1}$ (**Figure S3.3**) and consistent with other literature reports.[151–153]

$4\ Cr^{3+} + 3\ Cu^{2+} + 20\ OH^- \rightarrow 3\ CuCrO_2 + CrO_4^{2-} + 10\ H_2O$ **eq. 3.2)**

$2\ Cr^{3+} + 6\ Cu^{2+} + 22\ OH^- \rightarrow 3\ Cu_2O + 2\ CrO_4^{2-} + 11\ H_2O$ **eq. 3.3)**

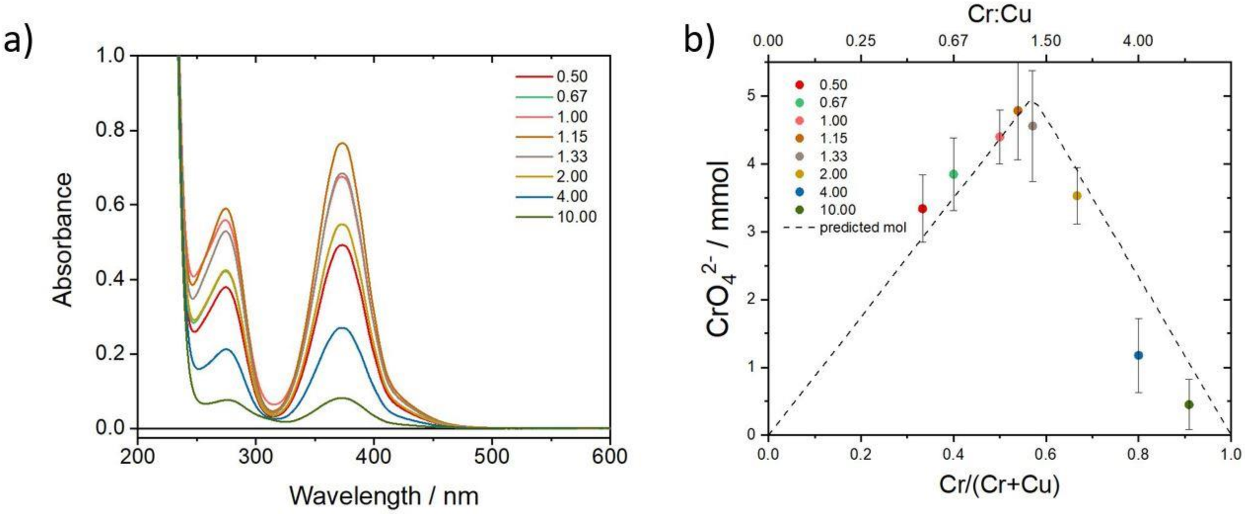

**Figure 3.4. a)** UV-visible absorbance spectra of post-reaction solutions produced from different ratios of Cr:Cu with a total [Cr] + [Cu] = 0.5 M. The absorbance spectra are consistent with $CrO_4^{2-}$. **b)** Millimoles of $CrO_4^{2-}$ measured from absorbance data plotted versus mole fraction of Cr and Cr:Cu ratio. Dashed line shows the theoretical amount of $CrO_4^{2-}$ produced based on **Equation 3.2**.

**Figure 3.4b** shows the concentration of chromate ions produced as a function of mole fraction of Cr ($\chi_{Cr}$ = Cr/(Cr + Cu)) and Cr:Cu ratio. It is evident that the largest amount of chromate produced is near the optimal ratio of 1.33 for Cr:Cu reactants ($\chi_{Cr}$ = 0.57). Error bars are provided and represent the standard deviation calculated from three separate reactions. The increase in

$CrO_4^{2-}$ up to 1.33 Cr:Cu followed by a decrease at higher ratios is due to the constant total metal concentration used for this series of reactions. At low Cr:Cu ratios, the amount of $CrO_4^{2-}$ produced is limited by the amount of $Cr^{3+}$ present during the reaction and the efficiency of reduction. At high Cr:Cu ratios, $CrO_4^{2-}$ production is limited by the amount of $Cu^{2+}$ available. The dashed line shown in **Figure 3.4b** represents the theoretical amount of $CrO_4^{2-}$ produced for 100% efficiency of **Equation 3.2**.

The experimental data follows the expected trend with additional data points at Cr:Cu ratios of 4.00 and 10.00 continuing to show the linear decline in $CrO_4^{2-}$ with Cr:Cu and $\chi_{Cr}$; however, the experimental data deviates from the theoretical line at ratios both lower and higher than 1.33. These deviations are a reflection of the percent yield for $CrO_4^{2-}$ (**Table S3.3**) and were found to greater than expected for Cr:Cu < 1.33 and lower than expected for Cr:Cu > 1.33. For Cr:Cu < 1.33, we believe that competitive formation of $Cu_2O$ via reduction of $Cu^{2+}$ by $Cr^{3+}$ is responsible for the greater than 100% yield of $CrO_4^{2-}$. The balanced redox reaction for the $Cu_2O$ formation is shown in **Equation 3.3** where the yield of $CrO_4^{2-}$ per $Cr^{3+}$ is 100% compared with 25% for $CuCrO_2$ formation. A small fraction of $Cu_2O$ side reactivity could therefore produce a greater than expected yield for $CrO_4^{2-}$. For Cr:Cu > 1.33, we believe the decline in percent yield is due to competitive $Cr_2O_3$ formation as more $Cr^{3+}$ is introduced to the reaction. In addition, the decreased percent yields at higher Cr:Cu ratios indicates a lower efficiency for $Cr^{3+}$ reduction of $Cu^{2+}$ which is supported by the persistent nature of CuO found via pXRD at higher ratios.

### *3.3.3 Series 2: 15 mmol Fixed Concentration of $Cu^{II}$ Reactant*

To further confirm the $Cr^{3+}$ reductant mechanism, a second series of reactions was conducted where the ratio of Cr:Cu was varied from 0.50 to 2.00; however, the $Cu(NO_3)_2$ starting material was fixed at 0.21 M (i.e. 15 mmol), allowing both the amount of $Cr(NO_3)_3$ and the amount of total metal concentration to change. Reaction parameters for the series can be found in **Table S3.2**. Powder XRD data showed similar trends as the first series, with high amounts of CuO at low Cr:Cu ratios, optimal production of $CuCrO_2$ at 1.33 Cr:Cu and an increase in $Cr_2O_3$ at high Cr:Cu ratios (**Figure 3.5**).

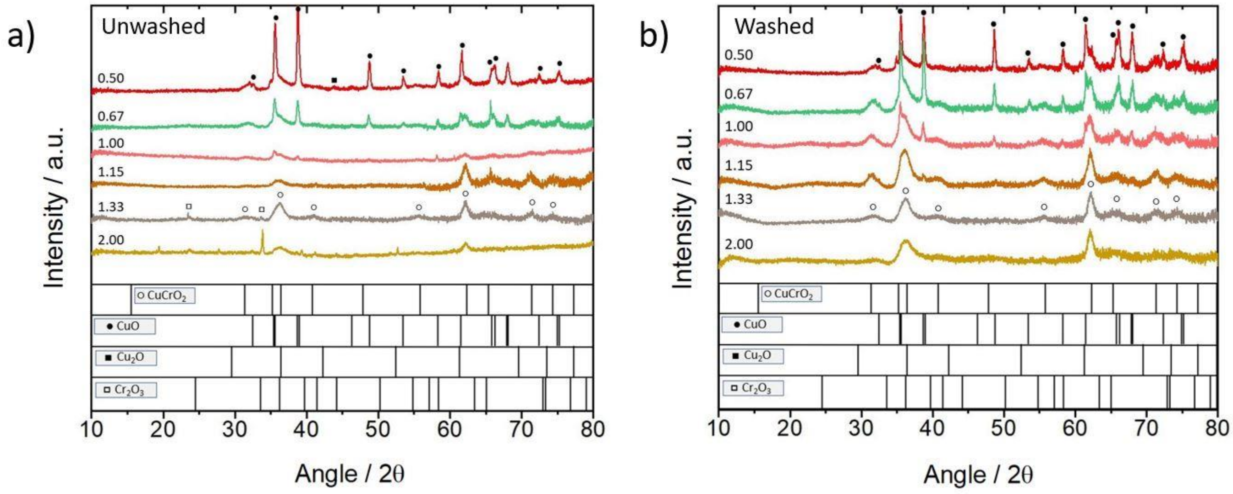

**Figure 3.5.** Powder diffractograms obtained for solid products from the indicated Cr:Cu ratios. In all cases, the total $[Cu^{2+}]$ = 0.21 M (i.e. 15 mmol). Peaks from $CuCrO_2$ are identified using (o) and peaks from CuO are identified using (●). Noteworthy peaks from $Cu_2O$ and $Cr_2O_3$ are denoted using (▫) and (▪). **a)** unwashed solids. **b)** solids after being washed in 0.5 M $NH_4OH$ solution for 24 hours.

The amount of $CrO_4^{2-}$ produced experimentally for the second series followed the predicted theoretical trend (**Figure 3.6**) where production was limited at low Cr:Cu ratios by the amount of $Cr^{3+}$ in solution and reached a plateau beyond a ratio of 1.33 due to the constant amount of $Cu^{2+}$. Notably, reactions containing Cr:Cu ratios of 4.00 and 10.00 were not conducted with this series because the amount of $Cr^{3+}$ reactant needed to run the reaction became impractical beyond a 2.00 ratio. Similar to the first series, the percent yield was also found to be greater than 100% at low Cr:Cu ratios and decrease as the ratio increased. **Figure S3.4** shows an overlay of $CrO_4^{2-}$ percent yields for both series of reactions where both show a similar decline as Cr:Cu increased. Also consistent was the fact that low Cr:Cu ratios resulted in $CrO_4^{2-}$ percent yields in excess of 100%, likely due to $Cu_2O$ formation according to **Equation 3.3**.

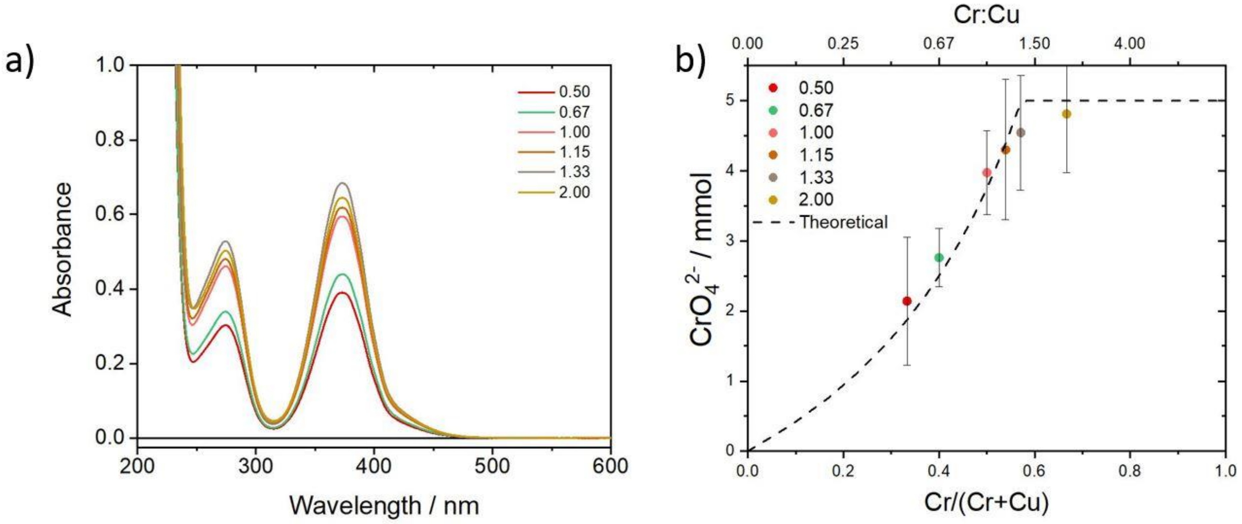

**Figure 3.6. a)** UV-visible absorbance spectra of post-reaction solutions produced from reactions where [Cu] = 0.21 M. **b)** Millimoles of $CrO_4^{2-}$ in solution for each reaction calculated from absorbance data and plotted versus mole fraction of Cr and Cr:Cu ratio. The dashed line represents the theoretical amount of $CrO_4^{2-}$ based on **Equation 3.2**.

Microscopy studies were conducted on samples from each series to analyze the morphological characteristics of each product. SEM images collected for series 1 reactions after base washing are shown in **Figure 3.7**. **Figure S3.5** shows SEM data for series 2 reactions. Across all reaction conditions, small particles were produced with anisotropic, plate-like morphology appearing for ratios of 1.00 and 1.33. The plate-like morphology is characteristic of $CuCrO_2$ nanocrystals based on the layered delafossite unit cell. At Cr:Cu = 0.50, more isotropic particles with smooth faces are observed. This could be due to the CuO formation under conditions where an excess amount of $Cu^{2+}$ starting material was used. Indeed, when only $Cu^{2+}$ was present in the reaction, the CuO produced exhibited an isotropic morphology, albeit with large particle sizes (**Figure S3.6**). In the reaction with only $Cr^{3+}$, small amorphous particles were produced.

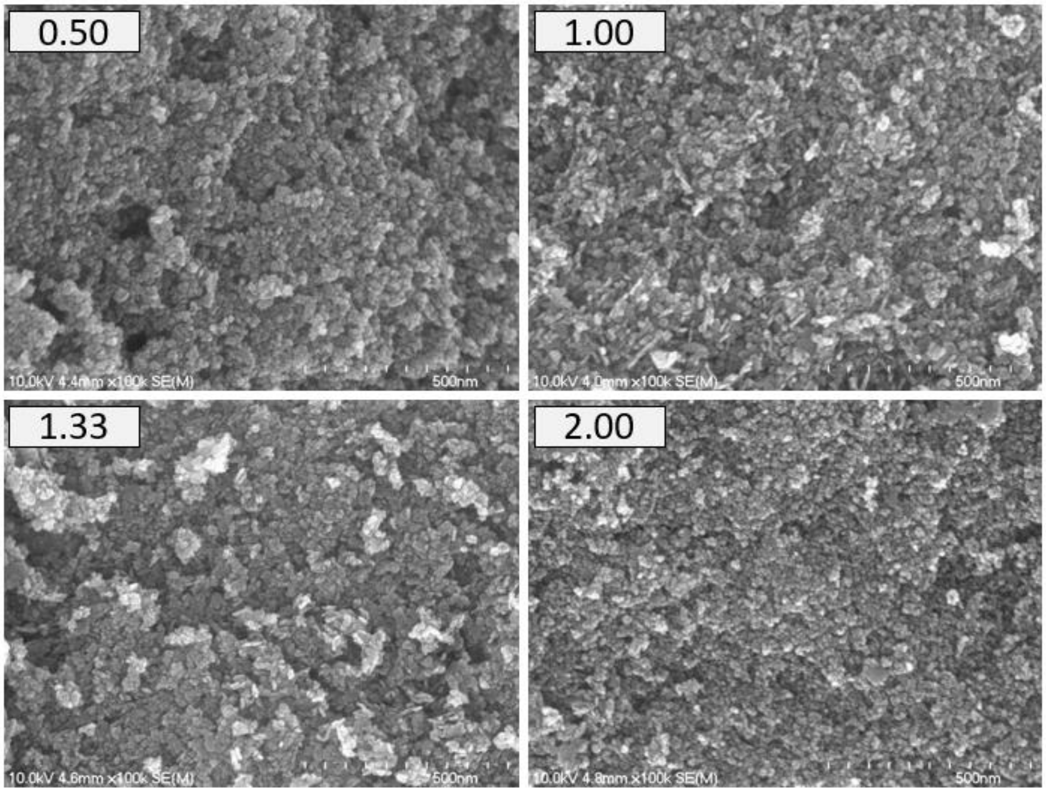

**Figure 3.7.** SEM images at constant magnification of products with Cr:Cu ratios 0.50, 1.00, 1.33, and 2.00 from the series with [Cr] + [Cu] = 0.5 M. All samples have been washed in 0.1 M $NH_4OH$ solution for 24 hours.

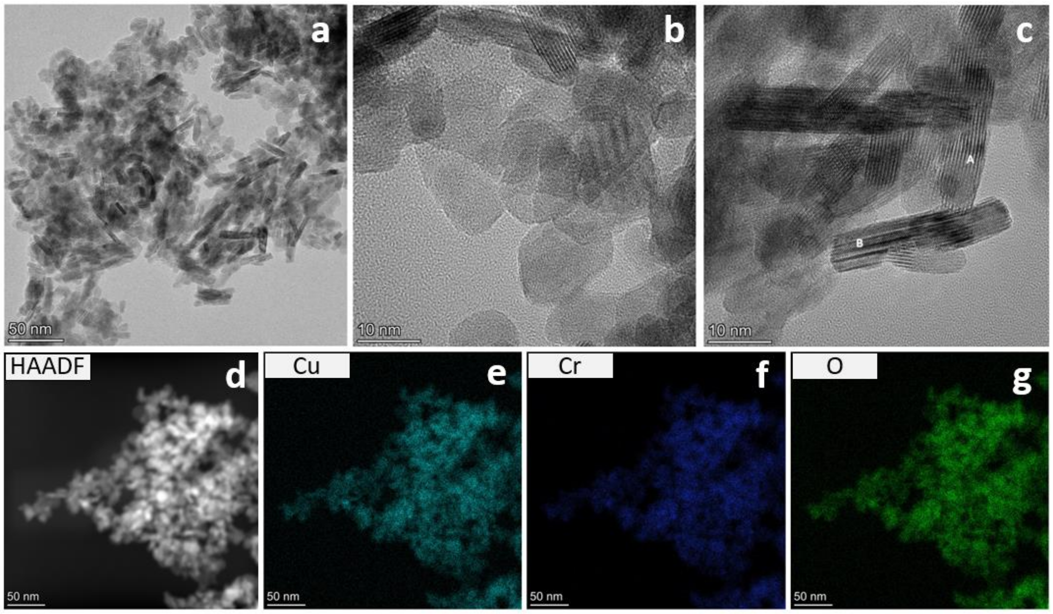

**Figure 3.8. a-c)** TEM images of washed solid product obtained from a Cr:Cu ratio of 1.33 with [Cu] + [Cr] = 0.5 M. **d-g)** HAADF images and EDS mapping of the same material.

TEM and EDS studies were further conducted on the optimized Cr:Cu ratio of 1.33 with images shown in **Figure 3.8**. Nanocrystals appear as anisotropic plates with an aspect ratio of 4.6 ± 1.9. High magnification indicates lattice fringes labeled as A and B in **Figure 3.8c**, typical of other reports for TEM images of $CuCrO_2$ nanocrystals.[22,154] High Angle Annular Dark Field (HAADF) images and EDS mapping reveals an even distribution of copper, chromium, and oxygen atoms throughout the nanocrystals.

ICP-MS was conducted for each sample in both series to determine elemental composition. A summary of this data is shown in **Table 3.1** for the unwashed and base washed products. The measured Cr:Cu ratio for unwashed samples was found to be an average of 73 ± 7 % of the starting ratio across all reaction conditions, meaning that ~27% of the starting precursors do not get converted to solid product. The low ratios for solid product obtained from low starting ratios is consistent with the presence of CuO byproducts found via pXRD, resulting from a lack of $Cu^{2+}$

reduction at low concentrations of $Cr^{3+}$. As Cr:Cu increased beyond the optimal ratio of 1.33, the final ratio also increased, likely due to formation of $Cr_2O_3$ byproducts or other amorphous materials not detectable by XRD in excess of $CuCrO_2$. Washing the solid products resulted in a general increase in the final Cr:Cu ratio, likely due to removal of $Cu_2O$.

**Table 3.1.** Ratio of Cr:Cu measured by ICP-MS for solid products.

| | [Cu] + [Cr] = 0.5 M | | [Cu] = 0.21 M | |
|---|---|---|---|---|
| Starting Ratio | unwashed | washed | unwashed | washed |
| 0.50 | 0.365 ± 0.004 | 0.402 ± 0.005 | 0.311 ± 0.004 | 0.325 ± 0.003 |
| 0.67 | 0.505 ± 0.006 | 0.511 ± 0.014 | 0.579 ± 0.008 | 0.547 ± 0.009 |
| 1.00 | 0.647 ± 0.006 | 0.766 ± 0.014 | 0.743 ± 0.027 | 0.753 ± 0.009 |
| 1.15 | 0.885 ± 0.022 | 0.889 ± 0.014 | 0.749 ± 0.012 | 0.843 ± 0.016 |
| 1.33 | 0.940 ± 0.059 | 1.036 ± 0.015 | 0.940 ± 0.059 | 1.036 ± 0.015 |
| 2.00 | 1.523 ± 0.006 | 1.685 ± 0.033 | 1.625 ± 0.019 | 1.680 ± 0.033 |

Based on the pXRD and ICP analysis, the optimal ratio of Cr:Cu to form $CuCrO_2$ with minimal impurities is 1.33 (4:3). At this ratio, an excess of Cu is present in the unwashed sample which is likely attributed to the presence of $Cu_2O$ impurity. After base washing the product, the ratio increased due to removal of $Cu_2O$ (*i.e.*, 27% mass loss during washing step; **Table S3.4**) and resulted in a final Cr:Cu ratio of 1.04, indicating a slight excess of Cr. Based on pXRD, this solid product is expected to be free from CuO impurities and thus the excess Cr could be attributed to $Cu^+$ vacancies in the $CuCrO_2$ lattice. This means that ~4% of $Cu^+$ sites could be vacant. Previous studies on $CuGaO_2$ have also indicated $Cu^+$ vacancies at similar defect percentages.[37]

### *3.3.4 Introducing Ethylene Glycol as a Reductant*

The role of $Cr^{3+}$ as a reductant is clearly established by the data presented thus far; however, the complexities of the competitive reactions beg the question of whether an alternative reductant could be used to generate $Cu^+$ while keeping $Cr^{3+}$ redox stable. Other reported synthetic routes for copper delafossite materials have used ethylene glycol as a reductant with much success.[155–157] For comparative purposes, ethylene glycol was thus added to the reaction with a 1:1 ratio of Cr:Cu precursors, as an excess of Cr should not be needed. Analysis of the solid product by pXRD (**Figure 3.9**), however, revealed that $CuCrO_2$ was not formed, but rather Cu metal (PDF#00-004-0836) was the major product along with an unknown product, possibly derived from Cr. These results indicate that addition of secondary reductants is not likely to result in a more efficient synthesis of $CuCrO_2$ and that a solid understanding of the $Cr^{3+}$ reductant and competitive side reactions is required to produce $CuCrO_2$ nanocrystals of high purity.

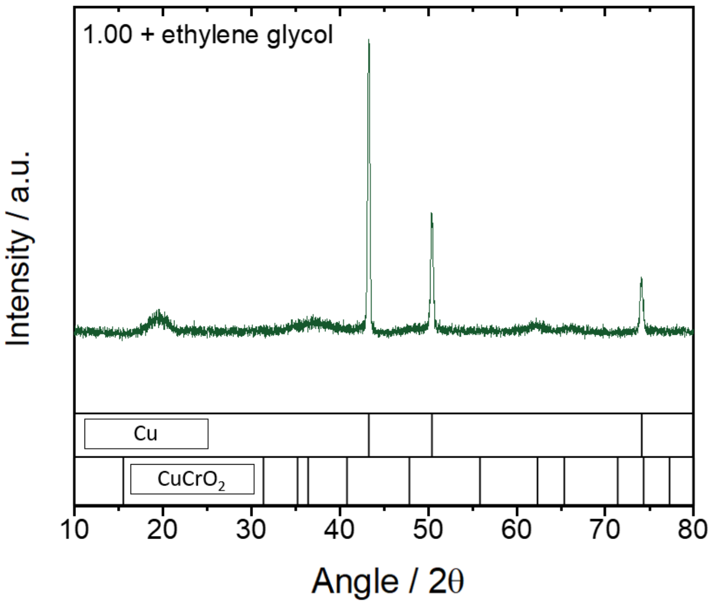

**Figure 3.9.** Diffractogram for solid product obtained from hydrothermal synthesis of a 1:1 ratio of Cr:Cu for 60 hours with ethylene glycol added as a reductant.

### *3.4 Conclusion*

The role of $Cr^{3+}$ as a reductant in the hydrothermal synthesis of $CuCrO_2$ from $Cu^{2+}$ and $Cr^{3+}$ precursors has been clearly elucidated by detection of $CrO_4^{2-}$ in the post-synthesis reaction solution. The results point to an optimized Cr:Cu ratio of 4:3 based on the reaction stoichiometry established in **Equation 3.2**. Deviation from this ratio leads to the formation of byproducts such as $Cu_2O$, CuO, and $Cr_2O_3$. The narrow window for which $CuCrO_2$ can be synthesized with high purity emphasizes the fact that impurities and defects could influence optical or electrochemical properties of $CuCrO_2$ if synthetic parameters are not optimized. Future studies are currently underway to understand how these impurities and defects specifically impact electrochemical properties and the band gap of $CuCrO_2$.

### *3.5 Supporting Information*

**Table S3.1**. Summary of reaction parameters for series 1 in which the total concentration of reactants was fixed at 0.5 M

| [Cu] + [Cr] = 0.5 M | | | | |
|---|---|---|---|---|
| Starting Ratio Cr:Cu | $Cu^{2+}$ reactant (mmol) | $Cr^{3+}$ reactant (mmol) | $H_2O$ added (mL) | Reaction time (hours) |
| 0.50 | 23.33 | 11.67 | 70 | 60 |
| 0.67 | 21 | 14 | 70 | 60 |
| 1.00 | 17.5 | 17.5 | 70 | 60 |
| 1.15 | 16.5 | 18.86 | 70 | 60 |
| 1.33 | 15 | 20 | 70 | 60 |
| 2.00 | 11.67 | 23.33 | 70 | 60 |
| 4.00 | 7 | 28 | 70 | 60 |
| 10.00 | 3.18 | 31.82 | 70 | 60 |

**Table S3.2**. Summary of reaction parameters for series 2 in which the starting [Cu] was fixed at 0.21 M

| [Cu] = 0.21 M | | | | |
|---|---|---|---|---|
| Starting Ratio Cr:Cu | $Cu^{2+}$ reactant (mmol) | $Cr^{3+}$ reactant (mmol) | $H_2O$ added (mL) | Reaction time (hours) |
| 0.50 | 15 | 7.5 | 70 | 60 |
| 0.67 | 15 | 10 | 70 | 60 |
| 1.00 | 15 | 15 | 70 | 60 |
| 1.15 | 15 | 16.67 | 70 | 60 |
| 1.33 | 15 | 20 | 70 | 60 |
| 2.00 | 15 | 30 | 70 | 60 |

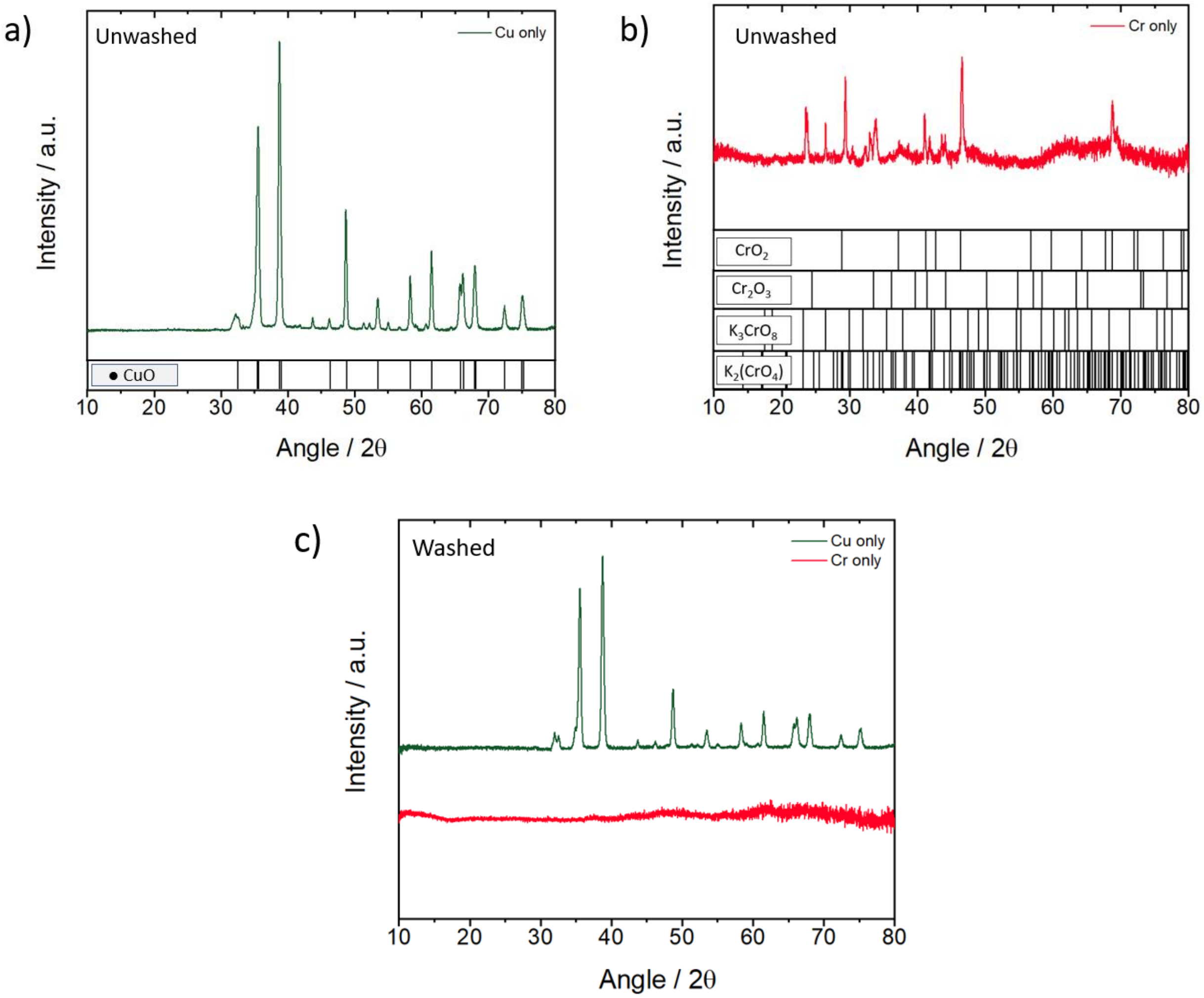

**Figure S3.1. a)** pXRD of unwashed products produced in which either 0.5 M $Cu^{2+}(NO_3)_2$ or 0.5 M $Cr^{3+}(NO_3)_3$ reactant are present in the reaction. **b)** The unwashed product in which 0.5 M $Cr^{3+}(NO_3)_3$ magnified alongside standards for comparison: $CrO_2$ (PDF # 01-075-7968), $Cr_2O_3$ (PDF # 00-038-1479), $K_3CrO_8$ (PDF # 00-014-0652), and $K_2(CrO_4)$ (PDF # 01-070-1222). **c)** pXRD of products after washing in 0.5 M $NH_4OH$ for 24 hours and dried prior to collecting the XRD.

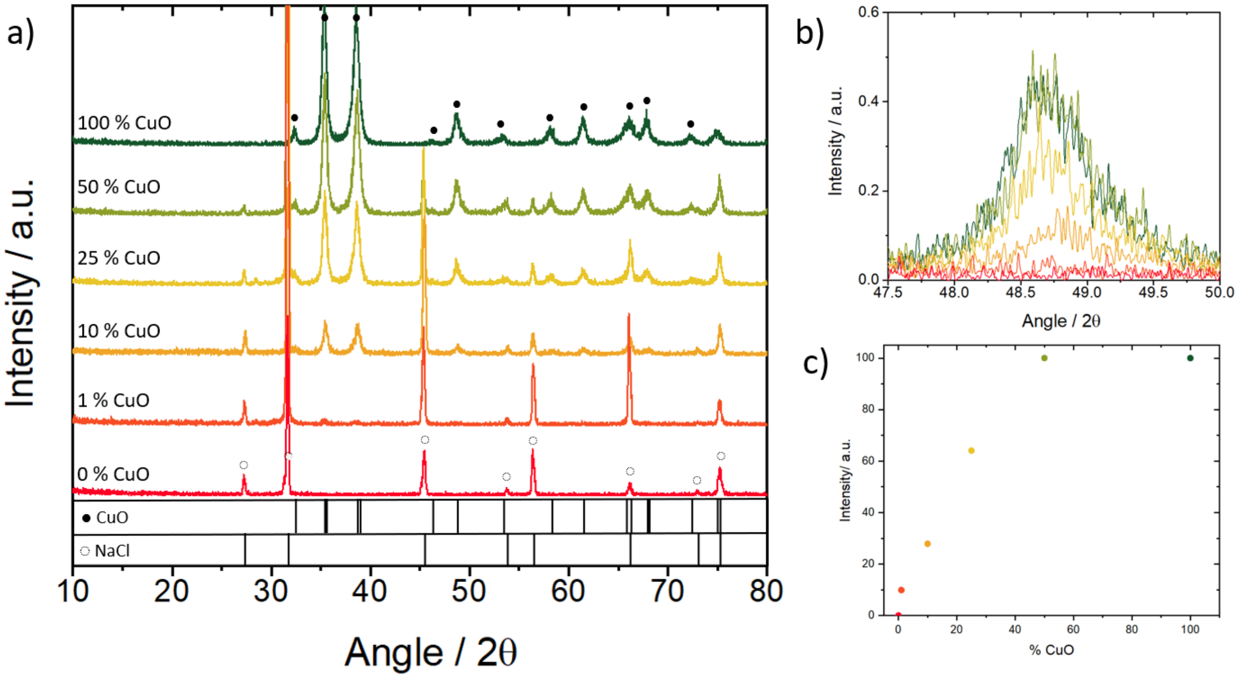

**Figure S3.2. a)** pXRD of CuO (Alfa Aesar, 30-50 nm APS powder) and NaCl (VWR Chemicals, crystalline) mixtures where CuO is represented as weight percentages in the sample. Peaks are identified as CuO (PDF # 00-041-0254) and NaCl (PDF # 00-005-0628). **b)** pXRD of CuO:NaCl mixtures zoomed in at 48.9˚. **c)** Plot of relative intensities as a function of CuO:NaCl mixtures at the 48.9˚ peak.

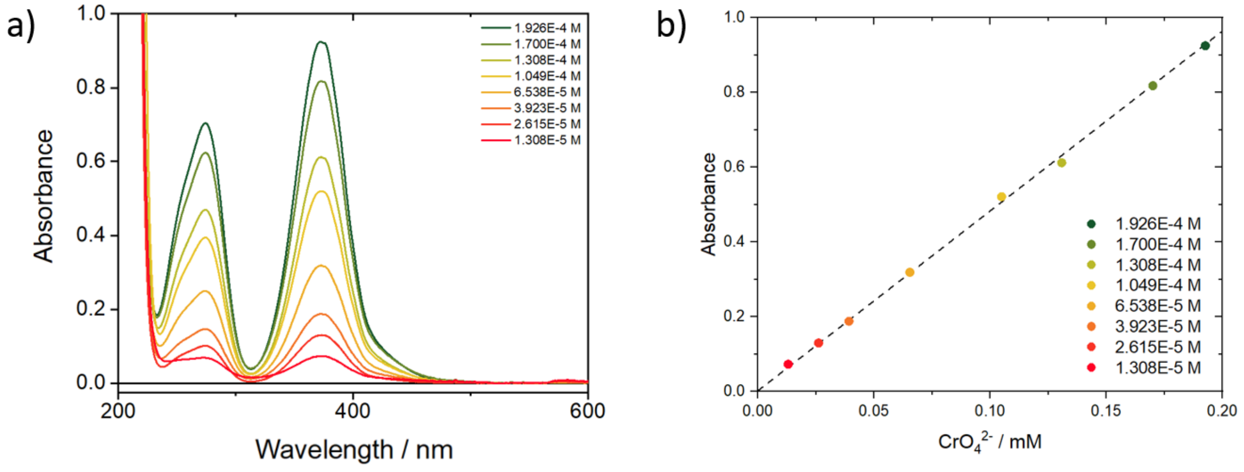

**Figure S3.3. a)** UV-visible absorbance spectra collected for [$CrO_4^{2-}$] in aqueous solution at standard concentrations and pH > 13. **b)** Beer-Lambert plot constructed from absorbance values at 372 nm. The extinction coefficient was calculated to be 4,835 $M^{-1}$ $cm^{-1}$.

**Table S3.3.** Summary of experimental yields of $CrO_4^{2-}$ obtained from UV-visible absorbance data for post-synthesis reaction liquids

| | [Cu] + [Cr] = 0.5 M | | | [Cu] = 0.21 M | | |
|---|---|---|---|---|---|---|
| Starting Ratio | Experimental Yield (mmol) | Theoretical Yield (mmol) | % Yield | Experimental Yield (mmol) | Theoretical Yield (mmol) | % Yield |
| 0.50 | 3.34 ± 0.50 | 2.90 | 115.2 ± 9.9 | 2.14 ± 0.91 | 1.87 | 114.4 ± 20.3 |
| 0.67 | 3.85 ± 0.54 | 3.53 | 109.1 ± 12.5 | 2.76 ± 0.42 | 2.52 | 109.5 ± 10.3 |
| 1.00 | 4.40 ± 0.40 | 4.37 | 100.7 ± 20.9 | 3.97 ± 0.60 | 3.77 | 105.3 ± 10.8 |
| 1.15 | 4.79 ± 0.72 | 4.70 | 101.9 ± 10.9 | 4.30 ± 1.01 | 4.32 | 99.5 ± 19.8 |
| 1.33 | 4.56 ± 0.82 | 4.92 | 92.7 ± 13.6 | 4.54 ± 0.82 | 4.93 | 80.5 ± 13.6 |
| 2.00 | 3.53 ± 0.42 | 3.90 | 90.5 ± 4.6 | 4.81 ± 0.84 | 5.00 | 96.2 ± 15.2 |
| 4.00 | 1.18 ± 0.54 | 2.33 | 50.6 ± 11.5 | | | |
| 10.00 | 0.45 ± 0.37 | 1.06 | 42.9 ± 7.5 | | | |

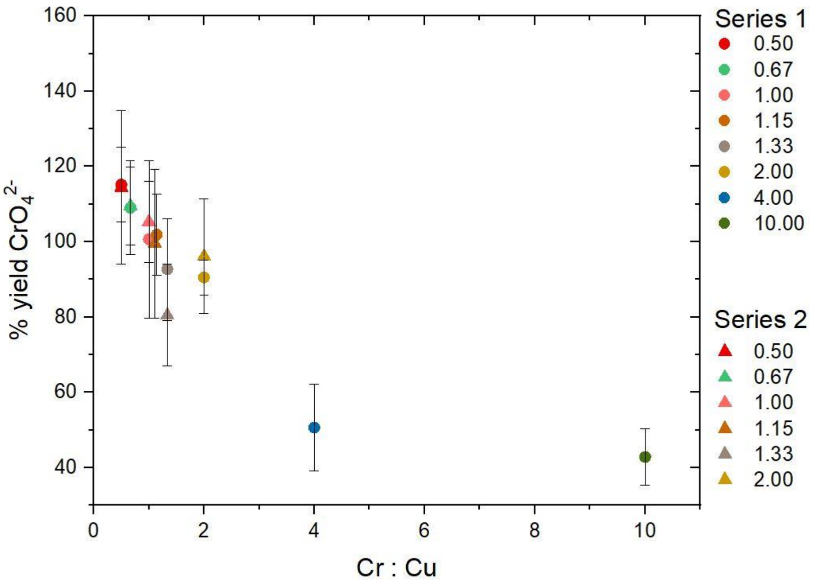

**Figure S3.4.** Percent yields for $CrO_4^{2-}$ plotted versus Cr:Cu ratio for both series of reactions. Legend indicates Cr:Cu ratio. Series 1 represents [Cr] + [Cu] = 0.5 M and Series 2 represents [Cu] = 0.21 M.

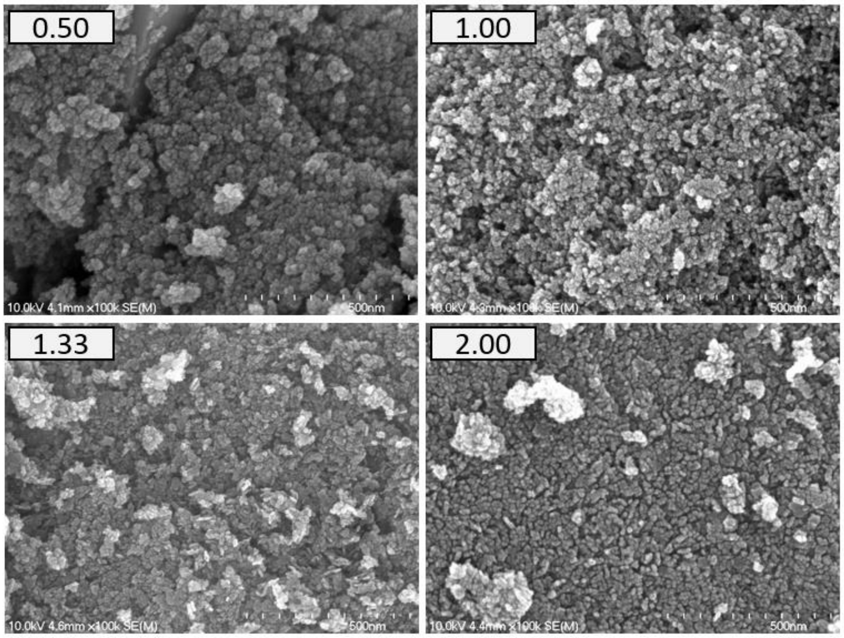

**Figure S3.5.** SEM images for washed 0.50, 1.00, 1.33, and 2.00 Cr:Cu ratios from series where [$Cu^{2+}$] reactant = 0.21 M.

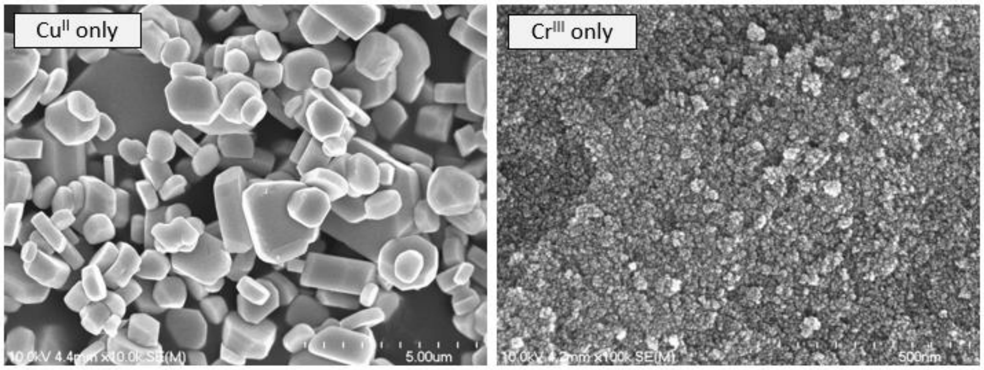

**Figure S3.6.** SEM images at varying magnifications of the products from the control reactions containing only $Cu^{2+}$ or $Cr^{3+}$ starting materials. All samples which have been washed in 0.1 M $NH_4OH$ solution for 24 hours.

**Table S3.4.** Summary of washed yields of $CuCrO_2$ powders and percent recovery

| | [Cu] + [Cr] = 0.5 M | | | [Cu] = 0.21 M | | |
|---|---|---|---|---|---|---|
| Starting Ratio | Unwashed Mass (g) | Washed Mass (g) | % Recovery | Unwashed Mass (g) | Washed Mass (g) | % Recovery |
| 0.50 | 0.1537 | 0.1287 | 83.73 | 0.1345 | 0.1013 | 75.32 |
| 0.67 | 0.1342 | 0.1031 | 76.83 | 0.1760 | 0.1288 | 73.18 |
| 1.00 | 0.1319 | 0.0937 | 71.04 | 0.3612 | 0.2794 | 77.35 |
| 1.15 | 0.1878 | 0.1359 | 72.36 | 0.1154 | 0.0805 | 69.76 |
| 1.33 | 0.1498 | 0.1099 | 73.36 | 0.1498 | 0.1099 | 73.36 |
| 2.00 | 0.1707 | 0.1266 | 74.17 | 0.2344 | 0.1766 | 75.34 |
| 4.00 | 0.1589 | 0.1175 | 73.95 | | | |
| 10.00 | 0.1363 | 0.1022 | 74.98 | | | |

## Thermodynamics of $Cr^{3+}$ reduction of $Cu^{2+}$ at elevated temperatures

Beverskog has published calculated Pourbaix diagrams for the copper and chromium redox systems at elevated temperatures.[22,23] Under basic conditions, $Cu(OH)_4^{2-}$ and $Cr(OH)_4^-$ are the proposed dominant species for $Cu^{2+}$ and $Cr^{3+}$. Note that the speciation of the chromite ion is unconfirmed in the cited publication and is assumed to be $Cr(OH)_4^-$. The following redox reactions and their corresponding potentials were extracted from the Pourbaix diagrams to the best of our ability.

$CrO_4^{2-} + 4H_2O + 3e^- \rightarrow Cr(OH)_4^- + 4OH^-$ $E \sim -0.75$ V vs SHE

$Cu(OH)_4^{2-} + e^- \rightarrow Cu(OH)_2^- + 2OH^-$ $E \sim -0.64$ V vs SHE

Overall balanced reaction:

$Cr(OH)_4^- + 3Cu(OH)_4^{2-} \rightarrow CrO_4^{2-} + 3Cu(OH)_2^- + 4H_2O + 2OH^-$ $\Delta E = +0.11$ V

$\Delta G = -0.33$ eV

### *3.6 References*

1. Samadpour, M.; Boix, P.P.; Giménez, S.; Zad, A.I.; Taghavinia, N.; Mora-Seró, I.; Bisquert, J. Fluorine Treatment of $TiO_2$ for Enhancing Quantum Dot Sensitized Solar Cell Performance. *J. Phys. Chem. C* **2011**, 115 (29), 14400-14407.
2. Boix, P. P.; Larramona, G.; Jacob, A.; Delatouche, B.; Mora-Seró, I.; Bisquert, J. Hole Transport and Recombination in All-Solid $Sb_2S_3$-Sensitized $TiO_2$ Solar Cells Using CuSCN As Hole Transporter. *J. Phys. Chem. C* **2012**, 116 (1), 1579–1587.
3. Dembele, K. T.; Selopal, G. S.; Soldano, C.; Nechache, R.; Rimada, J. C.; Concina, I.; Sberveglieri, G.; Rosei, F.; Vomiero, A. Hybrid Carbon Nanotubes–$TiO_2$ Photoanodes for High Efficiency Dye-Sensitized Solar Cells. *J. Phys. Chem. C* **2013**, 117 (28), 14510–14517.
4. Yang, K.; Fu, J.; Hu, L.; Xiong, Z.; Li, M.; Wei, X.; Xiao, Z.; Lu, S.; Sun, K. Impact of ZnO Photoluminescence on Organic Photovoltaic Performance. *ACS Appl. Mater. Interfaces* **2018**, 10 (46), 39962–39969.
5. Xu, Z.; Jiang, Y.; Li, Z.; Chen, C.; Kong, X.; Chen, Y.; Zhou, G.; Liu, J.; Kempa, K.; Gao, J. Rapid Microwave-Assisted Synthesis of $SnO_2$ Quantum Dots for Efficient Planar Perovskite Solar Cells. *ACS Appl. Energy Mater.* **2021** 4 (2), 1887-1893.
6. Rao, A. D.; Karalatti, S.; Thomas, T.; Ramamurthy, P. C. Self-Assembled, Aligned ZnO Nanorod Buffer Layers for High-Current-Density, Inverted Organic Photovoltaics. *ACS Appl. Mater. Interfaces* **2014**, 6 (19), 16792–16799.
7. Dimple, D.; Lebègue, S.; Pastore, M. Dye Anchoring on $CuCrO_2$ Surfaces for P-Type Dye-Sensitized Solar Cell Applications: An Ab Initio Study. *ACS Appl. Energy Mater*. **2021**, 4 (6), 6180–6190.
8. Powar, S.; Xiong, D.; Daeneke, T.; Ma, M. T.; Gupta, A.; Lee, G.; Makuta, S.; Tachibana, Y.; Chen, W.; Spiccia, L.; Cheng, Y.-B.; Götz, G.; Bäuerle, P.; Bach, U. Improved Photovoltages for P-Type Dye-Sensitized Solar Cells Using $CuCrO_2$ Nanoparticles. *J. Phys. Chem. C* **2014**, 118 (30), 16375–16379.
9. Kawazoe, H.; Yasukawa, M.; Hyodo, H.; Kurita, M.; Yanagi, H.; Hosono, H. P-Type Electrical Conduction in Transparent Thin Films of $CuAlO_2$. *Nature* **1997**, 389 (6654), 939–942.
10. Hautier, G.; Miglio, A.; Ceder, G.; Rignanese, G.-M.; Gonze, X. Identification and Design Principles of Low Hole Effective Mass P-Type Transparent Conducting Oxides. *Nat. Commun*. **2013**, 4 (1), 2292.
11. Zhao, R.-D.; Zhang, Y.-M.; Liu, Q.-L.; Zhao, Z.-Y. Effects of the Preparation Process on the Photocatalytic Performance of Delafossite $CuCrO_2$. *Inorg. Chem*. **2020**, 59 (22), 16679–16689.
12. Shannon, R. D.; Rogers, D. B.; Prewitt, C. T. Chemistry of Noble Metal Oxides. I. Syntheses and Properties of $ABO_2$ Delafossite Compounds. *Inorg. Chem*. **1971**, 10 (4), 713–718.
13. Croft, W. J.; Tombs, N. C.; England, R. E. Crystallographic Data for Pure Crystalline Silver Ferrite. *Acta Crystallogr*. **1964**, 17 (3), 313–313.
14. Sheets, W. C.; Mugnier, E.; Barnabé, A.; Marks, T. J.; Poeppelmeier, K. R. Hydrothermal Synthesis of Delafossite-Type Oxides. *Chem. Mater*. **2006**, 18 (1), 7–20.

15. Wang, J.; Ibarra, V.; Barrera, D.; Xu, L.; Lee, Y.-J.; Hsu, J. W. P. Solution Synthesized P-Type Copper Gallium Oxide Nanoplates as Hole Transport Layer for Organic Photovoltaic Devices. *J. Phys. Chem. Lett*. **2015**, 6 (6), 1071–1075.
16. Kumar, S.; Miclau, M.; Martin, C. Hydrothermal Synthesis of $AgCrO_2$ Delafossite in Supercritical Water: A New Single-Step Process. *Chem. Mater*. **2013**, 25 (10), 2083–2088.
17. Xiong, D.; Zeng, X.; Zhang, W.; Wang, H.; Zhao, X.; Chen, W.; Cheng, Y. Synthesis and Characterization of $CuAlO_2$ and $AgAlO_2$ Delafossite Oxides through Low-Temperature Hydrothermal Methods. *Inorg. Chem.* **2014** 53 (8), 4106-4116.
18. Xiong, D.; Xu, Z.; Zeng, X.; Zhang, W.; Chen, W.; Xu, X.; Wang, M.; Cheng, Y.-B. Hydrothermal Synthesis of Ultrasmall $CuCrO_2$ Nanocrystal Alternatives to NiO Nanoparticles in Efficient P-Type Dye-Sensitized Solar Cells. *J. Mater. Chem*. **2012**, 22 (47), 24760–24768.
19. Hoffmann, M. M.; Darab, J. G.; Fulton, J. L. An Infrared and X-Ray Absorption Study of the Structure and Equilibrium of Chromate, Bichromate, and Dichromate in High-Temperature Aqueous Solutions. *J. Phys. Chem. A* **2001**, 105 (28), 6876–6885.
20. Creissen, C. E.; Warnan, J.; Antón-García, D.; Farré, Y.; Odobel, F.; Reisner, E. Inverse Opal $CuCrO_2$ Photocathodes for $H_2$ Production Using Organic Dyes and a Molecular Ni Catalyst. *ACS Catal*. **2019**, 9 (10), 9530–9538.
21. Ketir, W.; Saadi, S.; Trari, M. Physical and Photoelectrochemical Characterization of $CuCrO_2$ Single Crystal. *J. Solid State Electrochem*. **2012**, 16 (1), 213–218.
22. Beverskog, B.; Puigdomenech, I. Revised Pourbaix Diagrams for Copper at 25 to 300°C. *J. Electrochem. Soc*. **1997**, 144 (10), 3476–3483.
23. Beverskog, B.; Puigdomenech, I. Revised Pourbaix Diagrams for Chromium at 25–300 °C. *Corros. Sci*. **1997**, 39 (1), 43–57.
24. Sanchez-Hachair, A.; Hofmann, A. Hexavalent Chromium Quantification in Solution: Comparing Direct UV–Visible Spectrometry with 1,5-Diphenylcarbazide Colorimetry. *Comptes Rendus Chim*. **2018**, 21 (9), 890–896.
25. Leita, L.; Margon, A.; Pastrello, A.; Arčon, I.; Contin, M.; Mosetti, D. Soil Humic Acids May Favour the Persistence of Hexavalent Chromium in Soil. *Environ. Pollut*. **2009**, 157 (6), 1862–1866.
26. Kerridge, D. H.; Mosley, M. Molten Potassium Thiocyanate: Reactions with Compounds of Chromium. *J. Chem. Soc. Inorg. Phys. Theor*. **1967**, 1874.
27. Liu, H.; Zhu, W.; Ding, X.; Huang, Y.; Bo, M. Abnormal Deviation of Temperature–Resistivity Correlation for Nanostructured Delafossite $CuCrO_2$ Due to Local Reconfiguration. *J. Phys. Chem. C* **2020**, 124 (52), 28555–28561.
28. Jiang, T.; Li, X.; Bujoli-Doeuff, M.; Gautron, E.; Cario, L.; Jobic, S.; Gautier, R. Modulation of Defects in Semiconductors by Facile and Controllable Reduction: The Case of p-Type $CuCrO_2$ Nanoparticles. *Inorg. Chem*. **2016**, 55 (15), 7729–7733.
29. Bredar, A. R. C.; Blanchet, M. D.; Comes, R. B.; Farnum, B. H. Evidence and Influence of Copper Vacancies in P-Type $CuGaO_2$ Mesoporous Films. *ACS Appl. Energy Mater*. **2019**, 2 (1), 19–28.
30. Yu, M.; Draskovic, T. I.; Wu, Y. Understanding the Crystallization Mechanism of Delafossite $CuGaO_2$ for Controlled Hydrothermal Synthesis of Nanoparticles and Nanoplates. *Inorg. Chem*. **2014**, 53 (11), 5845–5851.

31. Subramaniam, T.; Kesavan, G.; Venkatachalam, G. Development of $CuAlO_2$-Encapsulated Reduced Graphene Oxide Nanocomposites: An Efficient and Selective Electrocatalyst for Detection of Neurodegenerative Disorders. *ACS Appl. Bio Mater*. **2020**, 3 (11), 7769–7778.
32. Draskovic, T. I.; Yu, M.; Wu, Y. 2H-CuScO 2 Prepared by Low-Temperature Hydrothermal Methods and Post-Annealing Effects on Optical and Photoelectrochemical Properties. *Inorg. Chem*. **2015**, 54 (11), 5519–5526.

# Lithium Dependent Electrochemistry of p-Type Nanocrystalline $CuCrO_2$ Films

## *4.1 Introduction*

N-type and p-type metal oxides have found great use as selective contacts in a variety of heterojunction solar cell architectures including dye-sensitized solar cells, quantum dot solar cells, organic photovoltaics, and perovskite solar cells.[1–6] N-type materials such as $TiO_2$, $SnO_2$, and ZnO are used to selectively move electrons from light absorbers to the external circuit.[7–11] Likewise, p-type materials such as NiO and $CuMO_2$ ($M = Cr^{3+}$, $Ga^{3+}$) are used to accept and transport holes from light absorbers to the external circuit.[12,13] Given the interfacial relationship between the metal oxide and light absorbers required for charge transfer, a fundamental understanding of the band structure and surface electronic states of these materials is important. The electrochemical features which describe band edges and surface states for n-type oxides $TiO_2$, $SnO_2$, and ZnO and p-type NiO have been well studied in the literature;[1–3,7,8] however, only a handful of studies have presented such data for $CuMO_2$ materials.[14–19] Further understanding of the electrochemical behavior of $CuMO_2$ oxides could provide insight into how to fully utilize them in solar cell architectures.

$CuMO_2$ oxides are a variable class of materials with a wide range of $M^{3+}$ cations able to be incorporated. $CuCrO_2$ and $CuGaO_2$ have become popular choices for p-type hole transport materials for solar cells due to their wide direct band gaps, 3.3 and 3.6 eV, respectively.[14,20] The delafossite crystal structure (**Figure 4.1**) of these materials lends itself to hole transport through the $Cu^+$ sheets sandwiched between edge-shared $M^{3+}O_6$ octahedra. This layered structure in turn results in hexagonal plate-like nanocrystal morphologies with anisotropic hole transport. For example, the diffusion coefficient parallel to the $Cu^+$ plane has been measured to be ~25x larger than the diffusion coefficient perpendicular to the plane for $CuAlO_2$.[21]

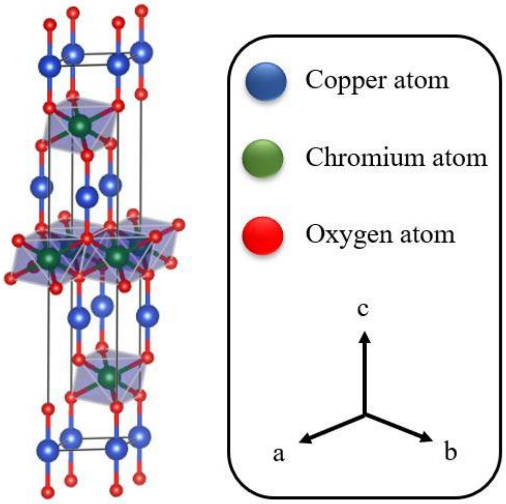

**Figure 4.1.** Delafossite unit cell for $CuCrO_2$ in 3R phase.

The band structure of copper delafossite materials has been thoroughly investigated by theoretical means to conclude that the valence band contains a mixture of copper based 3d-orbitals and oxygen based 2p-orbitals.[22,23] Electrochemical determination of the valence band edges of $CuCrO_2$ and $CuGaO_2$ have been determined from Mott-Schottky measurements to be 0.8 V and 0.6 V vs NHE in 0.1 M $Na_2HPO_4$ electrolyte solution.[14,24,25] In the case of $CuGaO_2$, the valence band edge aligns well with a quasireversible feature observed with cyclic voltammetry and assigned to a $Cu^{2+/+}$ surface redox state induced by copper vacancy defects.[26] Similar surface defects have been described for p-type NiO, which also shares a similar band structure involving overlap of transition metal 3d-orbitals and oxygen 2p-orbitals.[27] The impact of these surface defects on the performance of dye-sensitized solar cells has also been of great interest in the literature as they can act as recombination centers with reduced dye molecules and redox mediators.[27] Numerous studies have shown that passivation of these states using targeted atomic deposition to fill nickel vacancies with redox inert $M^{3+}$ cations in the lattice or atomic layer deposition of nanometer thick redox inert oxide materials (*e.g.* $Al_2O_3$) results in larger photovoltages but decreased photocurrent.[27,2829]

Given the layered delafossite structure of $CuMO_2$ materials and the hexagonal plate-like morphology of nanocrystals, it is important to consider that copper-based charge transfer through either surface defect states or valence band states should be more favored along the "sides" of the nanocrystal where copper atoms terminate the lattice as opposed to the "top and bottom" where $M^{3+}$ cations form a close-packed layer of edge-shared octahedra. Changes in aspect ratio of the nanocrystals may therefore impact the magnitude of the surface defect sites and/or the propensity of the material to perform charge transfer with light absorbing molecules and materials.

Here, we describe the electrochemical features of $CuCrO_2$ nanocrystals deposited as thin film electrodes on conductive glass. The preparation of $CuCrO_2$ and generation of the electrodes is designed to be consistent with how these materials would be used in heterojunction solar cells, particularly within dye-sensitized architectures. All experiments were performed with redox-inert electrolyte without the presence of light absorbing molecules so that the electrochemistry of the $CuCrO_2$ surface and valence band could be measured directly. Using a combination of electrochemical and spectroscopic methods, we show that quasi-reversible redox features at the electrode surface are consistent with $Cu^{2+/+}$ surface defects which are further activated by the presence of $Li^+$ in the electrolyte. The impact of these findings on the use of $CuCrO_2$ in heterojunction solar cells and electrochemical energy storage is further discussed.

## *4.2 Experimental*

### *4.2.1 Synthesis of $CuCrO_2$ and $CuGaO_2$ Nanocrystals*

An optimized hydrothermal synthetic procedure was followed as previously reported for delafossite $CuCrO_2$ nanocrystals.[30] 20 mmol of chromium nitrate nonahydrate [$Cr(NO_3)_3 \cdot 9\ H_2O$] (Alfa Aesar, 98.5%) and 15 mmol copper nitrate hemipentahydrate [$Cu(NO_3)_2 \cdot 2.5\ H_2O$] (Alfa Aesar, 98%+) were added to 70 mL deionized $H_2O$ (18 MΩ cm, Milli-Q) and stirred in an ice bath. After the precursors in water reached 5 ˚C, 7.03 g KOH (VWR Analytical) was added. The pH was measured before transferring the mixture into a 45 mL Teflon cup in order to ensure the solution pH > 13.

After transferring the mixture to the Teflon cup and sealing in an acid digestion bomb (Parr), the vessel was placed into a box furnace (Lindberg Blue M) and heated to 240 ˚C for 60 hours. After cooling to room temperature, the bomb was removed and the resulting mixture was centrifuged to separate the solid product from solution. The solid was dried and analyzed using powder X-ray diffraction before submerging in a 0.5 M $NH_4OH$ (28 vol %, BDH) solution for 24 hours to allow for dissolution of impurities. The remaining product was rinsed with ethanol (Koptec, 200 Proof), ultrasonicated (Branson 150), and vortexed (VWR Analog Vortex Mixer) three times before allowing the product to dry in ethanol under a fume hood. The product was then placed in a vacuum oven (VWR) at 60 ˚C until further use.

$CuGaO_2$ was grown using a synthetic procedure previously reported.[31] 5 mmol of $Cu(NO_3)_2 \cdot 2.5\ H_2O$ (Alfa Aesar, 98%+) and 5 mmol $Ga(NO_3)_3 \cdot H_2O$ (Alfa Aesar, 99.99%) were dissolved in 15 mL deionized $H_2O$ (18 MΩ cm, Milli-Q). The solution was chilled and stirred in an ice bath for 1 hour before adding 2.5 M KOH solution in 1 mL increments until the pH ~9. The final solution was transferred into a 45 mL Teflon-lined acid digestion bomb and placed into a box furnace at

190 ˚C for 24 hours. After cooling to room temperature, the solution was centrifuged and the solid product was separated from the aqueous solution and washed with ammonium hydroxide ($NH_4OH$, 28 % vol, BDH) to remove any $Cu_2O$ impurities. The final product was washed with deionized water three times before a final acetone wash and dried in a vacuum oven.

### *4.2.2 Thin Film Electrode Fabrication*

Viscous pastes of $CuCrO_2$ and $CuGaO_2$ nanocrystals in ethanol solution were made using a 2:1 ratio of $CuCrO_2$:ethyl cellulose (Acros Organics, 10 cP) where the final mixture contained 13 wt % $CuCrO_2$. Pastes were allowed to stir overnight to ensure homogeneity.

FTO glass ($SnO_2$:F, 15 $\Omega/cm^2$, Hartford Glass, Inc.) was used as the conductive substrate and was prepared for deposition by sonication (Branson 3800) in a 0.1 M HCl (Gracs, 36%) ethanol solution for 20 minutes, followed by sonication in pure ethanol for 20 minutes. The glass was air dried, and $CuCrO_2$ or $CuGaO_2$ pastes were spin coated (Laurell WS650 MHz 23 NPPB) onto the FTO glass at 4,000 rpm for 30 seconds. After spin coating, the films were inserted into a tube furnace (Lindberg Blue M) at 350 ˚C for 30 minutes (296 mL/min flow rate) under flowing Ar (99.999%, Airgas). After allowing the films to cool to room temperature, they were placed in a desiccator until needed for electrochemical characterization.

### *4.2.3 Physical Characterization*

Powder X-ray diffraction (pXRD) data was collected using a Rigaku SmartLab X-Ray diffractometer with a Cu Kα source. XPS of the thin films was collected using a Physical Electronics (PHI) 5400 system with a monochromatic Al Kα source. High resolution scans of the O 1s, Cu 2p, and Cr 2p peaks were performed with a pass energy of 35.75 eV and a step size of

0.05 eV. The Casa XPS fitting software was used for all data analysis and fitting. Scanning electron microscopy (SEM) images were collected using a Hitachi S-4700. Transmission electron microscopy (TEM) images were collected using a Thermo Scientific Talos F200X. Thickness measurements of films were conducted using a Veeco Dektak 150 Stylus Surface Profilometer.

Surface area measurements of $CuCrO_2$ and $CuGaO_2$ thin films were performed using adsorption and desorption of a molecular dye. Films were first allowed to soak in a 300 μM P1 dye solution in acetonitrile for 24 hours (P1 = 4-(Bis- {4-[5-(2,2-dicyano-vinyl)-thiophene-2-yl]-phenyl}-amino)-benzoic acid, Dyenamo > 95%). Films were then removed, rinsed with acetonitrile (MeCN), and then placed in a solution of 0.1 M KOH (BDH VWR Analytical) in 1:1 MeCN:$H_2O$ (BDH:Milli-Q, 18 MΩ cm) to desorb all dye molecules from the oxide surface. The resulting solution was analyzed using an Agilent Cary 8454 UV-visible spectrophotometer to determine the amount of dye desorbed based on the solution volume and the extinction coefficient at 418 nm determined to be 42,000 $M^{-1}$ $cm^{-1}$ in 0.1 M KOH 1:1 MeCN:$H_2O$ solution.[32] An estimated molecular footprint of the P1 dye ($1.1 \times 10^{10}$ $cm^2$ $mol^{-1}$) was then used to calculate the approximate surface area of $CuCrO_2$ and $CuGaO_2$ films.

### *4.2.4 Electrochemical Characterization*

A Gamry 1010E potentiostat was used to conduct all electrochemical experiments with a 3-electrode electrochemical cell where the reference was an aqueous Ag/AgCl electrode (satd. KCl; BASi), the counter electrode was platinum mesh (BASi), and the working electrode was $CuCrO_2$ or $CuGaO_2$ thin films deposited on FTO glass. Cyclic voltammetry of an external ferrocene standard in acetonitrile with 0.1 M $LiClO_4$ electrolyte was performed before and after every experiment to ensure no potential drift was observed in the reference electrode. 0.1 M electrolyte solutions in MeCN containing $LiClO_4$ (99.99%, Millipore Sigma) and/or $TBAClO_4$ (BTC, 2537-36-2) were used to conduct all experiments. Nitrogen was used to purge the electrolyte solution before and during each experiment.

## *4.3 Results and Discussion*

### *4.3.1 Structural Characterization of $CuCrO_2$*

$CuCrO_2$ nanocrystals were synthesized following a previously published procedure from our group.[30] Solid material produced from that study were further used for experiments reported here, thus some characterization methods have been previously reported. Powder diffractograms are shown in **Figure 4.2a** for the synthesized $CuCrO_2$ nanocrystals after washing in 0.5 M $NH_4OH$ for 24 hours. Distinct peaks are present at 31.0˚, 36.2˚, and 61.7˚ characteristic of the (006), (012), and (110) peaks, respectively for delafossite $CuCrO_2$ in the 3R phase (PDF #00-039-0247). The broad nature of the diffraction peaks was consistent with nanocrystalline particle sizes as observed in TEM images (**Figure 4.2b**). The anisotropic nanocrystals measured 22.9 ± 5.5 nm in width and 5.0 ± 1.7 nm in thickness, resulting in an aspect ratio of 4.6 ± 1.9. As previously reported, elemental analysis using ICP-MS found a 4.0 ± 1.5 atomic % deficiency in copper atoms compared with chromium, indicating the possible presence of copper vacancy defects.[30,33]

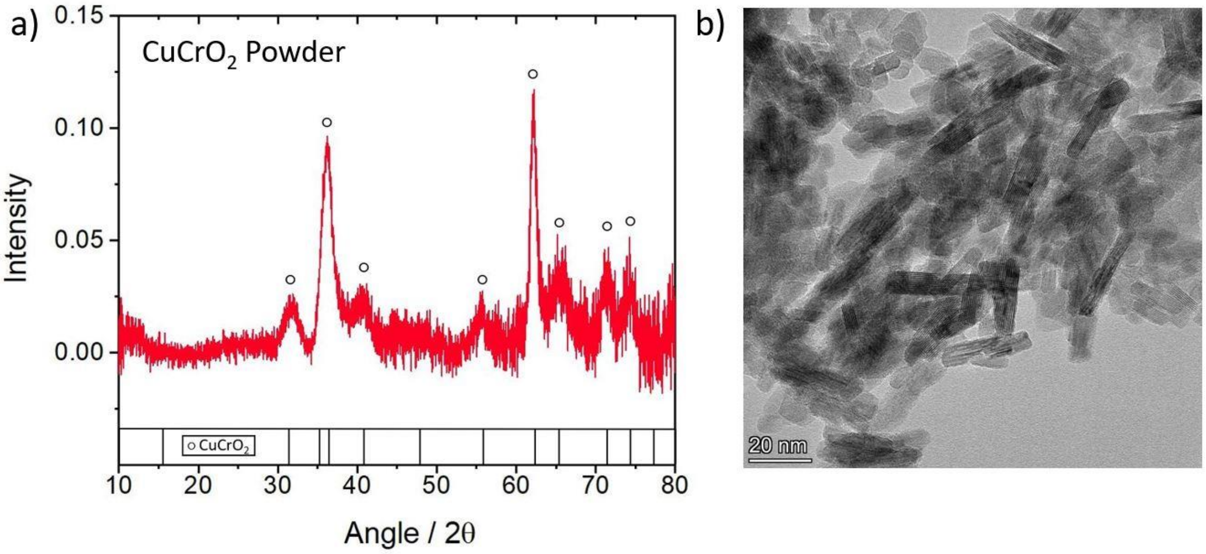

**Figure 4.2. a)** Powder X-ray diffractogram of synthesized CuCrO$_2$ powder. A standard diffraction pattern for CuCrO$_2$ (PDF #00-039-0247) is shown for comparison. **b)** TEM image of CuCrO$_2$ nanocrystals.

CuCrO$_2$ nanocrystals were mixed with ethyl cellulose and ethanol to form a viscous paste and dispersed onto conductive FTO glass using a spin coater to result in thin films of 1.43 ± 0.20 µm thickness. Films were then annealed at 350 °C to remove ethyl cellulose. **Figure S4.1** shows powder diffractograms collected pre- and post-annealing to confirm the integrity of the CuCrO$_2$ solid. XPS studies on post-annealed CuCrO$_2$ films also supported the conclusion that Cu$^{2+}$ sites are present to charge compensate for Cu$^{+}$ vacancies seen from ICP results, as previously reported.[30] **Figure S4.2** shows Cu XPS spectra where the Cu region indicates a peak at 936.7 eV assigned to Cu$^{2+}$.

### *4.3.2 CV Electrochemical Characterization of $CuCrO_2$ vs $CuGaO_2$ Films*

Post-annealed $CuCrO_2$ films deposited on FTO glass were used directly as working electrodes in three-electrode electrochemical cells. **Figure 4.3a** shows cyclic voltammograms collected at 10 mV/s for $CuCrO_2$ electrodes in MeCN solution with different electrolytes. The total ionic strength was fixed at 0.1 M for all experiments, but the amount of $LiClO_4$ and $TBAClO_4$ were varied to adjust the concentration of $[Li^+]$. Starting at 0 M $[Li^+]$ (*i.e.* 0.1 M $TBAClO_4$), the observed anodic and cathodic currents were relatively low with small peaks at $E_{pa}$ = 0.18 and $E_{pc}$ = -0.13 V vs $Fc^{+/0}$, yielding an $E_{1/2}$ = 0.03 V. A much larger anodic feature was observed to begin around 0.5 V which was found to be consistent across all $[Li^+]$ electrolyte conditions. As $Li^+$ was introduced into the electrolyte, the $E_{pa}$ and $E_{pc}$ values appeared to shift positively to 0.24 and 0.03 V, respectively, at 0.1 M $[Li^+]$ with an $E_{1/2}$ = 0.14 V. In addition, a new quasi-reversible redox feature was observed to increase in anodic current with an increase in $[Li^+]$ centered at $E_{1/2}$ = -0.43 V ($E_{pa}$ = -0.05 V, $E_{pc}$ = -0.81 V) for 0.1 M $LiClO_4$. The cathodic peak for this new feature shifted positively from potentials less than -1.5 V to the final peak position of -0.8 V as $[Li^+]$ increased.

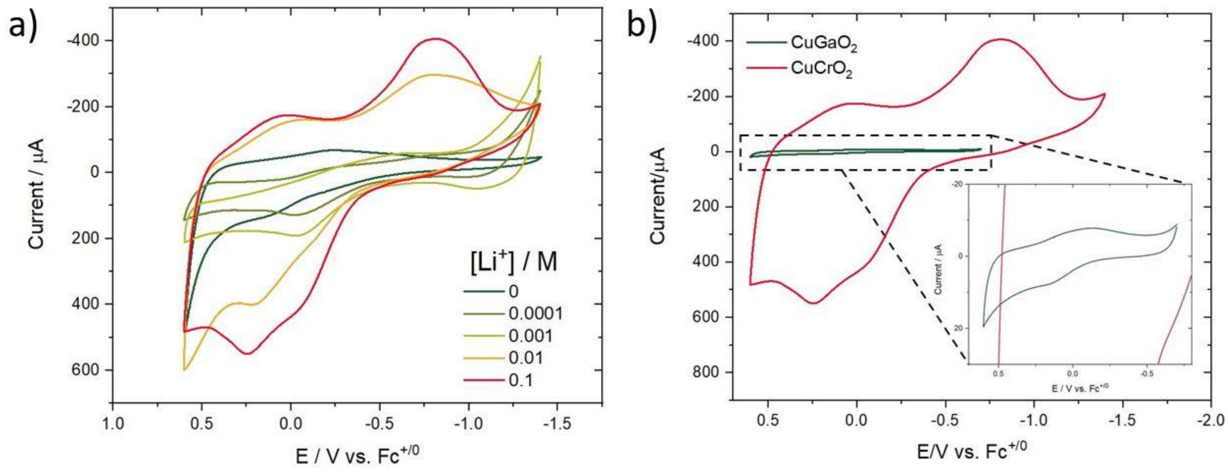

**Figure 4.3. a)** Comparison of CVs of the optimized $CuCrO_2$ thin film at 10 mV/s in electrolyte solutions containing mixtures of 0.1 M $LiClO_4$ and 0.1 M $TBAClO_4$ in MeCN. The total

concentration was held constant at 0.1 M, however, the amount of $Li^+$ was varied across the series. **b)** CV of $CuGaO_2$ vs $CuCrO_2$ thin films in 0.1 M $LiClO_4$ in MeCN at 10 mV/s. **(inset)** A zoomed in image of the CV for $CuGaO_2$.

Similar studies on $CuGaO_2$ nanocrystalline films in MeCN with 0.1 M $LiClO_4$ have reported a quasi-reversible redox feature with $E_{1/2}$ = 0.1 V vs $Fc^{+/0}$, assigned to a $Cu^{2+/+}$ redox couple.[26] Given that these studies were performed at much higher scan rates and without a comparison to 0 M [$Li^+$], we synthesized $CuGaO_2$ according to this previous report and generated comparable nanocrystalline films for electrochemical measurements. **Figure 4.3b** shows an overlay of the two materials, $CuCrO_2$ and $CuGaO_2$, in MeCN with 0.1 M $LiClO_4$ electrolyte. The current observed for $CuCrO_2$ greatly outweighs that observed for $CuGaO_2$. Some of this difference in current can be accounted for by the greater internal surface area observed for $CuCrO_2$ films (345 ± 63 $cm^2$) than for $CuGaO_2$ films (162 ± 25 $cm^2$), **Table S4.1-2**. However, this would represent only a ~2-fold increase in current for $CuCrO_2$ based on surface area, instead of the ~50-fold greater current observed in **Figure 4.3b**. Nanocrystals of $CuGaO_2$ were also found to be much larger (width = 343 ± 71 nm; thickness = 40 ± 10 nm; aspect ratio = 8.6 ± 2.8) than $CuCrO_2$ and found to have significant particle stacking within the film structure **(Figure S4.3),** consistent with the literature.[26] Based on the delafossite crystal structure which only features copper surface terminations along the "sides" of the nanocrystals (e.g. (100) and (010) planes), the larger aspect ratio found for $CuGaO_2$ nanocrystals could further limit the percentage of the surface area terminated in electrochemically active copper sites. Notably, when the electrochemistry of a $CuGaO_2$ film was measured in 0.1 M $TBAClO_4$, the $Cu^{2+/+}$ redox feature disappeared and the voltammogram was featureless until the potential exceeded 0.2 V vs $Fc^{+/0}$ where an irreversible oxidation was observed

(**Figure S4.4**). This observation supports the idea that $Li^+$ dependent redox chemistry is associated with $Cu^{2+/+}$ redox chemistry.

### *4.3.3 Chronoamperometry and $Li^+$ Dependence of $CuCrO_2$ Films*

Chronoamperometry experiments were conducted for $CuCrO_2$ films to quantitatively measure the increase in anodic and cathodic current with $[Li^+]$. Data were collected for a series of electrolyte solutions in 3 steps, with step 1 holding at -1.3 V vs $Fc^{+/0}$, followed by step 2 at 0.3 V, and returning to -1.3 V for step 3. These potentials were chosen so that a majority of the redox features could be captured without entering the irreversible oxidation observed near 0.5 V. Current versus time data is plotted in **Figure S4.5** for each step and electrolyte condition. These data were then integrated to calculate the total charge passed as a function of time. Surprisingly, the measured charges for each step (**Figures S4.6-S7** and **Figure 4.4a**) were found to be linear with $t^{1/2}$ at long times according to the **Equation 4.1**. This equation, known as the Anson equation, implies that faradaic current is being observed due to diffusion limited transfer of an electroactive species from solution to the electrode surface. However, in these experiments, the electrolyte is redox-inert, and this behavior must be explained by either diffusion of $Li^+$, $TBA^+$, or $ClO_4^-$ to charge-balance redox changes within the $CuCrO_2$ film and/or diffusion of electrons/holes through the $CuCrO_2$ lattice associated with redox changes within the material. The linear slope of the diffusion region for the Anson plot can be used to calculate the diffusion coefficient ($D_o$), however, this requires knowledge of the concentration of electroactive species ($C_o$) and film surface area (A). Assuming the diffusion is the result of electrolyte ions, a concentration of 0.1 M, surface area of 343 $cm^2$, and electron transfer number of $n = 1$ results in diffusion coefficients reported in **Table S4.3**. These values were in the range of $10^{-14} – 10^{-18}$ $cm^2/s$ and are remarkably low for typical ion diffusion through MeCN solvent. This could point to a more activation-controlled diffusion mechanism within the $CuCrO_2$ lattice.

What is more interesting about the Anson plots is that the intercepts from the linear fits, which report on the total adsorbed charge at the electrode surface ($Q_{ads}$), were found to increase and plateau at maximum values as $[Li^+]$ increased (**Table S4.4**). The maximum $|Q_{ads}|$ value measured for each step was 8.4, 12, and 6.8 mC for steps 1, 2, and 3, respectively. The increase in $Q_{ads}$ with $[Li^+]$ for step 2 (0.3 V) is shown in **Figure 4.4b** and was found to fit well to a Langmuir binding isotherm using **Equation 4.2**, where $Q_{max}$ is the maximum surface charge, and K is an equilibrium constant. Fitting to this equation implies an equilibrium between $Li^+$ ions and redox active surface sites of $CuCrO_2$. From this equation, an equilibrium constant $K = 0.057\ M^{-1}$ and maximum surface charge of $Q_{max} = 15.5$ mC were extracted.

$$Q = nFAC_o D_o^{1/2} t^{1/2} \pi^{-1/2} + Q_{ads} \qquad \textbf{eq. 4.1)}$$

$$Q_{ads} = \frac{K * Q_{max} * [Li^+]}{(1 + K * [Li^+])} \qquad \textbf{eq. 4.2)}$$

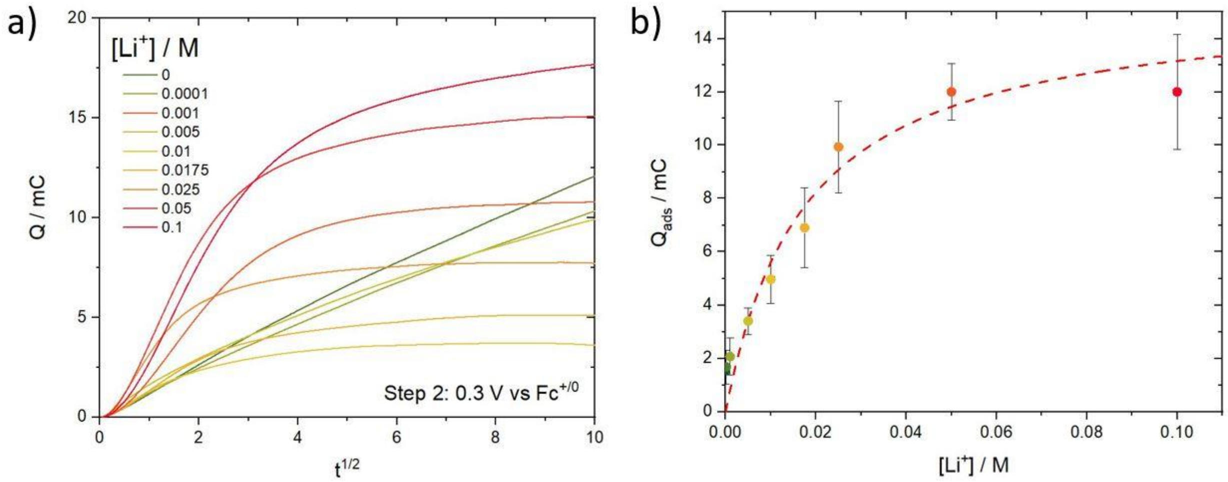

**Figure 4.4. a)** Anson plots constructed from integrated anodic chronoamperometry data using a series of electrolyte solutions with total concentration of 0.1 M and the [Li$^+$] adjusted from 0 M to 0.1 M. Each step was held at the fixed potential 0.3 V vs Fc$^{+/0}$ for 100 seconds**. b)** $Q_{ads}$ plotted as a function of [Li$^+$] in electrolyte solution, fit to the Langmuir adsorption isotherm model.

The impact of small cations on the electrochemical features of metal oxides semiconductors has been well documented in the literature.[34–38] Most notably, cations such as Li$^+$ and H$^+$ have been observed to shift band edges by affecting the Helmholtz layer at the oxide surface to result in ~59 mV anodic shifts per order of magnitude increase in cation concentration. This has been most importantly observed for n-type $TiO_2$ electrodes and is exploited to lower the conduction band edge within dye-sensitized solar cells to allow for greater injection of excited-state electrons.[39–41] For p-type NiO, McCullough et al. have shown the valence band edge to likewise shift in a positive direction with increased charge density of the cation, where Al$^{3+}$ was found to have the greatest shift.[41]

In the present study, we believe that the feature observed at $E_{1/2} = 0.03$ V for 0 M [Li$^+$] is shifted positively to $E_{1/2} = 0.14$ V for 0.1 M [Li$^+$] based on the ability of Li$^+$ to affect the Helmholtz layer. We also believe the increase in current observed for this feature is likely due to the higher double layer capacitance available to $Li^+$ vs $TBA^+$, such that as $TBA^+$ ions are replaced with Li+ in the electrolyte, a higher density of cations can form the double layer at the electrode surface.[42] Distinct from this observation is the new feature that emerged at $E_{1/2} = -0.43$ V for 0.1 M $LiClO_4$. The anodic wave for this feature was found at nearly the same potential for all $[Li^+]$, but increased in magnitude as $[Li^+]$ was increased. On the other hand, the cathodic wave shifted in a positive direction with increased $[Li^+]$ while also increasing in magnitude.

These observations lead to our assignment of a Li-coupled redox feature in which $Li^+$ ions occupy specific sites at the $CuCrO_2$ surface generated by copper vacancy defects. A proposed redox reaction for this feature is shown in **Equation 4.3**. Here, the starting redox state of $CuCrO_2$ is dependent on the number of copper vacancies within the lattice ($x$) where every vacancy generates a corresponding $Cu^{2+}$ ion to compensate charge. Reduction of $Cu^{2+}$ to $Cu^+$ is accompanied by $Li^+$ insertion into the vacant site for charge balance. The positive shift in the cathodic peak could be explained by the fact that $Li^+$ is a reactant and thus increased $[Li^+]$ could shift $E_{pc}$ similar to proton-coupled electron transfer reactions.[43,44] Oxidation of $Cu^+$ back to $Cu^{2+}$ therefore results in release of $Li^+$ ions from copper vacancy sites. Given the specific site occupation, $TBA^+$ ions are too large to occupy these positions and thus, the redox feature is not observed in 0.1 M $TBAClO_4$.

$$Cu^{+}_{1-2x}Cu^{2+}_{x}V_{Cu,x}Cr^{3+}O_2 + xLi^{+} + xe^{-} \rightarrow Cu^{+}_{1-x}Li^{+}_{x}Cr^{3+}O_2 \qquad \textbf{eq. 4.3)}$$

Fitting the surface charge data for the anodic step to a Langmuir binding isotherm implies that $Li^+$ ions bind to particular sites at the surface of $CuCrO_2$ nanocrystals with an equilibrium constant

K = 0.057 $M^{-1}$. Based on **Equation 4.3**, the measured surface charge should therefore be proportional to the number of copper vacancies. Based on a value of 4.0 ± 1.5 % determined from ICP-MS for the same $CuCrO_2$ material published previously, we calculate that the expected charge would be 11 ± 5 mC.[30] The measured surfaces charges of 8.4 mC, 12 mC, and 6.8 mC for each chronoamperometric step are highly consistent with this estimate. It should be noted that the vacancy estimate from ICP-MS is a bulk value and not specific to surface copper vacancies. Therefore, the correlation between the expected charge for total vacancies and the measured charge could indicate that most if not all copper vacancies migrate to the surface of $CuCrO_2$ nanocrystals. Indeed, defect migration to surface sites is common in solid state materials and has been observed for $CuGaO_2$.[31]

### *4.3.4 Chronopotentiometry and Degradative Studies of $CuCrO_2$ Films*

It is also intriguing to think that $Li^+$ ions may be able to intercalate into the interior of the nanocrystal structure to occupy vacant sites in the bulk, given the structural similarities between $CuCrO_2$ and $LiCoO_2$. Both structures contain monovalent cations sandwiched between layers of edge-shared octahedra of trivalent cations. However, $Li^+$ is present in an octahedral coordination environment versus a linear coordination environment for $Cu^+$. To further explore this idea, we performed chronopotentiometric charge-discharge experiments on $CuCrO_2$ nanocrystalline films in MeCN with 0.1 M $LiClO_4$ electrolyte. The results from these experiments are shown in **Figure 4.5** and summarized in **Table S4.5-6**.

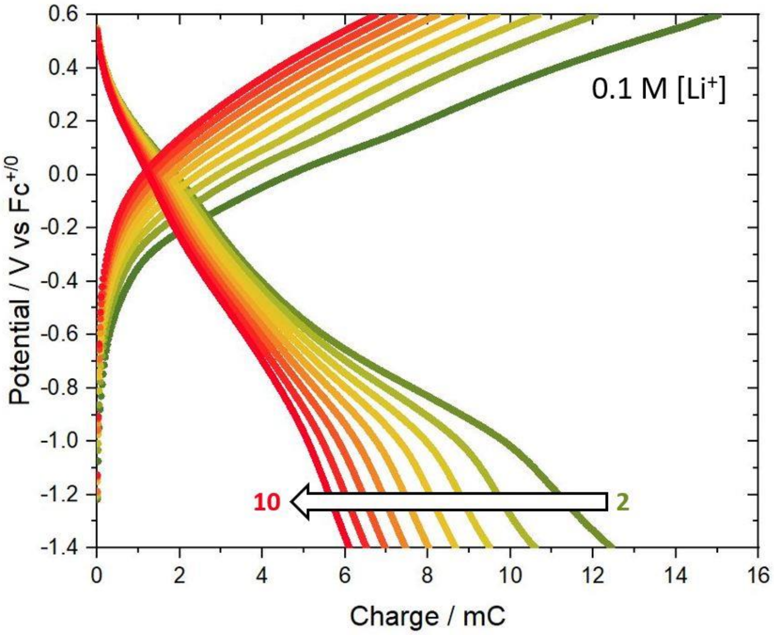

**Figure 4.5.** Cyclic charge-discharge chronopotentiograms for $CuCrO_2$ thin films held at 0.1 mA in 0.1 M $LiClO_4$. An arrow is shown to represent the degradation from cycle 2 (green) to cycle 10 (red).

At cycle 2, the charge observed at 0.6 V vs $Fc^{+/0}$ for $CuCrO_2$ was 15 mC, similar to that found in chronoamperometry experiments. Considering the dimensions of the $CuCrO_2$ film and assuming 50% porosity, 15 mC is equivalent to a 7.8 mA h $g^{-1}$ storage capacity which is comparable to the theoretical 7.0 mA h $g^{-1}$ with 4% copper vacancies present according to **Equation 4.3**. The experimental increase could be due to additional $Li^+$ incorporation into the film at a slightly higher potential. The discharge capacity was consistently much lower than the charge capacity for each cycle with a % cycling efficiency increasing from 83% to 91% over 10 cycles. By cycle 10, the charge capacity for $CuCrO_2$ in $Li^+$ decreased to 3.5 mA h $g^{-1}$. Conversely, the discharge capacity in $Li^+$ by cycle 10 was 3.2 mA h $g^{-1}$, respectively. Extended cycling of CV experiments revealed that the decrease in charge capacity was related to loss of the Li-coupled redox activity, as shown in **Figure 4.6**. Taken together, these data show there is irreversibility in the redox behavior, possibly due to incomplete removal of $Li^+$. The irreversibility could also be due to instability of the film in the form of degradation. Given that $Cu^{2+}$ has a preferential square planar orientation, the increased $Cu^{2+}$ concentration in linearly coordinated sites over the course of cycling could lead to increased strain on the structure, facilitating degradation of the film.

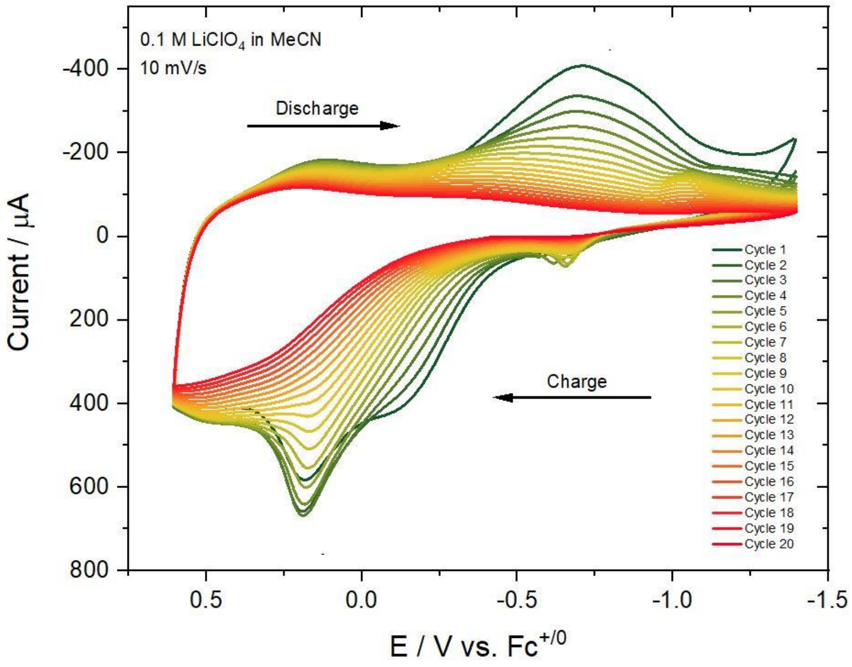

**Figure 4.6.** CV of $CuCrO_2$ film in 0.1 M $LiClO_4$ in MeCN at 10 mV/s scan rate over 20 consecutive cycles.

The pronounced increase in surface charge with increased $Li^+$ has important implications for $CuCrO_2$ nanocrystalline films within heterojunction solar cells. For example, many studies have focused on the impact of NiO surface defects on the performance of dye-sensitized solar cells.[7,8] The presence of such states has been associated with increased hole recombination to molecular dyes and redox mediators, such that passivation of these states has resulted in improved photovoltages. Notably, passivation of surface defects also decreased photocurrent, suggesting that these surface states also have a role to play in accepting holes from excited-state molecules. The surface defects for $CuCrO_2$ were found to be activated by $Li^{+}$ and would be expected to behave in a similar fashion and thus limit the photovoltage of solar cell devices through faster recombination but increase photocurrent by expanding the density of states capable of accepting holes from excited-state molecules. Furthermore, it should be noted that common estimates for the valence band edge of $CuCrO_2$ and $CuGaO_2$ could be erroneously measured due to the onset of surface defects above the true valence band edge.

The ability of $Li^{+}$ to occupy copper vacancy sites within the delafossite lattice also has implications for electrochemical energy storage. Conventional Li-ion batteries with layered cathode structures utilize redox chemistry at the $M^{3+}$ site accompanied by $Li^{+}$ intercalation. In the case of $CuCrO_2$, we have shown that redox chemistry is instead focused on the $Cu^{+}$ site; however, this is not to say that $M^{3+}$ redox chemistry could not be accessed with other delafossite materials. Furthermore, research into the ability to control vacancy formation and ordering within the solid could enhance the reversibility and stability of $Li^{+}$ intercalation within delafossite materials.

### *4.4 Conclusion*

Electrochemical characterization of nanocrystalline $CuCrO_2$ thin films was investigated in which a strong $Li^{+}$ dependence was observed via CV and chronoamperometry experiments. These observations resulted in a proposed redox reaction $Cu^{+}_{1-2x}Cu^{2+}_{x}V_{Cu,x}Cr^{3+}O_2 + xLi^{+} + xe^{-} \rightarrow Cu^{+}_{1-x}Li^{+}_{x}Cr^{3+}O_2$ in which $Li^{+}$ can occupy copper vacancy sites at the film surface. Due to the increased size of $TBA^{+}$, this redox reaction is not observed in the presence of electrolyte containing only $TBA^{+}$. Morphological variations among delafossite metal oxides was also explored and its impact on electrochemical characterization. When compared to its $CuGaO_2$ counterpart, $CuCrO_2$ films exhibited a much greater current in the cyclic voltammograms in 0.1 M $LiClO_4$ in MeCN which can be accounted for by the greater internal surface area of the $CuCrO_2$ films and smaller aspect ratio of nanocrystals. Finally, the redox reaction observed in the presence of $Li^+$ exhibits irreversibility, seen via chronopotentiometry experiments, and could be attributed to incomplete removal of $Li^+$ or degradation from strain caused by the linear coordination sites for $Cu^{2+}$ cations. Future studies to improve the stability of these materials by means of controlling surface copper vacancy formation are needed in efforts to improve the cycling efficiency of the $CuCrO_2$. In addition, photoelectrochemical studies can be explored to understand how such surface defects impact hole recombination in heterojunction solar cells.

### *4.5 Supporting Information*

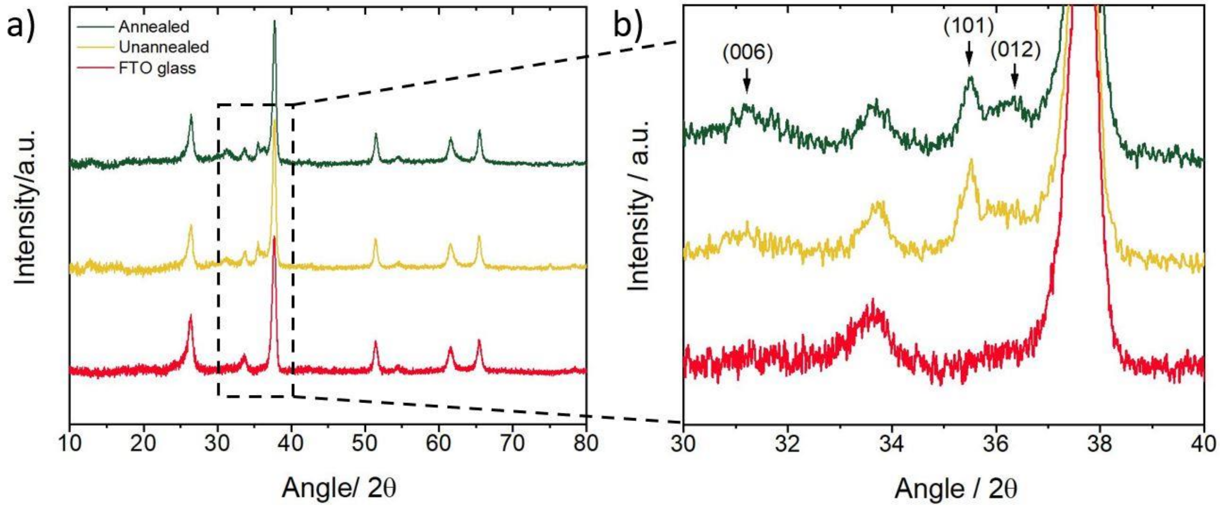

**Figure S4.1. a)** Diffractograms for deposited CuCrO$_2$ thin films on FTO glass before and after annealing under Ar at 350 ˚C for 30 minutes. A diffractogram of blank FTO is also included for comparative purposes. **b)** The diffractograms from part (a) zoomed in to show CuCrO$_2$ (006), (101), and (012) peaks.

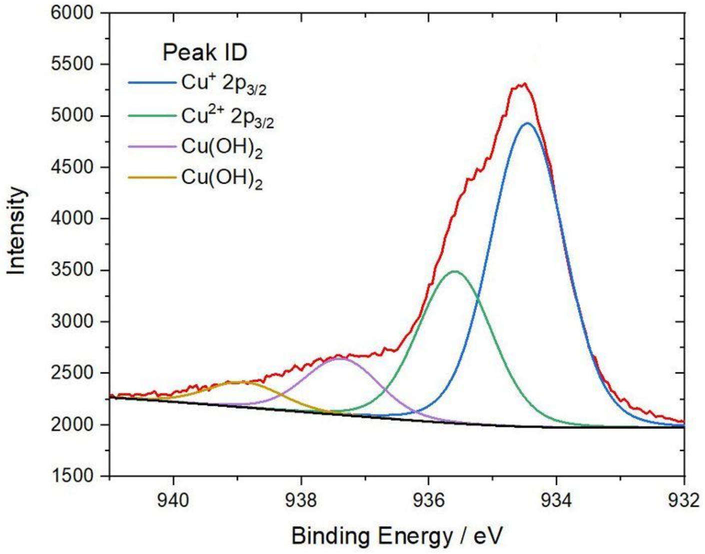

**Figure S4.2.** Cu XPS spectra with fits for a dry CuCrO$_2$ thin film. The peak at 936.7 eV was fit and assigned to Cu$^{2+}$.

**Table S4.1.** Geometric area, thickness, and surface area[a] of $CuCrO_2$ films

| | Film 1 | Film 2 | Film 3 | Average |
|---|---|---|---|---|
| Geometric Area / $cm^2$ | 1.04 | 1.50 | 1.26 | 1.27 ± 0.19 |
| Thickness / μm | 1.45 | 1.17 | 1.67 | 1.43 ± 0.20 |
| P1 dye desorbed / mol | $2.6 \times 10^{-8}$ | $2.7 \times 10^{-8}$ | $3.8 \times 10^{-8}$ | $3.0 \pm 0.7 \times 10^{-8}$ |
| Surface Area / $cm^2$ | 297 | 304 | 434 | 345 ± 63 |

[a] Calculated by multiplying the amount of P1 dye desorbed by $1.1 \times 10^{10}$ $cm^2$/mol

**Table S4.2.** Geometric area, thickness, and surface area[a] of $CuGaO_2$ films

| | Film 1 | Film 2 | Film 3 | Average |
|---|---|---|---|---|
| Geometric Area / $cm^2$ | 1.4 | 1.4 | 1.4 | 1.4 |
| Thickness / μm | 1.58 | 1.81 | 1.45 | 1.61 ± 0.15 |
| P1 dye desorbed / mol | $1.2 \times 10^{-8}$ | $1.3 \times 10^{-8}$ | $1.7 \times 10^{-8}$ | $1.4 \pm 0.3 \times 10^{-8}$ |
| Surface Area / $cm^2$ | 137 | 152 | 195 | 162 ± 25 |

[a] Calculated by multiplying the amount of P1 dye desorbed by $1.1 \times 10^{10}$ $cm^2$/mol

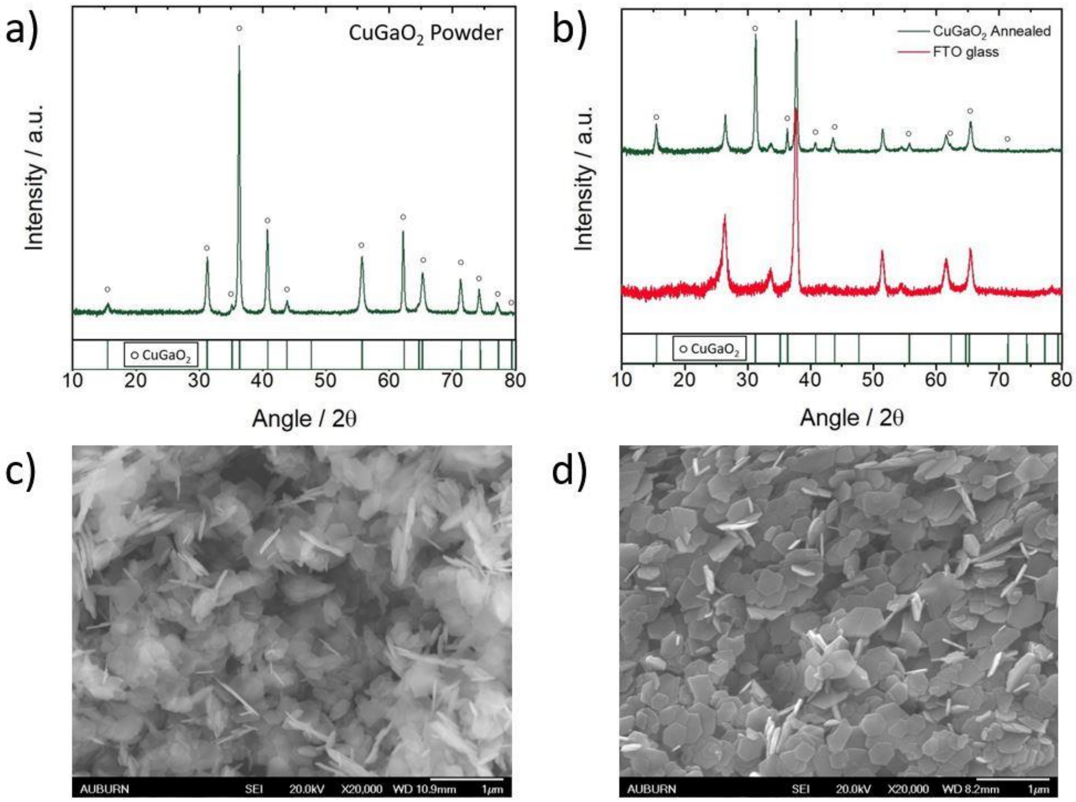

**Figure S4.3. a)** Diffractogram of $CuGaO_2$ powder. A standard diffractogram for $CuGaO_2$ is shown for comparison (PDF 00-041-0255). **b)** Diffractogram of annealed $CuGaO_2$ thin film. A diffractogram of bare FTO glass is provided for comparative purposes. **c)** SEM image of $CuGaO_2$ washed powder. **d)** SEM image of annealed $CuGaO_2$ annealed thin film, showing preferential stacking.

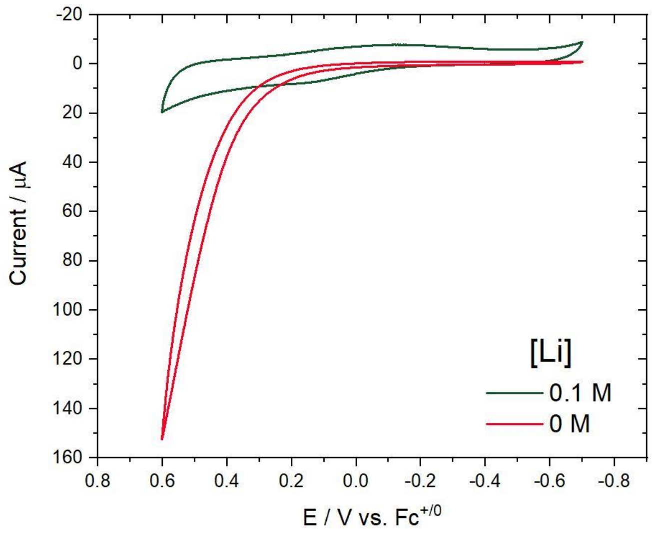

**Figure S4.4.** Cyclic voltammograms of $CuGaO_2$ thin films in 0.1 M $LiClO_4$ in MeCN (0.1 M [Li]) vs 0.1 M $TBAClO_4$ in MeCN (0 M [Li]) at a 10 mV/s scan rate.

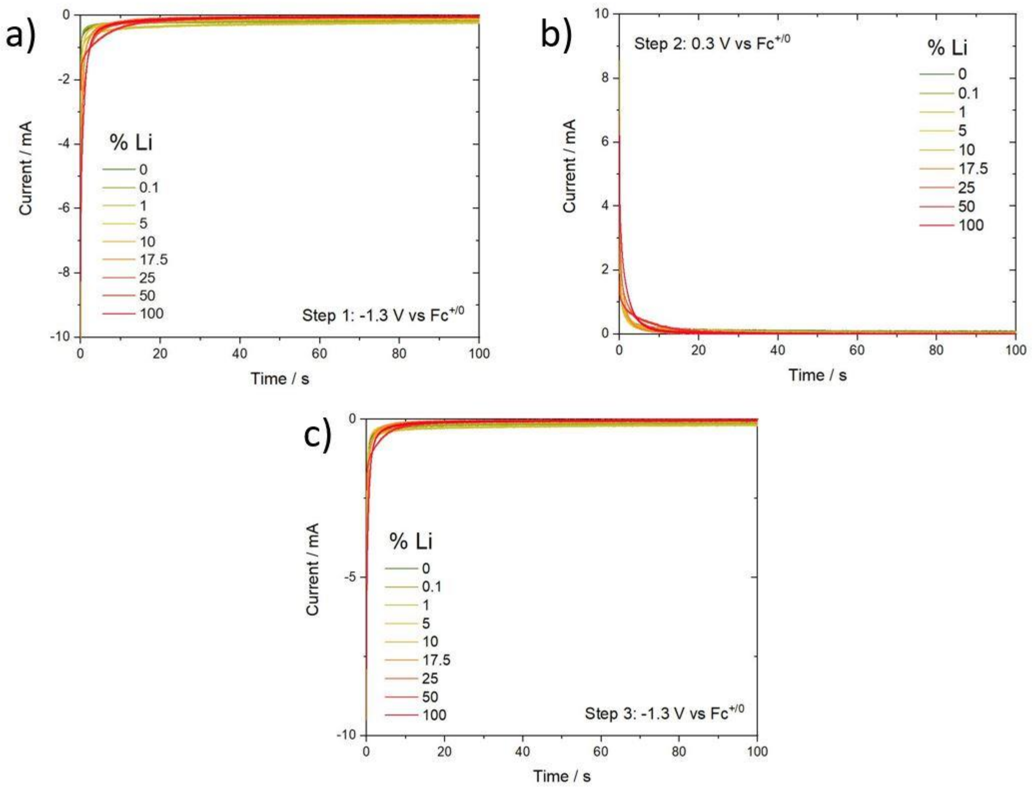

**Figure S4.5.** Amperometric IT curves used to integrate and construct Anson plots for CuCrO$_2$ films in electrolyte solutions of varying Li:TBA concentrations where the total concentration electrolyte = M. A 3 step experiment was conducted in which the potential was held at -1.3 V vs Fc$^{+/0}$ for 100 seconds (step 1), 0.3 V vs Fc$^{+/0}$ for 100 seconds (step 2), and -1.3 V vs Fc$^{+/0}$ for 100 seconds (step 3).

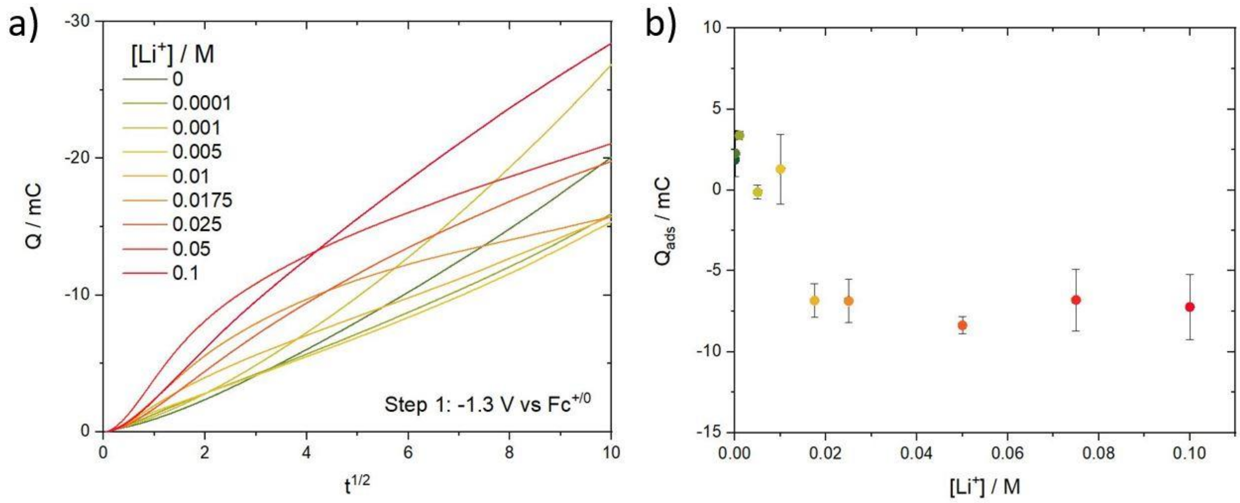

**Figure S4.6. a)** Anson plots constructed from integrated amperometric IT curves using a series of electrolyte solutions with total concentration = 0.1 M, where the [Li$^+$] was adjusted from 0 to 0.1 M. Each step was held at the fixed potential -1.3 V vs Fc$^{+/0}$ for 100 seconds (Step 1). **b)** Q$_{ads}$ plotted as a function of [Li$^+$] in electrolyte solution.

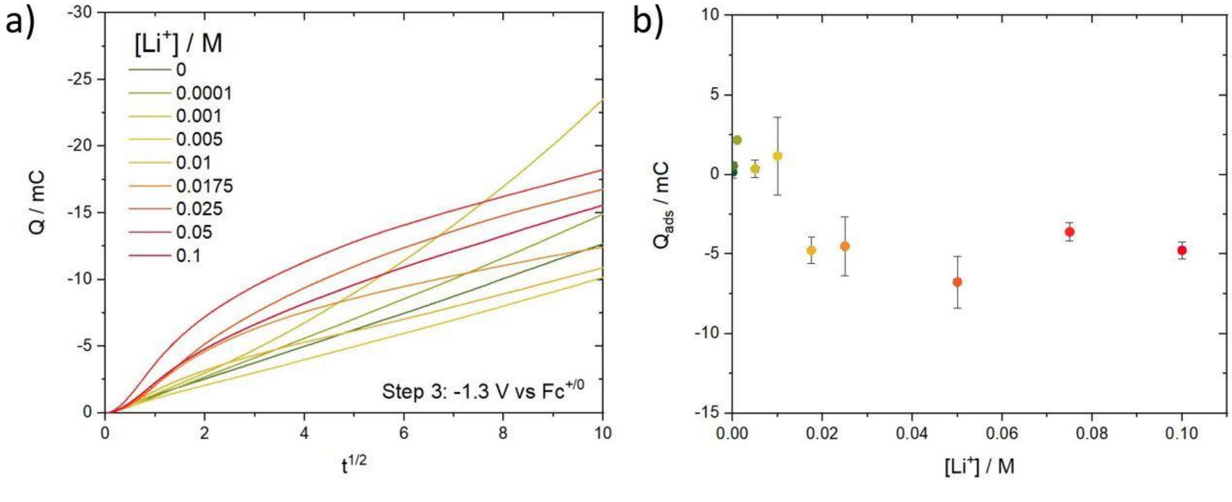

**Figure S4.7. a)** Anson plots constructed from integrated amperometric IT curves using a series of electrolyte solutions with total concentration = 0.1 M, where the [Li$^+$] was adjusted from 0 to 0.1 M. Each step was held at the fixed potential -1.3 V vs Fc$^{+/0}$ for 100 seconds (Step 3). **b)** Q$_{ads}$ plotted as a function of [Li$^+$] in electrolyte solution.

**Table S4.3.** Diffusion coefficients ($D_o$ / $cm^2/s$) determined from Anson plots assuming $C_o$ = 0.1 M, A = 343 $cm^2$, and n = 1. (F = 96485 C/mol).

| **[$Li^+$] / M** | **Step 1 (-1.3 V)** | **Step 2 (0.3 V)** | **Step 3 (-1.3 V)** |
|---|---|---|---|
| 0 | 9.6 ± 1.8 x $10^{-15}$ | 4.1 ± 0.8 x $10^{-15}$ | 7.1 ± 1.9 x $10^{-15}$ |
| 0.0001 | 1.1 ± 0.4 x $10^{-14}$ | 2.0 ± 0.3 x $10^{-15}$ | 1.1 ± 0.3 x $10^{-14}$ |
| 0.0010 | 2.1 ± 0.3 x $10^{-14}$ | 1.7 ± 0.2 x $10^{-15}$ | 1.1 ± 0.6 x $10^{-14}$ |
| 0.0050 | 4.2 ± 1.1 x $10^{-15}$ | 4.8 ± 3.2 x $10^{-18}$ | 8.2 ± 4.9 x $10^{-15}$ |
| 0.0100 | 2.0 ± 1.1 x $10^{-14}$ | 1.1 ± 1.6 x $10^{-16}$ | 1.1 ± 1.4 x $10^{-14}$ |
| 0.0175 | 1.5 ± 0.4 x $10^{-15}$ | 5.6 ± 5.4 x $10^{-18}$ | 1.0 ± 0.3 x $10^{-15}$ |
| 0.0250 | 4.6 ± 2.0 x $10^{-15}$ | 7.1 ± 7.5 x $10^{-17}$ | 2.3 ± 0.7 x $10^{-15}$ |
| 0.0500 | 3.7 ± 1.5 x $10^{-15}$ | 3.1 ± 2.3 x $10^{-17}$ | 2.9 ± 0.1 x $10^{-15}$ |
| 0.1000 | 7.2 ± 6.4 x $10^{-15}$ | 1.3 ± 1.7 x $10^{-16}$ | 2.7 ± 1.1 x $10^{-15}$ |

**Table S4.4.** Adsorbed surface charges ($Q_{ads}$ / mC) determined from Anson plots assuming $C_o$ = 0.1 M, A = 343 $cm^2$, and n = 1. (F = 96485 C/mol).

| **[$Li^+$] / M** | **Step 1 (-1.3 V)** | **Step 2 (0.3 V)** | **Step 3 (-1.3 V)** |
|---|---|---|---|
| 0 | 1.9 ± 0.2 | 1.6 ± 0.2 | 0.2 ± 0.4 |
| 0.0001 | 2.3 ± 1.4 | 1.7 ± 0.6 | 0.5 ± 0.2 |
| 0.0010 | 3.4 ± 0.3 | 2.1 ± 0.7 | 2.2 ± 0.1 |
| 0.0050 | -0.1 ± 0.4 | 3.4 ± 0.5 | 0.4 ± 0.5 |
| 0.0100 | 1.3 ± 2.2 | 5.0 ± 0.9 | 1.2 ± 2.4 |
| 0.0175 | -6.8 ± 1.1 | 6.9 ± 1.5 | -4.8 ± 0.8 |
| 0.0250 | -6.9 ± 1.3 | 9.9 ± 1.7 | -4.5 ± 1.9 |
| 0.0500 | -8.4 ± 0.5 | 12 ± 2.9 | -6.8 ± 1.6 |
| 0.1000 | -7.2 ± 2.0 | 12 ± 2.2 | -4.8 ± 0.5 |

**Table S4.5.** Calculated charge and discharge Q and % cycling efficiencies from $CuCrO_2$ chronopotentiograms in 0.1 M $LiClO_4$ in MeCN.

| Cycle # | Charge Q (mC) | Discharge Q (mC) | % Cycling efficiency |
|---|---|---|---|
| 2 | 15 | 13 | 82.9 |
| 3 | 12 | 11 | 88.0 |
| 4 | 11 | 10 | 89.0 |
| 5 | 9.7 | 8.7 | 89.7 |
| 6 | 8.9 | 8.0 | 90.7 |
| 7 | 8.2 | 7.5 | 90.9 |
| 8 | 7.7 | 7.0 | 90.9 |
| 9 | 7.2 | 6.5 | 90.6 |
| 10 | 6.7 | 6.1 | 90.7 |

**Table S4.6.** Calculated charge and discharge capacity from $CuCrO_2$ chronopotentiograms in 0.1 M $LiClO_4$ in MeCN.

| Cycle # | Charge Capacity / mA h $g^{-1}$ | Discharge Capacity / mA h $g^{-1}$ |
|---|---|---|
| 2 | 7.8 | 6.5 |
| 3 | 6.2 | 5.5 |
| 4 | 5.5 | 4.9 |
| 5 | 5.0 | 4.5 |
| 6 | 4.6 | 4.2 |
| 7 | 4.3 | 3.9 |
| 8 | 4.0 | 3.6 |
| 9 | 3.7 | 3.4 |
| 10 | 3.5 | 3.2 |

### *4.6 References*

1. Zhen, C.; Wu, T.; Chen, R.; Wang, L.; Liu, G.; Cheng, H.-M. Strategies for Modifying $TiO_2$ Based Electron Transport Layers to Boost Perovskite Solar Cells. *ACS Sustainable Chem. Eng.* **2019**, *7* (5), 4586–4618.
2. Toyoda, T.; Shen, Q. Quantum-Dot-Sensitized Solar Cells: Effect of Nanostructured TiO2 Morphologies on Photovoltaic Properties. *J. Phys. Chem. Lett.* **2012**, *3* (14), 1885–1893.
3. Bai, Y.; Mora-Seró, I.; De Angelis, F.; Bisquert, J.; Wang, P. Titanium Dioxide Nanomaterials for Photovoltaic Applications. *Chem. Rev.* **2014**, *114* (19), 10095–10130.
4. Ramasamy, E.; Lee, J. Ordered Mesoporous SnO2−Based Photoanodes for High-Performance Dye-Sensitized Solar Cells. *J. Phys. Chem. C* **2010**, *114* (50), 22032–22037.
5. Anta, J. A.; Guillén, E.; Tena-Zaera, R. ZnO-Based Dye-Sensitized Solar Cells. *J. Phys. Chem. C* **2012**, *116* (21), 11413–11425.
6. Huang, J.; Yin, Z.; Zheng, Q. Applications of ZnO in Organic and Hybrid Solar Cells. *Energy Environ. Sci.* **2011**, *4* (10), 3861–3877.
7. He, J.; Lindström, H.; Hagfeldt, A.; Lindquist, S.-E. Dye-Sensitized Nanostructured p-Type Nickel Oxide Film as a Photocathode for a Solar Cell. *J. Phys. Chem. B* **1999**, *103* (42), 8940–8943.
8. Hu, L.; Peng, J.; Wang, W.; Xia, Z.; Yuan, J.; Lu, J.; Huang, X.; Ma, W.; Song, H.; Chen, W.; Cheng, Y.-B.; Tang, J. Sequential Deposition of CH3NH3PbI3 on Planar NiO Film for Efficient Planar Perovskite Solar Cells. *ACS Photonics* **2014**, *1* (7), 547–553.
9. Yu, M.; Natu, G.; Ji, Z.; Wu, Y. P-Type Dye-Sensitized Solar Cells Based on Delafossite $CuGaO_2$ Nanoplates with Saturation Photovoltages Exceeding 460 MV. *J. Phys. Chem. Lett.* **2012**, *3* (9), 1074–1078.
10. Zhang, H.; Wang, H.; Chen, W.; Jen, A. K.-Y. CuGaO2: A Promising Inorganic Hole-Transporting Material for Highly Efficient and Stable Perovskite Solar Cells. *Adv. Mater.* **2017**, *29* (8), 1604984.
11. Powar, S.; Xiong, D.; Daeneke, T.; Ma, M. T.; Gupta, A.; Lee, G.; Makuta, S.; Tachibana, Y.; Chen, W.; Spiccia, L.; Cheng, Y.-B.; Götz, G.; Bäuerle, P.; Bach, U. Improved Photovoltages for P-Type Dye-Sensitized Solar Cells Using $CuCrO_2$ Nanoparticles. *J. Phys. Chem. C* **2014**, *118* (30), 16375–16379.
12. Hagfeldt, A.; Boschloo, G.; Sun, L.; Kloo, L.; Pettersson, H. Dye-Sensitized Solar Cells. *Chem. Rev.* **2010**, 110, 11, 6595–6663.
13. O'Regan, B.; Grätzel, M. A Low-Cost, High-Efficiency Solar Cell Based on Dye-Sensitized Colloidal $TiO_2$ Films. *Nature* **1991**, *353* (6346), 737–740.
14. Yu, M.; Draskovic, T. I.; Wu, Y. Cu(I)-Based Delafossite Compounds as Photocathodes in p-Type Dye-Sensitized Solar Cells. *Phys. Chem. Chem. Phys.* **2014**, *16* (11), 5026–5033.
15. Xu, Z.; Xiong, D.; Wang, H.; Zhang, W.; Zeng, X.; Ming, L.; Chen, W.; Xu, X.; Cui, J.; Wang, M.; Powar, S.; Bach, U.; Cheng, Y.-B. Remarkable Photocurrent of P-Type Dye-Sensitized Solar Cell Achieved by Size Controlled $CuGaO_2$ Nanoplates. *J. Mater. Chem. A* **2014**, *2* (9), 2968–2976.
16. Odobel, F.; Pellegrin, Y. Recent Advances in the Sensitization of Wide-Band-Gap Nanostructured p-Type Semiconductors. Photovoltaic and Photocatalytic Applications. *J. Phys. Chem. Lett.* **2013**, *4* (15), 2551–2564.

17. Creissen, C. E.; Warnan, J.; Reisner, E. Solar $H_2$ Generation in Water with a $CuCrO_2$ Photocathode Modified with an Organic Dye and Molecular Ni Catalyst. *Chem. Sci.* **2018**, *9* (6), 1439–1447.
18. Wang, J.; Ibarra, V.; Barrera, D.; Xu, L.; Lee, Y.-J.; Hsu, J. W. P. Solution Synthesized P-Type Copper Gallium Oxide Nanoplates as Hole Transport Layer for Organic Photovoltaic Devices. *J. Phys. Chem. Lett.* **2015**, *6* (6), 1071–1075.
19. Wang, J.; Lee, Y.-J.; Hsu, J. W. P. Sub-10 Nm Copper Chromium Oxide Nanocrystals as a Solution Processed p-Type Hole Transport Layer for Organic Photovoltaics. *J. Mater. Chem. C* **2016**, *4* (16), 3607–3613.
20. Ueda, K.; Hase, T.; Yanagi, H.; Kawazoe, H.; Hosono, H.; Ohta, H.; Orita, M.; Hirano, M. Epitaxial Growth of Transparent P-Type Conducting CuGaO2 Thin Films on Sapphire (001) Substrates by Pulsed Laser Deposition. *J. Appl. Phys.* **2001**, *89* (3), 1790–1793.
21. Tate, J.; Ju, H. L.; Moon, J. C.; Zakutayev, A.; Richard, A. P.; Russell, J.; McIntyre, D. H. Origin of p-Type Conduction in Single-Crystal $CuAlO_2$. *Phys. Rev. B* **2009**, *80* (16), 165206.
22. Hautier, G.; Miglio, A.; Ceder, G.; Rignanese, G.-M.; Gonze, X. Identification and Design Principles of Low Hole Effective Mass P-Type Transparent Conducting Oxides. *Nat. Commun.* **2013**, *4* (1), 2292.
23. Gillen, R.; Robertson, J. Band Structure Calculations of $CuAlO_2$, $CuGaO_2$, $CuInO_2$, and $CuCrO_2$ by Screened Exchange. *Phys. Rev. B* **2011**, *84* (3), 035125.
24. Benko, F. A.; Koffyberg, F. P. Preparation and Opto-Electronic Properties of Semiconducting $CuCrO_2$. *Mater. Res. Bull.* **1986**, *21* (6), 753–757.
25. Benko, F. A.; Koffyberg, F. P. The Optical Interband Transitions of the Semiconductor $CuGaO_2$. *Phys. Status Solidi A* **1986**, *94* (1), 231–234.
26. Bredar, A. R. C.; Blanchet, M. D.; Comes, R. B.; Farnum, B. H. Evidence and Influence of Copper Vacancies in P-Type $CuGaO_2$ Mesoporous Films. *ACS Appl. Energy Mater.* **2019**, *2* (1), 19–28.
27. Flynn, C. J.; McCullough, S. M.; Oh, E.; Li, L.; Mercado, C. C.; Farnum, B. H.; Li, W.; Donley, C. L.; You, W.; Nozik, A. J.; McBride, J. R.; Meyer, T. J.; Kanai, Y.; Cahoon, J. F. Site-Selective Passivation of Defects in NiO Solar Photocathodes by Targeted Atomic Deposition. *ACS Appl. Mater. Interfaces* **2016**, *8* (7), 4754–4761.
28. Flynn, C. J.; McCullough, S. M.; Li, L.; Donley, C. L.; Kanai, Y.; Cahoon, J. F. Passivation of Nickel Vacancy Defects in Nickel Oxide Solar Cells by Targeted Atomic Deposition of Boron. *J. Phys. Chem. C* **2016**, *120* (30), 16568–16576.
29. Tian, L.; Tyburski, R.; Wen, C.; Sun, R.; Abdellah, M.; Huang, J.; D’Amario, L.; Boschloo, G.; Hammarström, L.; Tian, H. Understanding the Role of Surface States on Mesoporous NiO Films. *J. Am. Chem. Soc.* **2020**, *142* (43), 18668–18678.
30. Chown, A. L.; Farnum, B. H. Defining the Role of $Cr^{3+}$ as a Reductant in the Hydrothermal Synthesis of CuCrO2 Delafossite. *Inorg. Chem.* **2022**, *61* (21), 8349–8355.
31. Bredar, A. R. C.; Blanchet, M. D.; Comes, R. B.; Farnum, B. H. Evidence and Influence of Copper Vacancies in P-Type CuGaO2 Mesoporous Films. *ACS Appl. Energy Mater.* **2019**, *2* (1), 19–28.
32. Bredar, A. Synthesis and Electrochemical Characterization of Ternary Metal Oxides. PhD Dissertation, Department of Chemistry and Biochemistry, Auburn University, Auburn AL. **2021**.

33. Zhao, R.-D.; Zhang, Y.-M.; Liu, Q.-L.; Zhao, Z.-Y. Effects of the Preparation Process on the Photocatalytic Performance of Delafossite $CuCrO_2$. *Inorg. Chem.* **2020**, *59* (22), 16679–16689.
34. Greiner, M. T.; Chai, L.; Helander, M. G.; Tang, W.-M.; Lu, Z.-H. Transition Metal Oxide Work Functions: The Influence of Cation Oxidation State and Oxygen Vacancies. *Adv. Funct. Mater.* **2012**, *22* (21), 4557–4568.
35. Natu, G.; Hasin, P.; Huang, Z.; Ji, Z.; He, M.; Wu, Y. Valence Band-Edge Engineering of Nickel Oxide Nanoparticles via Cobalt Doping for Application in p-Type Dye-Sensitized Solar Cells. *ACS Appl. Mater. Interfaces* **2012**, *4* (11), 5922–5929.
36. Enright, B.; Redmond, G.; Fitzmaurice, D. Spectroscopic Determination of Flatband Potentials for Polycrystalline TiO2 Electrodes in Mixed Solvent Systems. *J. Phys. Chem.* **1994**, *98* (24), 6195–6200.
37. Redmond, G.; Fitzmaurice, D. Spectroscopic Determination of Flatband Potentials for Polycrystalline Titania Electrodes in Nonaqueous Solvents. *J. Phys. Chem.* **1993**, *97* (7), 1426–1430.
38. Rothenberger, G.; Fitzmaurice, D.; Graetzel, M. Spectroscopy of Conduction Band Electrons in Transparent Metal Oxide Semiconductor Films: Optical Determination of the Flatband Potential of Colloidal Titanium Dioxide Films. *J. Phys. Chem.* **1992**, *96* (14), 5983–5986.
39. Park, N. G.; Jang, S. H.; Kim, G. J. Effect of Cations on the Open-Circuit Photovoltage and the Charge-Injection Efficiency of Dye-Sensitized Nanocrystalline Rutile $TiO_2$ Films. *Bull. Korean Chem. Soc.* **2000**, *21* (10), 1047–1048.
40. Wu, S.; Han, H.; Tai, Q.; Zhang, J.; Xu, S.; Zhou, C.; Yang, Y.; Hu, H.; Chen, B.; Sebo, B.; Zhao, X.-Z. Enhancement in Dye-Sensitized Solar Cells Based on MgO-Coated $TiO_2$ electrodes by Reactive DC Magnetron Sputtering. *Nanotechnology* **2008**, *19* (21), 215704.
41. McCullough, S. M.; Evans, J. M.; Moot, T.; Taggart, A. D.; Troian-Gautier, L.; Cahoon, J. F. Cation Effects in P-Type Dye-Sensitized Solar Cells. *ACS Appl. Energy Mater.* **2020**, *3* (2), 1496–1505.
42. Dunwell, M.; Yan, Y.; Xu, B. Understanding the Influence of the Electrochemical Double-Layer on Heterogeneous Electrochemical Reactions. *Curr. Opin. Chem. Eng.* **2018**, *20*, 151–158.
43. Kelly, C. A.; Farzad, F.; Thompson, D. W.; Stipkala, J. M.; Meyer, G. J. Cation-Controlled Interfacial Charge Injection in Sensitized Nanocrystalline $TiO_2$. *Langmuir* **1999**, *15* (20), 7047–7054.
44. Song, W.; Luo, H.; Hanson, K.; Concepcion, J. J.; Brennaman, M. K.; Meyer, T. J. Visualization of Cation Diffusion at the $TiO_2$ Interface in Dye Sensitized Photoelectrosynthesis Cells (DSPEC). *Energy Environ. Sci.* **2013**, *6* (4), 1240–1248.
45. Xie, J.; Lu, Y.-C. A Retrospective on Lithium-Ion Batteries. *Nat. Commun.* **2020**, *11* (1), 2499.

# Chapter 5

## Summary and Outlook

### *5.1 Introduction*

This chapter discusses future research directions to ultimately enhance the electrochemical performance and stability of $CuCrO_2$. Previous experiments and conclusions from ***Chapters 3-4***, in addition to recent preliminary findings, aid in supporting novel experiments discussed in ***Sections 5.2-5.6***. Such experiments include but are not limited to studying the morphological growth of $CuCrO_2$ in efforts to increase the isotropic nature of the nanocrystals, doping $CuCrO_2$ and studying the degradative effects, and exploring alternative cation sources in electrolyte solution.

### *5.2 Morphological Studies*

The synthesis of $CuCrO_2$ has been optimized as detailed in ***Chapter 3*** as nanocrystalline particles with an aspect ratio of 4.6 ± 1.9. Compared to its larger counterpart $CuGaO_2$ discussed briefly in ***Chapter 4***, whose morphology resembles hexagonal plates with a width upwards of 400 nm and an aspect ratio approximately twice the size of $CuCrO_2$, it was shown that the electrochemical performance of $CuCrO_2$ was better than $CuGaO_2$ due to the particles being smaller, having a more isotropic nature with the Cu-terminated faces being more exposed and more accepting of electrochemical reactivity with $Li^+$ in solution. This suggests that delafossite materials that are small and isotropic in nature could lead to better functionality as a hole transport material for solar cell applications.

In future efforts to continue the improvement of electrochemical performance by $CuCrO_2$, while the particles are currently synthesized on the nanoscale, additional synthetic routes to growing $CuCrO_2$ can be explored with the introduction of capping ligands as a reactant to facilitate the morphological growth of nanoparticles with improved electrochemical performance. This could enable an aspect ratio closer to 1, or an aspect ratio > 1 in favor of growth along Cu-terminated planes which could improve the availability of Cu-terminated faces. The approach of $CuCrO_2$ growth exposing a single crystal facet has been executed previously using an oxygen plasma assisted molecular beam epitaxy (MBE) deposition method,[1] but proposing hydrothermal synthetic procedures would be optimal due to its ease of experimental design, while MBE deposition requires more time and high temperatures which can become cumbersome.

In previous studies, organic capping ligands have been utilized to influence the morphological growth of nanomaterials using a variety of ligands; however, the appropriate ligand needs to be selected in order to achieve definitive, reproducible control of the synthesis and the resulting dimensions of the particles. Ligands that have been explored and utilized as capping agents include but are not limited to alkylphosphonic acid ligands, oleyl alcohol solutions, amines, and carboxylic acids.[2–7] In the case of utilizing a capping agent to control the growth of $CuCrO_2$, an agent must be selected that promote capping along Cu-terminated surfaces. This would allow for more vertical growth in which more Cu-terminated faces are available for redox activity.

Capping agents with hydroxyl groups would be a possible candidate for controlling the morphological growth of $CuCrO_2$ due to the strong affinity -OH groups have toward transition metals. Glycerol has been previously used as a capping agent in the growth of rhombohedral, spherical-like $CuFeO_2$ nanoparticles due to the tridentate -OH functional groups present in the structure.[8] A similar approach could be used to synthesize $CuCrO_2$ nanoparticles with a more isotropic morphology.

It is important to note that the presence of such capping agents could be counterintuitive, acting as a reducing agent in the synthesis of the delafossite structure. For example, ethylene glycol (a commonly used capping agent) had been introduced to the synthesis as seen in ***Chapter 3***. This ultimately led to over-reduction of $Cu^{2+}$ to $Cu^0$ metal and prevented the growth of delafossite $CuCrO_2$. Furthermore, a two-step synthetic procedure could be explored where the hydrothermal synthesis is allowed to proceed without the capping agent for long enough to permit the formation of reduced $Cu^+$ and $Cr^{3+}$ oxides, followed by the addition of a small amount of the capping agent. The hydrothermal synthesis could then proceed for the remainder of the required 60 hours to permit layering of the oxides to form the delafossite structure with preferential morphological growth.

A series of times for steps 1 and 2 would need to be conducted, in addition to a synthetic procedure where the reaction proceeds for the full 60 hours in the presence of the capping agent, in order to compare results and to determine if this method is viable. Adjusting the amount of capping agent added to the reaction can also aid in determining whether or not there is a "sweet spot" in which adding too little is not effective, while adding excess results in unwanted side products due to more favorable over-reduction to $Cu^0$. In the case of $CuFeO_2$, over-reduction of Cu was not discussed as an issue. Following their experimental procedure in which 2 mL glycerol and 20 mmol total reactants are added in 40 mL water and NaOH solution as the base source may be a good starting point.[8]

Using a capping agent that is less prone to oxidation is an alternate route that could be explored in the morphological control of $CuCrO_2$ growth. Silica nanoparticles might be a good candidate as a capping agent due to its chemical inertness, transparency, high colloidal stability, and dispersibility.[9] This could allow for silica to coat the surface of $CuCrO_2$ without affecting the capability for redox reactions to occur at the surface of the $CuCrO_2$ cores and preventing reduction of $Cu^+$ to $Cu^0$ metal.

### *5.3 Monovalent Cation Defect Studies*

#### *5.3.1. Cationic Vacancies in $CuCrO_2$*

Cation-deficient metal oxides are of interest due to previously seen correlations between inducing cationic vacancies, improved diffusion of lithium within the structure, and enhanced conductivity and capacitance of the material.[10–13] While the role vacancies have on performance in metal oxides has been established in the literature, the control of vacancy concentration in metal oxides and the stabilization of such vacancies has only been attained for select metal oxides. The introduction of vacancies has usually been done synthetically, including oxidative electrodeposition at high current density[14] where an electric current is applied to a conductive material in a solution, typically a salt, to reduce dissolved metal cations to form a metal coating on the electrode. Vacancies may be introduced via electrodeposition through excess vacancy reduction when high current is applied. Additionally, high temperature heating in defect-inducing environments, specifically heating under $O_2$ or $H_2O$, has been used to synthetically introduce vacancies.[15]

Research on inducing vacancies in delafossite $CuCrO_2$ and studying effects on its properties is scarce. The control of defects has been done using glovebox reduction methods;[11] however, this can become cumbersome.[12] Additionally, research has been done to control defects in delafossite $CuCrO_2$ by controlled annealing,[16] the annealing temperatures which are claimed to influence the vacancy concentrations are upwards of 900 ˚C. Chemical reactions to form spinel $CuCr_2O_4$ have been noted in literature at temperatures above 400 ˚C depending on atmospheric conditions[17], which would support the idea that spinel formation at extreme annealing temperatures could influence differences in properties but may pose difficulties with respect to preventing decomposition under non-inert atmospheric conditions.

***Section 5.3.3.2*** extensively discusses the role of pH dependence of delafossite $CuCrO_2$ to introduce and control cationic vacancies through acidic washing methods, ideal for its simplistic methodology and ease of reproducibility. Based on the results discussed, washing $CuCrO_2$ powder in pH 1 solution for 96 hours is the optimal condition to induce the maximum amount of $Cu^+$ vacancies while maintaining crystallinity. Washing the powder for less time results in less vacancies induced, which allows for tunability. Conversely, washing for longer than 96 hours negatively impacts the electrochemistry of the resulting material and is likely caused by excess vacancies, leading to a loss in crystallinity.

Several additional pH dependence studies can be implemented to ultimately control the vacancy concentrations in the material, and to study its effects on the morphology changes of $CuCrO_2$ from nanocrystalline to amorphous which could be a driving force behind the observed electrochemical behavior. ***Section 5.3.2*** goes into more detail on proposed pH dependence studies to further control vacancy concentrations in $CuCrO_2$.

### *5.3.2 Possible Deleterious Impacts of $Cu^{II}$ Sites*

Delafossite $CuCrO_2$ shows considerable degradation upon exposure to extreme potentials and multiple cycling, revealed in ***Chapter 4*** through multiple cycling CV experiments as well as analyzing the electrolyte solution after applying an extreme positive potential over time. This degradative behavior is not ideal because it leads to difficult analysis of electrochemical studies which require relatively long-term electrochemical exposure such as EIS. Additionally, performance as a cathode in ion batteries has severe limitations due to the significant decrease in performance over time, as seen by the charge capacities calculated from multiple charge-discharge cycling experiments.

It is plausible that the presence of $Cu^{2+}$ sites could be facilitating the degradation of the film; $Cu^{2+}$ prefers square planar coordination due to its $d^9$ electron configuration and Jahn-Teller distortion. However, as previously seen by XPS data in ***Chapter 4*** when $Cu^+$ vacancies are present in $CuCrO_2$, adjacent $Cu^{2+}$ atoms are present for charge compensating purposes. These $Cu^{2+}$ atoms remain in linearly coordinated sites, which increases the steric strain of the overall system and could lead to advanced degradation. If $CuCrO_2$ could be synthesized with $Cu^+$ vacancies while simultaneously preventing the oxidation of neighboring copper sites to $Cu^{2+}$, the steric strain could be minimized and the rate of degradation may improve. It is important to note that this strategy would simply decrease the concentration of $Cu^{2+}$ adjacent to vacancies; as seen in ***chapter 4***, $Cu^{2+/+}$ redox events permit the electrochemical processes observed by $CuCrO_2$. This could slow the rate of degradation, but in order to alleviate the film of $Cu^{2+}$ sites altogether, $Cu^+$ defects must be absent in order to prevent $Cu^{2+}$ compensation and $Cr^{3+}$ must be involved in the redox event.

Synthetically doping $CuCrO_2$ has been previously explored through doping $Mg^{2+}$, $Sc^{3+}$, $Rh^{3+}$, and $Ti^{4+}$ to study the resulting electrochemical properties.[18–21] Manickam et al. was interested in doping $CuCrO_2$ for potential supercapacitor applications, and concluded that by doping with $Mg^{2+}$ and $Ti^{4+}$ simultaneously, the reversibility of the resulting CV improved over time.[21] A similar approach could be used in which $Ti^{4+}$ could be doped in place of $Cr^{3+}$ sites to charge balance existing $Cu^+$ vacancies, thus eliminating the need for neighboring $Cu^{2+}$ sites. Manickam et al. assigned CV features to a $Cu^{2+/+}$ redox event, implying $Ti^{4+}$ was not redox active. In our case, $Ti^{4+}$

would be expected to charge compensate for $Cu^+$ vacancies, but the presence of $Li^+$ would still drive $Cu^{2+/+}$ redox events. Nonetheless, reducing the initial concentration of $Cu^{2+}$ on the surface can improve degradation due to steric strain. If such reduction in steric strain reduces the degradation of the film over periods of electrochemical exposure, and if the cycling efficiency improves, there is potential for the number of $Cu^+$ vacancies to be increased and for enhanced lithiation of the film, making these materials more viable for ion battery applications.

### *5.3.3 pH Dependence Studies*

#### *5.3.3.1 Paste Fabrication and the Role of pH*

For all previously discussed experiments, a pH neutral paste was made in efforts to fabricate thin films using ethanol and ethyl cellulose. However, it would not be surprising that pastes prepared under acidic conditions may degrade the material in such a way that vacancy concentrations or morphology are also impacted. Preliminary studies comparing CVs in 0.1 M $LiClO_4$ in MeCN for two films of $CuCrO_2$ prepared different pastes in shown in **Figure 5.1**. Here, the pH neutral data (red) refers to a $CuCrO_2$ film prepared using a paste that had been developed as previously discussed in ***Chapter 4*** while the pH 1 data (blue) was prepared using a 2:1 ratio of $CuCrO_2$:PEG with 13 wt % of $CuCrO_2$ in a pH 1 solution made using HCl in water. Here, PEG refers to 20,000 $M_w$ polyethylene glycol.

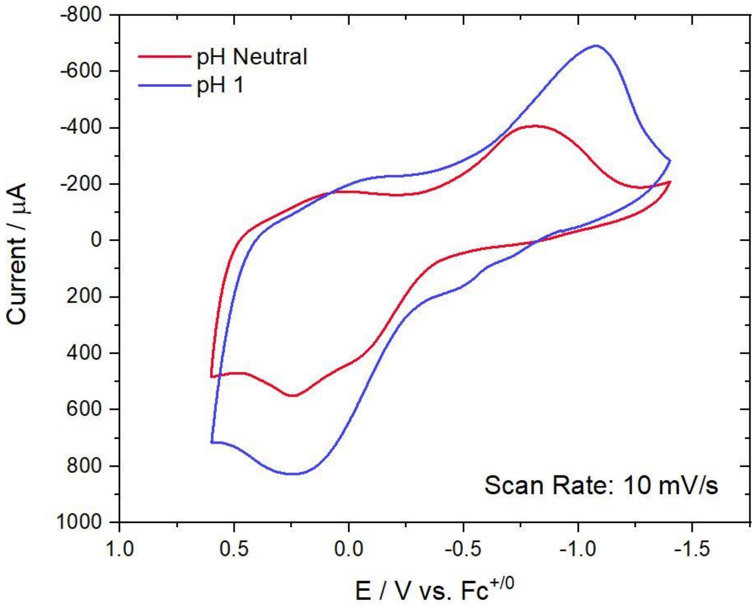

**Figure 5.1.** Cyclic voltammograms of films developed using a pH neutral paste vs pH 1 paste in 0.1 M $LiClO_4$ in MeCN at a 10 mV/s scan rate.

There is a considerable increase in the faradaic current measured by the film prepared using the pH 1 paste fabrication method; however, it is unclear if this is due to an increase in the $Cu^+$ vacancies present or an increase in film surface area. The use of PEG rather than ethyl cellulose could have resulted in larger pores post-annealing, resulting in electrochemical changes. While the surface area would be expected to decrease as a result of larger pores, the dye loading capability would improve and could be utilized to study $CuCrO_2$ films photoelectrochemically through the collection of J-V curves under illumination for solar cell applications. To understand and isolate both factors, subsequent experiments would need to be conducted in which pH 1 pastes were developed using PEG with a lower molecular weight, or a supplemental polymer, that is soluble in water and would produce films with comparable porosity relative to its pH neutral counterpart. This would aid in determining the degree of impact that both porosity and paste pH have on the electrochemical properties.

#### *5.3.3.2 Effects of Acidic Washing Environment on the Electrochemical Properties of $CuCrO_2$*

In the case of delafossite $CuCrO_2$, moderate conductivity values have been reported with a range from 157 to almost 436 mA h $g^{-1}$ as an anodic material.[22,23] While these are not cathodic measurements, the potential for $CuCrO_2$ to exceed the specific capacity of lithium nickel manganese cobalt oxide (NMC) as a cathode is definitely plausible, but no studies have reported specific capacities for $CuCrO_2$ as a cathodic material, nor have studies explored optimizing the synthesis of $CuCrO_2$ or film preparation to improve its performance for ion battery application.

Preliminary electrochemical studies were conducted to further understand how acid washing $CuCrO_2$ before thin film fabrication (in efforts to induce $Cu^+$ vacancies) influences the surface charge and charge-discharge capacities observed. As seen in ***chapter 4*** and in this section, a strong $Li^+$ dependence was observed, suggesting these materials have potential to be used as cathodic materials in ion battery application. Acid washing $CuCrO_2$ films for 12 – 336 hours was shown to lead to consistent increases in both surface charge and capacities compared to their base washed counterpart, with films made from $CuCrO_2$ washed for 96 hours lead to overall optimal electrochemical performance.

The synthetic procedure, paste development, and thin film fabrications used for these preliminary studies were identical to those described in the experimental section of ***Chapter 4***. However, after synthesis the solid product was washed in a pH 1 HCl (acidic) solution for a predetermined period of time rather than washing in basic solution for 24 hours. A series was conducted in which the wash times varied at 12, 24, 36, 48, 96, 168, and 336 hours. This permitted both cleaning the product from any possible impurities while also slowly etching the $CuCrO_2$ particles in efforts to induce more $Cu^+$ vacancies. The remaining product was rinsed with ethanol, sonicated, and vortexed three times to allow additional cleansing of remaining acidic solution before drying the product under a fume hood overnight. After drying under the fume hood, the product was placed in a vacuum oven (Lindberg Blue M) at 60 ˚C overnight to ensure complete dryness.

**Figure 5.2** shows cyclic voltammograms for $CuCrO_2$ thin films washed in acidic solution for 12 – 336 hours. All cyclic voltammograms were collected at a 10 mV/s scan rate in 0.1 M $LiClO_4$ in MeCN. The electrochemical features for all voltammograms are consistent with previous observations discussed in ***Chapter 4***. Namely, two quasi-reversible features are present, one with a narrow peak separation and $E_{1/2} = 0.14$ V and another with a broad peak separation and $E_{1/2} = -0.43$ V. Both of these features appeared to be influenced by $[Li^+]$ with the -0.43 V feature being assigned to Li-coupled redox event dependent on the concentration of copper vacancies in the delafossite lattice.

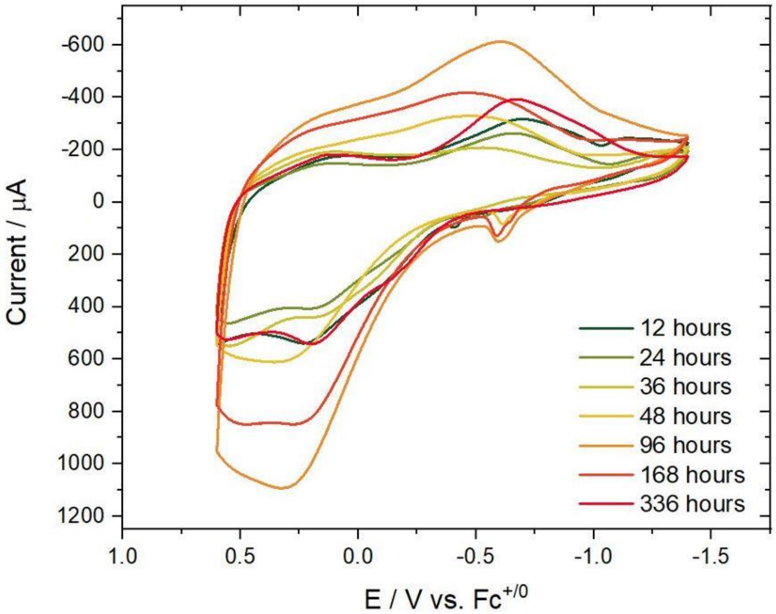

**Figure 5.2.** Cyclic voltammograms of $CuCrO_2$ thin films washed in acidic solution at various times for 12 – 336 hours. All CVs were collected in 0.1 M $LiClO_4$ in MeCN at a 10 mV/s scan rate.

Quantitatively, the amount of current passed fluctuates between the samples depending on the amount of time $CuCrO_2$ powder was washed in acidic solution. It is evident that between 12 and 96 hours of washing, peak anodic and cathodic currents increase with washing time. However, beyond 96 hours, peak currents decreased, resulting an optimal wash time of 96 hours in terms of maximum current.

To better understand this quantitative increase in current at 96 hours, chronoamperometry experiments were conducted for $CuCrO_2$ films with varying acidic wash times of 12 – 336 hours. Data was collected for all $CuCrO_2$ films in 3 steps for 100 seconds each. Step 1 was held at -1.3 V vs $Fc^{+/0}$, followed by step 2 at 0.3 V, and step 3 at -1.3 V again. Similar to chronoamperometry experiments discussed in ***Chapter 4***, these potentials were chosen to ensure a majority of the redox features could be captured without entering an extreme potential range that could facilitate degradation or an irreversible oxidation near 0.5 V, as has been previously seen. All amperometric IT curves can be seen in **Figure S5.1**; this data was then integrated to construct Anson plots as seen in **Figure 5.3a** for the anodic step to 0.3 V vs $Fc^{+/0}$. Linearity was observed at large $t^{1/2}$ and the resulting slopes were used to calculate diffusion coefficients in accordance with the Anson equation as previously seen in ***Chapter 4*** (**Equation 5.1**). Surface charge ($Q_{ads}$) was also quantified from the y-intercept of the linear fits. All diffusion coefficient and surface charge values are provided in **Table 5.1** with $Q_{ads}$ data summarized in **Figure 5.3b** for the anodic step at 0.3 V vs $Fc^{+/0}$. Anson plots with corresponding diffusion coefficient and surface charge values for the cathodic steps (steps 1 and 3) at -1.3 V vs $Fc^{+/0}$ can be found in **Figures S5.2-3** and **Tables S5.1-2**.

$$\mathrm{Q} = \mathrm{nFAC_oD_o^{1/2}t^{1/2}\pi^{-1/2}} + \mathrm{Q_{ads}} \qquad \textbf{eq. 5.1)}$$

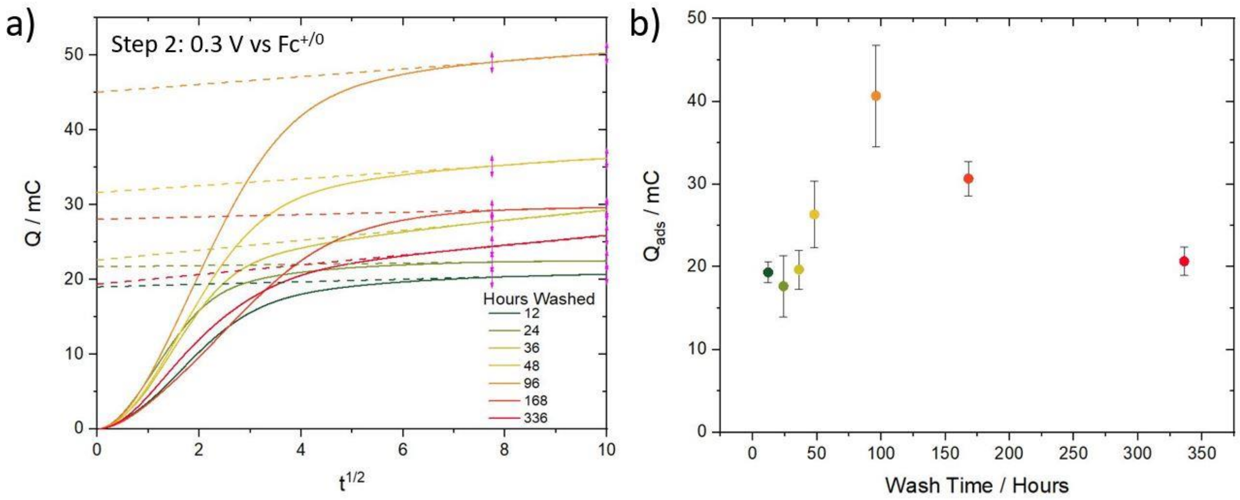

**Figure 5.3. a)** Anson plots constructed from integrated anodic chronoamperometry data using films fabricated from $CuCrO_2$ powders washed in acidic solution from 12 – 336 hours in 0.1 M $LiClO_4$ in MeCN. Each step was held at the fixed potential 0.3 V vs $Fc^{+/0}$ for 100 seconds. **b)** $Q_{ads}$ plotted as a function of wash time in acidic solution, with error bars from triplicate experiments for each condition.

**Table 5.1.** Diffusion coefficients and adsorption charges determined from Anson plot step 2 where the potential was held at 0.3 V vs $Fc^{+/0}$ for 100 seconds.

| Wash Time | Diffusion Coefficient / $cm^2s^{-1}$ | Adsorption Charge Q / mC |
|---|---|---|
| 12 | $8.3 \times 10^{-17}$ | 19 ± 1.3 |
| 24 | $1.9 \times 10^{-17}$ | 18 ± 3.7 |
| 36 | $1.3 \times 10^{-15}$ | 20 ± 2.4 |
| 48 | $6.0 \times 10^{-16}$ | 26 ± 4.0 |
| 96 | $7.7 \times 10^{-16}$ | 41 ± 6.1 |
| 168 | $7.0 \times 10^{-17}$ | 31 ± 2.1 |
| 336 | $1.2 \times 10^{-15}$ | 21 ± 1.7 |

The diffusion coefficients of the $CuCrO_2$ films calculated from the slopes are comparable to those seen from base washed $CuCrO_2$ films in ***Chapter 4***, which again suggests a pseudo-capacitive redox reaction at the nanocrystalline interface. However, the surface charge ($Q_{ads}$) observed for the acidic washed films are substantially higher at all wash times than those seen from base washed $CuCrO_2$ where $Q_{ads}$ = 12 ± 2.2 mC in 0.1M $LiClO_4$ for the base washed film. Among the acid washed films, $CuCrO_2$ washed for 96 hours had the highest surface charge at $Q_{ads}$ = 41 ± 6.1 mC. Similar trends observed in CV were observed in surface charges; $Q_{ads}$ maximized at 96 hours and decreased for longer washing times. When considering surface charge should be proportional to the number of copper vacancies, the significant increase in surface charge under acidic wash conditions supports the idea that $Cu^+$ atoms can be etched away from the $CuCrO_2$ surface leading to an increase in vacancies. Surface charge $Q_{ads}$ calculated from **Equation 5.1** were also used for $CuCrO_2$ after washing to calculate the theoretical % $Cu^+$ vacancies present based on the charge capacity of the material after one charge-discharge cycle assuming the redox reaction shown in **Equation 5.2** (**Table 5.2**). The theoretical % $Cu^+$ vacancies calculated support the idea that acidic washing consistently leads to an increase in vacancies compared to the base washed films seen in ***Chapter 4***.

$$Cu^{+}_{1-2x}Cu^{2+}_{x}V_{Cu,x}Cr^{3+}O_2 + xLi^+ + xe^- \rightarrow Cu^{+}_{1-x}Li^{+}_{x}Cr^{3+}O_2 \qquad \textbf{eq. 5.2)}$$

**Table 5.2.** Theoretical % $Cu^+$ Vacancies based on surface charge ($Q_{ads}$) of $CuCrO_2$ films after charge cycle 2.

| Time Washed (Hours) | Step 2 Charge $Q_{ads}$ (mC) | Theoretical % $Cu^+$ Vacancies |
|---|---|---|
| 12 | 19 | 10 |
| 24 | 18 | 9.5 |
| 36 | 20 | 10.5 |
| 48 | 26 | 13.5 |
| 96 | 41 | 21 |
| 168 | 31 | 16 |
| 336 | 21 | 11 |

Based on these results, ICP-MS can be done to determine the Cr:Cu ratio of the powders after acid washing to compare to the theoretical % $Cu^+$ vacancies. If the surface charge observed by chronoamperometry is higher than theoretically calculated, the excess surface charge could be accounted for by $Li^+$ intercalation. The degree of intercalation would be determinate on whether or not enough vacancies have been induced to permit lithiation into the lattice.

It is important to note that based on the surface charges calculated from Anson plots that films made using $CuCrO_2$ powder washed for 96 hours resulted in the highest $Q_{ads}$ at 41 mC. This however does not mean that $CuCrO_2$ powders washed for longer would result in less vacancies. The loss in surface charge and overall performance may be attributed to the induction of too many $Cu^+$ vacancies, and could result in a loss of crystallinity which could degrade $Li^+$ surface interaction or hinder any intercalation capabilities of $Li^+$.

Chronopotentiometry experiments were conducted for films made with $CuCrO_2$ washed for 12 – 336 hours to calculate both charge and discharge capacities as well as to study the degradation of the film in the form of % cycling efficiencies. All chronopotentiograms can be referenced in **Figure 5.4a-g**. Each chronopotentiometry experiment was done in 0.1 M $LiClO_4$ in MeCN from 0.6 to -1.4 V vs $Fc^{+/0}$ while holding 0.1 mA current. Cycles are shown in gradient from cycle 2 (green) to cycle 10 (red). All calculated results from these experiments are shown in **Tables S5.3-13**.

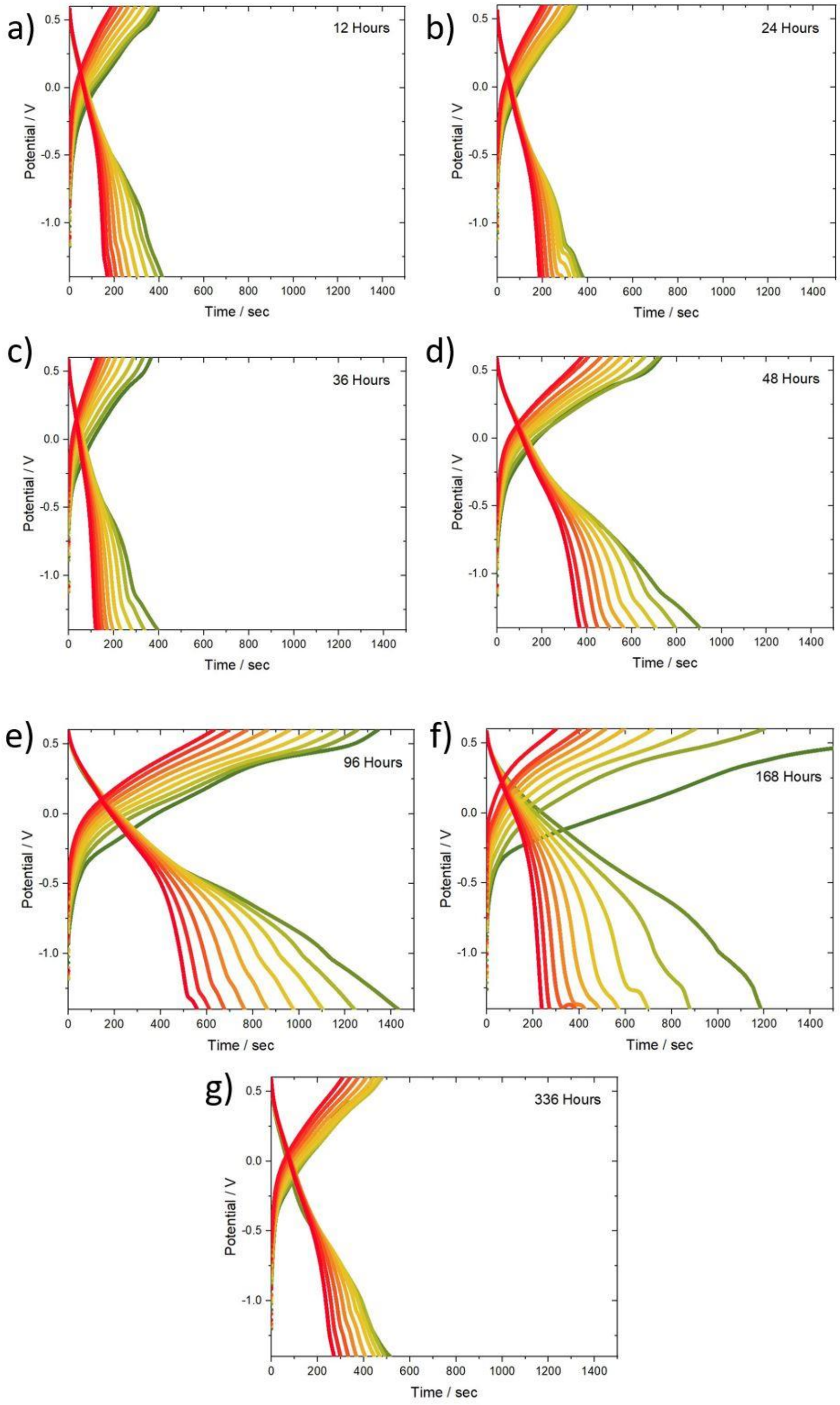

**Figure 5.4**. Chronopotentiograms of films made using $CuCrO_2$ powders with acidic wash times **a)** 12 hours, **b)** 24 hours, **c)** 36 hours, **d)** 48 hours, **e)** 96 hours, **f)** 168 hours, and **g)** 336 hours.

Similar to CV and chronoamperometry results, charge storage was found to be optimal for the films in which $CuCrO_2$ was washed in acidic solution for 96 hours with a 134 mC charge and 70 mA h $g^{-1}$ charge capacity after cycle 2, and all acidic washed $CuCrO_2$ films exhibited higher charge storage than base washed $CuCrO_2$ films reported in ***Chapter 4***. Interestingly, 168 hour washed $CuCrO_2$ films saw a charge of 205 mC and charge capacity of 106 mA h $g^{-1}$ after charge cycle 2. However, the % cycling efficiency was the lowest of all wash conditions at 58% after charge cycle 2. While the cycling efficiency gradually increased to 80% by cycle 10, all other conditions maintained > 90% efficiency throughout cycling and close to 90% efficiency by cycle 10. One possibility is that at a 168 hours wash time, the film is etched and exposed to acid for such a long period of time that surface defects become too prominent and stability of the film at long exposure times to positive potentials decreases, resulting in the significant decrease in charge capacity upon initial cycling and poor % cycling efficiency. By 336 hours, the film may lose even more stability from acid exposure and overall performance could decrease as a result.

Conclusively, preparation of films using $CuCrO_2$ that has been acid washed consistently showed higher current seen in CV, surface charge ($Q_{ads}$), and charge capacities compared to base washed $CuCrO_2$ which was discussed in ***Chapter 4***. When compared to the optimal wash time of 96 hours in acidic solution, this performance enhancement is even more significant, with surface charge $Q_{ads}$ = 12 mC for base washed $CuCrO_2$ vs 41 mC for acid washed $CuCrO_2$ films, and charge capacity 7.8 mA h $g^{-1}$ for base washed $CuCrO_2$ vs 70 mA h $g^{-1}$ for acid washed $CuCrO_2$ after the $2^{nd}$ charge cycle.

While acid washed $CuCrO_2$ leads to film fabrication with higher performance compared to its base washed counterpart, and while at 96 hours the electrochemical performance is ideal, more experiments and characterization are required to determine the causes that lead to the trends described through this section. Triplicate measurements were taken for chronoamperometry experiments which resulted in error bars that support the trend that as time washed deviates from 96 hours, the surface charge observed decreases. More chronopotentiometry experiments can be taken in efforts to implement error bars for charge capacities as well.

ICP-MS studies might reveal that acid washed films have higher Cr:Cu ratios than what is seen in base washed films, where base washed films have 4% $Cu^+$ vacancies. Based on electrochemical characterization, 21% $Cu^+$ vacancies were expected to be observed in the $CuCrO_2$ powder washed for 96 hours in acidic solution. One possibility is that at 96 hours, an optimal amount of $Cu^+$ vacancies have been induced to maintain crystallinity and promote $Li^+$ intercalation into the lattice, resulting in high surface charge and charge capacity. At lower wash times, $CuCrO_2$ may become amorphous in nature or lose crystallinity due to severe etching of $Cu^+$ from the lattice. Another possibility could be that $Cr^{3+}$ is also etched from $CuCrO_2$ in addition to $Cu^+$, which could induce more vacancies while maintaining consistent Cr:Cu ratios. UV-vis can be used to further analyze whether or not $Cr^{3+}$ is also being etched from $CuCrO_2$ powder. In this case, if $CuCrO_2$ is washed for 96 hours, an optimal amount of vacancies may be induced to promote high electrochemical performance and $Cr^{3+}$ vacancies may lead to exposed $Cu^+$ vacancies underneath that are accessible to $Li^+$ interaction.

TEM and SAED of $CuCrO_2$ powders washed in acidic solution for 12 – 336 hours will ultimately give insight into whether or not the degree of crystallinity is affected by time washed in acidic solution by analyzing possible defects in the lattice. After TEM is collected for all samples, explanation for the observed electrochemical trends might be re-examined and further research can be explored in the upcoming year.

### *5.3.4 Effects of Synthetic Lithiation*

As seen in ***Chapter 4***, “electrochemical lithiation” is possible using 0.1 M $LiClO_4$ in MeCN as the electrolyte solution which ultimately increases the charge capacity of $CuCrO_2$. While electrochemical lithiation is of interest, synthetically doping transition metal oxides is also relevant. Previous studies involving synthetic lithiation of metal oxides reveals optimization of the interfacial charge transfer kinetics is necessary.[24] Computational studies have also revealed competition between two mechanisms, one involving a reversible intercalation reaction mechanism where lithium can intercalate in and out of the structure without structural distortion. The other mechanism involves an irreversible conversion mechanism where lithium intercalation induces a structural distortion.[25] These irreversible conversion mechanisms may be considered similar to what is discussed in ***Chapter 4*** and ***Section 5.3.3.2*** in which the structure degrades over the course of multiple cycling experiments. Based on chronopotentiometry experiments, cycling efficiency between charging and discharging was not efficient using base washed $CuCrO_2$ powder (***Chapter 4***) which could indicate less facile $Li^+$ movement through vacancies. One possibility for this might be that $Li^+$ can intercalate into $Cu^+$ vacant sites but get constrained and cannot as easily deintercalate. The acid washed $CuCrO_2$ powder (***Section 5.3.3.2***) produced improved cycling efficiencies. This may be due to the increased $Cu^+$ vacancy sites, allowing for more interstitial sites for $Li^+$ interaction and reduced difficulty for delithiation.

By synthetically lithiating delafossite $CuCrO_2$, structural characterization can be done to determine whether lithium would reside in interstitial sites, or if lithium would be in sites where copper vacancies are present to compensate for cationic deficiency in the material. Furthermore, a relationship may be observed between the concentration of cationic vacancies induced and the concentration of lithium doped into the structure. By determining where doped lithium atoms reside, as well as determining whether structural distortion occurs as a result of synthetic lithiation, electrochemically lithiating the material may present insight into the limits of lithium diffusion. Structural distortion caused by synthetically doping $CuCrO_2$ may lead to enhanced or impeded lithiation electrochemically. For instance, consider a hypothetical case where synthetically lithiated $CuCrO_2$ can maintain crystalline properties due to lithium atoms residing in cationic sites where copper is absent. Upon electrochemically lithiating the system, the rate of diffusion may increase and more lithium ions may intercalate into the system due to the material's crystallinity and preserved interstitial channels, as well as having wider interstitial channels due to lithium's smaller atomic radii. Synthetically lithiating $CuCrO_2$ with a range of cationic vacancy concentrations may reveal interesting correlations between lithiation approaches, structural integrity, rates of diffusion, and charge transfer kinetics.

ICP, TEM, and pXRD can be used to confirm both morphology and elemental composition, allowing trends in vacancy concentrations, paste pH, or doping conditions to be determined as further research is conducted. Ultimately, the goal is to be confident in determining what synthetic parameters and paste development conditions are necessary to produce $CuCrO_2$ controllably with a wide range of desired vacancy concentrations. Determination of such optimal parameters can be used to produce high-performing and electrochemically stable $CuCrO_2$ for either battery or solar cell applications.

### *5.4 Surface Chemistry and Optical Properties*

Previous studies reveal monovalent cation vacancies in transition metal oxides containing copper results in neighboring $Cu^{2+}$ atoms for charge compensation.[26] Additionally, $Cr^{4+}/Cr^{3+}$ coupling has been observed in transition metal oxides during lithium intercalation.[27] Based on our

XPS studies discussed in ***Chapter 4***, $Cr^{4+}/Cr^{3+}$ redox events are not taking place to account for $Li^+$ interactions, but rather $Cu^{2+}/Cu^+$ redox events. Because these interactions are surface-based, modifications to the film's surface may hinder or facilitate electrochemical processes.

One method to alter the surface chemistry of $CuCrO_2$ films could be to adjust the annealing conditions used, both in terms of temperature and gas conditions. Bredar et al. studied various annealing conditions of $CuGaO_2$ thin films using ATR-IR, and found that vibrational modes associated with polymer disappear at temperatures above 200 ˚C.[26] Annealing delafossite films at temperatures greater than 500 ˚C has also been found to lead to the conversion to delafossite into the spinel $CuM_2O_4$ phase.[28,29] All $CuCrO_2$ films that were previously discussed were annealed at 350 ˚C for 30 minutes to ensure the polymer is absent from the film post-annealing, in addition to the avoidance of spinel conversion. However, studying the effects of annealing at various temperature and time profiles between 200 and 500 ˚C may affect sintering of the nanoparticles. ***Chapter 4*** discusses the differences between $CuCrO_2$ and $CuGaO_2$ electrochemistry and how morphological differences play a role; $CuCrO_2$ was more isotropic in nature which led to more Cu-terminated faces to be available for $Li^+$ interaction. In the case of $CuGaO_2$, the large anisotropic particles post-annealing led to a preferential (001) stacking parallel to the FTO glass substrate which could have also played a role in reduced current observed in the CV in the presence of $Li^+$. While $CuCrO_2$ particles are more isotropic in nature compared to its $CuGaO_2$ counterpart, the aspect ratio is still $4.6 \pm 1.9$. This could lead to more enhanced sintering at higher temperatures or longer times in a preferential orientation which could directly affect the electrochemical properties of the film.

In addition to varying the annealing temperature and time, the gaseous environment in which the films are annealed can lead to interesting surface state changes. Preliminary findings have shown the $V_{OC}$ of $CuCrO_2$ thin films annealed at 350 ˚C under argon for 30 minutes is approximately 0.18 V which suggests the films rest in a slightly oxidized state, likely due to surface defects. Annealing under oxygen or hydrogen may respectively oxidize or reduce surface sites during the annealing process. Measuring the $V_{OC}$ and collecting CV for films annealed under oxygen vs hydrogen could lead to interesting deviations in the electrochemical behavior compared to films annealed under inert argon. XPS data could also aid in determining if surface Cu or Cr sites are being oxidized or reduced in the presence of oxygen or hydrogen gas.

***Chapter 4*** discusses the similarities in the band gap of $CuCrO_2$ before and after annealing; however, the absorbance peaks seen in the UV-vis spectra are significantly diminished in the case of annealing the film. While the band gap is comparable, these optical changes could lead to changes in light absorption under illumination. For film fabrication for solar cell application, it would be interesting to supplement the polymers used in previous studies for a conductive polymer. Annealing is done to eliminate polymer from the film due to its insulating properties; furthermore, using a conductive polymer could allow for elimination of the annealing process altogether. Conductive polymers have been previously used to fabricate electrodes, such as polypyrrole, polyaniline, and poly(p-phenylene vinylene).[30–32] However, due to differences in solubility as well as the need for ozone treatment to improve device performance, paste and thin film fabrication methods would need to be modified accordingly.[33,34]

### *5.5 Electrolyte Sources*

The use of $Li^+$ ion batteries has been commercialized and readily available for use in electronic devices and electric vehicles due to its high energy density, playing a vital role in energy storage demands.[35] However, an interest in fabricating ion battery alternatives has increased due to the limited supply of lithium, high manufacturing costs, and flammability which can be hazardous. Some alternative ion sources include abundant alkali metals such as $Na^+$ and $K^+$, divalent alkaline metals such as $Mg^{2+}$, and 3d transition metals such as $Zn^{2+}$ as previously discussed in ***Chapter 2***.[27,35–37] These alternatives are abundant and low cost in addition to being less hazardous compared to their $Li^+$ counterpart.

Preliminary CV was collected to compare the electrochemical redox activity of $CuCrO_2$ in the presence of $Li^+$ to that of $Na^+$ (**Figure 5.5**). As seen in **Figure 5.5a**, there is considerable faradaic current observed for the redox event in the presence of $Na^+$, comparable to what is seen in $Li^+$. This shift where $E_{1/2} = -0.88$ V in $Na^+$ is likely attributed to the differences in ion size where the ionic size of $Li^+$ vs $Na^+$ are 76 and 102 pm, respectively (refer to **Table S5.14** for cation radii size and charge data). The observed current is predicted to be a $Cu^{2+/+}$ redox event based on electrochemical behavior of $CuCrO_2$ and XPS results discussed in ***Chapter 4***, but XPS could be conducted after holding at potentials outside the range of oxidation and reduction events to confirm this consistency.

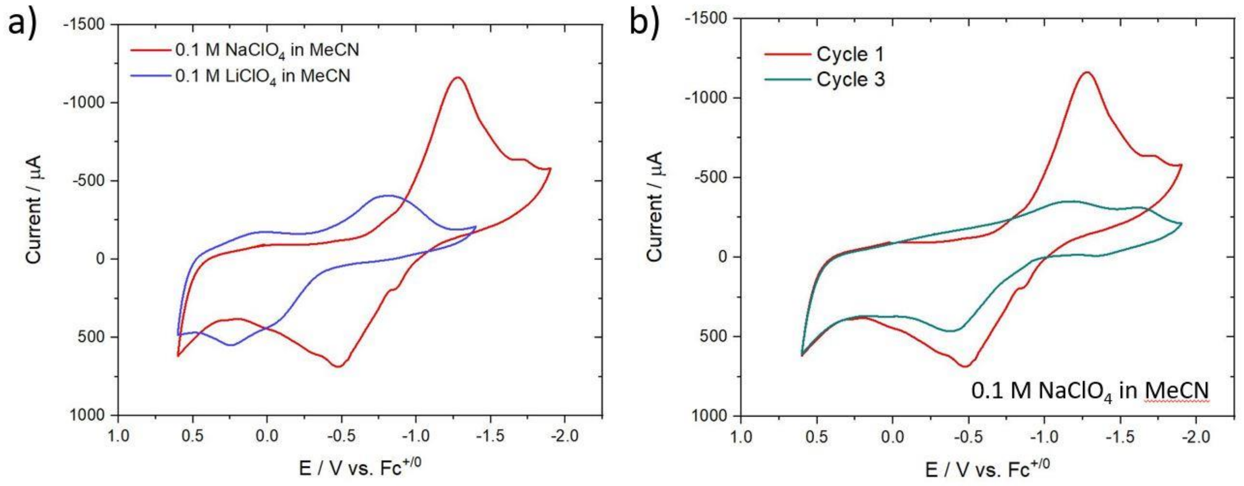

**Figure 5.5. a)** Cycle 1 of $CuCrO_2$ thin films in 0.1 M $NaClO_4$ vs 0.1 M $LiClO_4$ in MeCN at a 10 mV/s scan rate. **b)** A comparison of cycle 1 vs cycle 3 of $CuCrO_2$ CVs in 0.1 M $NaClO_4$ in MeCN at a 10 mV/s scan rate.

Interestingly, the current observed in the presence of $Na^+$ is higher than when $CuCrO_2$ is in the presence of $Li^+$, but the degradation during cycling occurs at a quicker rate as seen in **Figure 5.5b**. This could be due to the increased size of $Na^+$ ions; the ability of $Na^+$ ions to deintercalate out of the film is likely less facile than that of $Li^+$. Additional causes could be increased stress due to the ion size in the film's surface alongside $Cu^{2+}$ sites. Doping $CuCrO_2$ with $Ti^{4+}$ could aid in improving the increased degradation as previously discussed in ***Section 6.3.2***. $K^+$ could also be used as a cation source for direct comparison by using 0.1 M $KClO_4$ in MeCN as the electrolyte solution, but the size of $K^+$ is larger than both $Li^+$ and $Na^+$ at 138 pm and is expected to experience similar behavior in that the $E_{1/2}$ would shift toward a more negative potential and the degradation over the course of cycling would worsen. Furthermore, $Ti^{4+}$ doping or synthetic lithiation could be used to improve the stability of $CuCrO_2$, making the use of these electrolyte sources more practical for alternative ion battery applications.

Divalent and trivalent cation sources could also be studied as alternatives to $Li^+$. In the case of using divalent cation sources, $Mg^{2+}$ and $Zn^{2+}$ both have comparable ion sizes to $Li^+$ with radii of 72 and 74 pm, respectively. The similarities in size would permit plausible intercalation or surface reactivity as that of $Li^+$. However, twice the amount of $Cu^+$ sites adjacent to vacancies would need to oxidize to $Cu^{2+}$ in order to charge balance the lithiated cations which could lead to problematic steric strain. $Ti^{4+}$ doping could aid in alleviating the amount of steric strain in that less $Cu^{2+}$ sites would need to be present for charge compensation of $Cu^+$ vacancies, but the degree of stability is unknown. Utilizing 0.1 M $Mg(ClO_4)_2$ and 0.1 M $Zn(ClO_4)_2$ in MeCN as electrolyte solutions to study both undoped and $Ti^{4+}$ doped $CuCrO_2$ films could lead to insight into the effects of degradation. Acid washed films may also maximize the amount of $Cu^+$ vacancies as seen in ***Section 5.3.3.2***, therefore increasing the number of $Cu^+$ sites that could be available for $Cu^{2+}$ conversion as intercalation occurs.

Similar approaches could be used for trivalent cation electrolyte sources, such as $La(ClO_4)_3$ where $La^{3+}$ has a comparable ion radius of 103 pm relative to a $Na^+$ ion. In the case of using 0.1 M $La(ClO_4)_3$ in MeCN as the electrolyte source, it is uncertain whether or not enough $Cu^+$ sites would be available to oxidize for charge compensation. Acid washed films may permit enough vacancies to be present for neighboring $Cu^+$ atoms to accommodate a trivalent cation intercalation event, but it is also plausible that nearby $Cr^{3+}$ sites could oxidize to $Cr^{6+}$ to charge balance $Li^+$ intercalation into the lattice. In this case, only one $Cr^{3+}$ atom would need to be redox active compared to three $Cu^+$ atoms, making the possibility of increased capacity possible. If $Cr^{3+}$ were capable of redox activity during intercalation, $Cu^{2+}$ conversion would be limited, which could help minimize strain during intercalation and stabilize the film. Additionally, if anisotropic delafossite particles have Cr terminated faces as what is seen in $CuGaO_2$ particles in ***Chapter 4*** where the particles favor orientation of the Cr terminated (001) plane parallel to the FTO glass substrate, more Cr coordinated surface sites could be available for surface redox interactions. CV and XPS could again be used to determine whether redox activity in the presence of $La^{3+}$ is possible, and whether or not $Cu^{2+/+}$ or $Cr^{6+/3+}$ is responsible for charge compensation.

### *5.6 Kinetic Considerations*

As previously mentioned, delafossite $CuCrO_2$ exhibits a moderately high capacity. However, the influence of defects on the capacity of these materials is lacking. A key factor contributing to the impediment of the overall performance is likely the rate of lithium intercalation. In previously reported studies on lithium intercalation into anatase $TiO_2$, the $Ti^{4+/3+}$ coupled redox events were found to be kinetically hindered, determined by the potential dependence on the rate of insertion and extraction.[38] If delafossite $CuCrO_2$ also exhibits $Cu^{2+/+}$ coupled redox events which are kinetically hindered, or $Cr^{6+/3+}$ if trivalent cation intercalation successfully permits redox activity of $Cr^{3+}$ sites, it may aid in understanding the complex kinetics of the system. Potential dependence studies can be conducted by constructing Anson plots at critical potential steps before and after redox events take place as previously shown in ***Chapter 4*** where potentials were held within the diffusional window determined by CV. These same experiments can be done isothermally using a range of temperatures to determine whether or not ion diffusion is thermally activated.[38]

Anson plots can be used to calculate the slope and provide a corresponding diffusion coefficient. Using the equation $D = D_0 e^{\frac{-E_a}{kT}}$, activation energies for each system can be calculated where D is the diffusion coefficient, $D_0$ is the preexponential factor, $E_a$ is the activation energy, k is the Boltzmann constant, and T is the absolute temperature. Temperature dependent studies to determine differences in activation energies for $CuCrO_2$ with differences in morphology and vacancy concentrations can be insightful with respect to determining optimal conditions for enhanced performance. Previous studies have revealed differences in activation energies for crystalline and amorphous transition metal oxide materials, where amorphous materials exhibit lower activation energies.[39] Due to the enhanced performance seen in ***Section 5.3.3.2*** where $CuCrO_2$ was washed in pH 1 solution, in addition to the loss in crystallinity when washing > 96 hours, similar results in the activation energies might be expected. However, studies on a range of vacancy concentrations and their impact on the activation energy may be useful in explaining results obtained in experimental data.

The kinetics of the system can also be studied in more detail using CV scan rate dependence studies. In efforts to understand the kinetic limitations of the electrochemical system of synthetically optimized $CuCrO_2$ films in 0.1 M $LiClO_4$ in MeCN, a preliminary cyclic voltammogram was taken at various scan rate intervals between 450 – 5 mV/s. **Figure 5.6a** shows the resulting CVs. The peak current was obtained prior to normalization using the reductive peak maxima near 0 V. This peak was selected for further analysis due to its minimal observed degradation over the course of cycling relative to the other peaks in the CV. These values were used to generate a log i-*v* plot, as seen in **Figure 5.6b**.

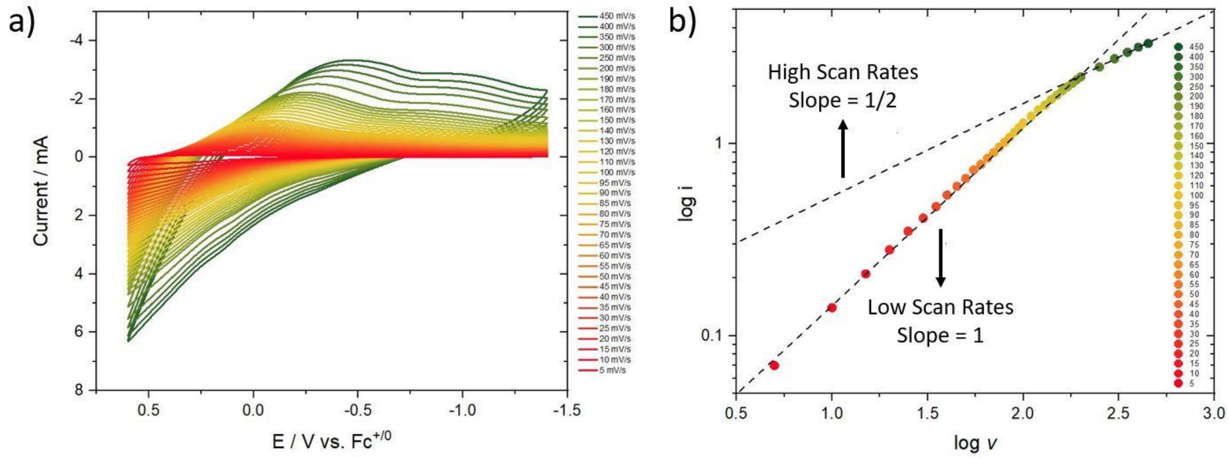

**Figure 5.6. a)** CVs of optimized $CuCrO_2$ thin films from 450 mV/s to 5 mV/s. **b)** Log i-*v* plot for the 0 V reduction peak observed in the scan rate dependence CVs. The initial scan rate used was 450 mV/s and went to lower scan rates.

A slope of ½ can be seen between high scan rates of 200 – 450 mV/s which is attributed to ion diffusion being the rate limiting step. At scan rates lower than 200 mV/s, the slope of the line is equal to 1 which suggests that the film is able to behave as a thin film or surface process that is not diffusion controlled. Because the scan rate dependence study began at high scan rates and proceeded to low scan rates, one possibility is that the lithium ions are intercalating into the film and are kinetically limiting the electrochemical redox processes. However, after cycling multiple times, the irreversibility of the ion deintercalation could lead to a lack in diffusion, meaning at scan rates lower than 200 mV/s no more ions are intercalating into the film. This could lead to kinetic limitations due to other phenomena. In order to further examine the kinetics of the system and how much impact the irreversibility has on diffusion, additional scan rate dependence experiments can be conducted after $CuCrO_2$ is tuned to prevent degradation, either by means of $Ti^{4+}$ doping or synthetic lithiation, as previously discussed. In the event that film degradation leads to a slope of 1 at low scan rates, conducting this experiment with more stable films could result in a slope of ½ extending to slower scan rates.

### *5.7 Summarizing Thoughts*

Delafossite $CuCrO_2$ is a promising material for both applications as a cathode in ion batteries, as well as a hole transport material in solar cell devices, due to its wide band gap and moderately high reported conductivity.[13,22,40,41] We successfully report an optimized synthetic route to hydrothermally growing $CuCrO_2$ nanocrystals with minimal impurities, while also defining the role of $Cr^{3+}$ as a reducing agent in oxidizing $Cu^{2+}$ precursors. Structural and electrochemical characterization was extensively done to understand the fundamental $Cu^{2+/+}$ redox process and the electrochemical dependence of $Li^+$ in electrolyte solution. Morphological comparisons were done between $CuCrO_2$ and $CuGaO_2$ to determine smaller nanoparticle size and isotropy leads to improvements in observed current. Degradation studies were done to better understand the irreversibility of the system seen through multiple cycling CV and chronopotentiometry experiments. Finally, inducing $Cu^+$ vacancies by washing $CuCrO_2$ powders in pH 1 solution over time was shown to optimize the cycling efficiency of the film compared to films which were base washed. Washing for 96 hours optimized the amount of charge capacity observed by chronopotentiometry as well as maximizing the current observed in CV. Through continuing research and improving the stability of the film during electrochemical exposure, this material is a viable candidate for future solar energy conversion and storage applications.

### *5.8 Supporting Information*

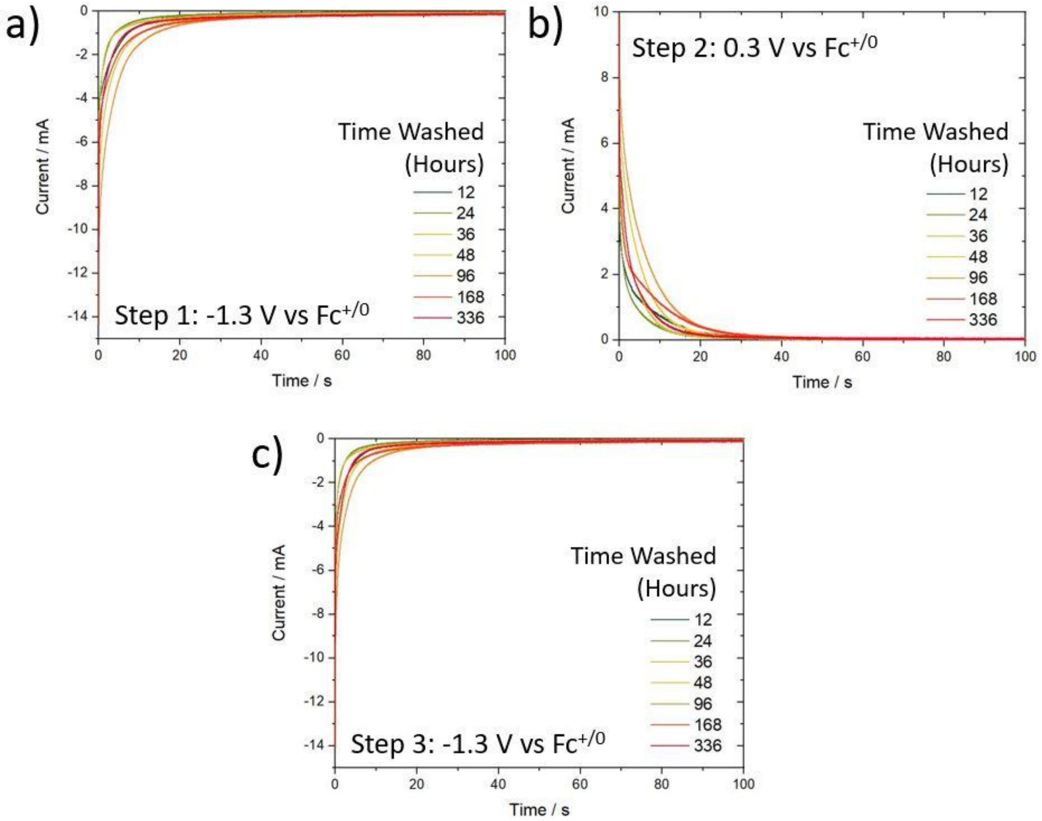

**Figure S5.1.** Amperometric IT curves used to integrate and construct Anson plots for films made using $CuCrO_2$ powder washed in acidic solution for 12 – 336 hours, all in 0.1 M $LiClO_4$ in MeCN holding 0.1 mA. A 3 step experiment was conducted in which the potential was held at **a)** -1.3 V vs $Fc^{+/0}$ for 100 seconds (step 1), **b)** 0.3 V vs $Fc^{+/0}$ for 100 seconds (step 2), and **c)** -1.3 V vs $Fc^{+/0}$ for 100 seconds (step 3).

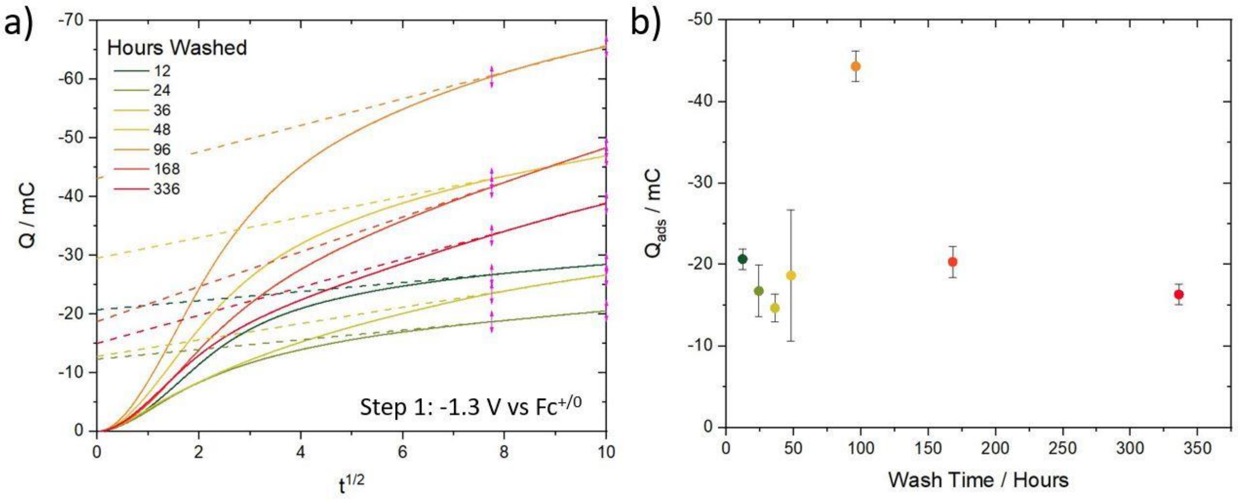

**Figure S5.2. a)** Anson plots constructed from integrated amperometric IT curves from films made using $CuCrO_2$ powder washed in acidic solution for 12 – 336 hours, all in 0.1 M $LiClO_4$ in MeCN holding 0.1 mA. Each step was held at the fixed potential -1.3 V vs $Fc^{+/0}$ for 100 seconds (Step 1). **b)** Qads plotted as a function of time washed in acidic solution.

**Table S5.1.** Diffusion coefficients and adsorption charges determined from Anson plot step 1 where the potential was held at -1.3 V vs $Fc^{+/0}$ for 100 seconds (Step 1).

| Wash Time | Diffusion Coefficient / $cm^2s^{-1}$ | Adsorption Charge Q / mC |
|---|---|---|
| 12 | $1.7 \times 10^{-15}$ | -21 ± 1.3 |
| 24 | $2.0 \times 10^{-15}$ | -17 ± 3.2 |
| 36 | $5.6 \times 10^{-15}$ | -15 ± 1.7 |
| 48 | $9.3 \times 10^{-15}$ | -19 ± 8.1 |
| 96 | $1.5 \times 10^{-14}$ | -44 ± 1.9 |
| 168 | $2.6 \times 10^{-14}$ | -20 ± 1.9 |
| 336 | $1.7 \times 10^{-14}$ | -16 ± 1.3 |

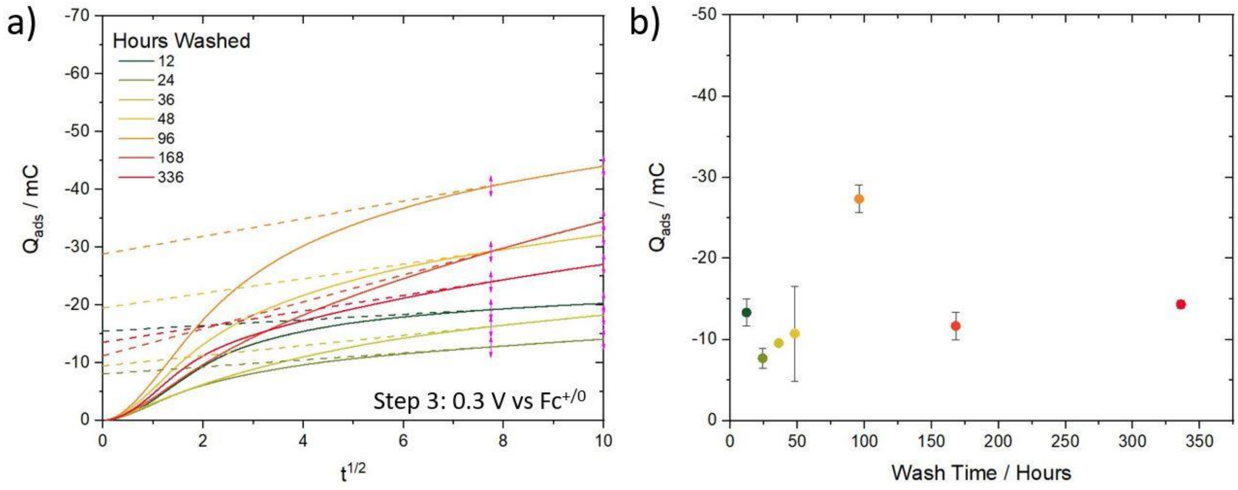

**Figure S5.3. a)** Anson plots constructed from integrated amperometric IT curves from films made using $CuCrO_2$ powder washed in acidic solution for 12 – 336 hours, all in 0.1 M $LiClO_4$ in MeCN holding 0.1 mA. Each step was held at the fixed potential -1.3 V vs $Fc^{+/0}$ for 100 seconds (Step 3). **b)** $Q_{ads}$ plotted as a function of time washed in acidic solution.

**Table S5.2.** Diffusion coefficients and adsorption charges determined from Anson plot step 3 where the potential was held at -1.3 V vs $Fc^{+/0}$ for 100 seconds (Step 3).

| Wash Time | Diffusion Coefficient / $cm^2s^{-1}$ | Adsorption Charge Q / mC |
|---|---|---|
| 12 | $6.7 \times 10^{-16}$ | -13 ± 1.7 |
| 24 | $1.1 \times 10^{-15}$ | -7.7 ± 1.2 |
| 36 | $2.2 \times 10^{-15}$ | -9.6 ± 0.2 |
| 48 | $4.6 \times 10^{-15}$ | -11 ± 5.9 |
| 96 | $6.7 \times 10^{-15}$ | -27 ± 1.7 |
| 168 | $1.6 \times 10^{-14}$ | -12 ± 1.7 |
| 336 | $5.3 \times 10^{-15}$ | -14 ± 0.5 |

**Table S5.3.** Calculated charge and discharge Q and % cycling efficiencies from $CuCrO_2$ chronopotentiograms washed in acidic solution for 12 hours.

| Cycle # | Charge Q (mC) | Discharge Q (mC) | % Cycling efficiency $(\frac{\text{Disharge Q}}{\text{Charge Q}}) * 100$ |
|---|---|---|---|
| 2 | 40 | 42 | 105 |
| 3 | 39 | 39 | 101 |
| 4 | 37 | 35 | 94 |
| 5 | 33 | 30 | 93 |
| 6 | 29 | 27 | 91 |
| 7 | 26 | 24 | 90 |
| 8 | 23 | 21 | 90 |
| 9 | 21 | 19 | 90 |
| 10 | 19 | 17 | 91 |

**Table S5.4.** Calculated charge and discharge Q and % cycling efficiencies from $CuCrO_2$ chronopotentiograms washed in acidic solution for 24 hours.

| Cycle # | Charge Q (mC) | Discharge Q (mC) | % Cycling efficiency $(\frac{\text{Disharge Q}}{\text{Charge Q}}) * 100$ |
|---|---|---|---|
| 2 | 34 | 38 | 113 |
| 3 | 35 | 36 | 104 |
| 4 | 34 | 34 | 101 |
| 5 | 33 | 32 | 99. |
| 6 | 31 | 29 | 95 |
| 7 | 28 | 25 | 89 |
| 8 | 24 | 22 | 92 |
| 9 | 22 | 20 | 94 |
| 10 | 20 | 19 | 95 |

**Table S5.5.** Calculated charge and discharge Q and % cycling efficiencies from $CuCrO_2$ chronopotentiograms washed in acidic solution for 36 hours.

| Cycle # | Charge Q (mC) | Discharge Q (mC) | % Cycling efficiency $(\frac{\text{Disharge Q}}{\text{Charge Q}}) * 100$ |
|---|---|---|---|
| 2 | 37 | 40 | 108 |
| 3 | 33 | 34 | 102 |
| 4 | 29 | 28 | 98 |
| 5 | 24 | 23 | 96 |
| 6 | 21 | 20 | 95 |
| 7 | 18 | 17 | 95 |
| 8 | 16 | 15 | 96 |
| 9 | 14 | 14 | 96 |
| 10 | 13 | 12 | 97 |

**Table S5.6.** Calculated charge and discharge Q and % cycling efficiencies from $CuCrO_2$ chronopotentiograms washed in acidic solution for 48 hours.

| Cycle # | Charge Q (mC) | Discharge Q (mC) | % Cycling efficiency $(\frac{\text{Disharge Q}}{\text{Charge Q}}) * 100$ |
|---|---|---|---|
| 2 | 73 | 90 | 124 |
| 3 | 72 | 80 | 110 |
| 4 | 66 | 71 | 108 |
| 5 | 60 | 63 | 104 |
| 6 | 56 | 57 | 102 |
| 7 | 51 | 50 | 99 |
| 8 | 46 | 45 | 97 |
| 9 | 41 | 40 | 98 |
| 10 | 38 | 37 | 97 |

**Table S5.7.** Calculated charge and discharge Q and % cycling efficiencies from $CuCrO_2$ chronopotentiograms washed in acidic solution for 96 hours.

| Cycle # | Charge Q (mC) | Discharge Q (mC) | % Cycling efficiency $(\frac{\text{Disharge Q}}{\text{Charge Q}}) * 100$ |
|---|---|---|---|
| 2 | 134 | 143 | 107 |
| 3 | 125 | 124 | 99 |
| 4 | 117 | 110 | 95 |
| 5 | 107 | 98 | 92 |
| 6 | 96 | 87 | 90 |
| 7 | 86 | 77 | 89 |
| 8 | 78 | 68 | 88 |
| 9 | 70 | 61 | 88 |
| 10 | 63 | 56 | 89 |

**Table S5.8.** Calculated charge and discharge Q and % cycling efficiencies from $CuCrO_2$ chronopotentiograms washed in acidic solution for 168 hours.

| Cycle # | Charge Q (mC) | Discharge Q (mC) | % Cycling efficiency $(\frac{\text{Disharge Q}}{\text{Charge Q}}) * 100$ |
|---|---|---|---|
| 2 | 205 | 119 | 58 |
| 3 | 120 | 88 | 73 |
| 4 | 90 | 70 | 77 |
| 5 | 72 | 57 | 79 |
| 6 | 59 | 49 | 82 |
| 7 | 51 | 42 | 83 |
| 8 | 45 | 39 | 86 |
| 9 | 41 | 27 | 67 |
| 10 | 30 | 24 | 80 |

**Table S5.9.** Calculated charge and discharge Q and % cycling efficiencies from $CuCrO_2$ chronopotentiograms washed in acidic solution for 336 hours.

| Cycle # | Charge Q (mC) | Discharge Q (mC) | % Cycling efficiency $(\frac{\text{Disharge Q}}{\text{Charge Q}}) * 100$ |
|---|---|---|---|
| 2 | 44 | 52 | 117 |
| 3 | 47 | 49 | 105 |
| 4 | 48 | 47 | 98 |
| 5 | 47 | 45 | 96 |
| 6 | 44 | 41 | 92 |
| 7 | 41 | 37 | 90 |
| 8 | 38 | 33 | 89 |
| 9 | 34 | 30 | 88 |
| 10 | 31 | 27 | 88 |

**Table S5.10.** Calculated charge and discharge capacity from $CuCrO_2$ chronopotentiograms washed in acidic solution for 12 and 24 hours.

| | 12 Hours | | 24 Hours | |
|---|---|---|---|---|
| Cycle # | Charge Capacity $(\frac{\text{mAh}}{\text{g}})$ | Discharge Capacity $(\frac{\text{mAh}}{\text{g}})$ | Charge Capacity $(\frac{\text{mAh}}{\text{g}})$ | Discharge Capacity $(\frac{\text{mAh}}{\text{g}})$ |
| 2 | 21 | 21 | 17 | 20 |
| 3 | 20 | 20 | 18 | 19 |
| 4 | 19 | 18 | 18 | 18 |
| 5 | 17 | 16 | 17 | 17 |
| 6 | 15 | 14 | 16 | 15 |
| 7 | 14 | 12 | 14 | 13 |
| 8 | 12 | 11 | 12 | 12 |
| 9 | 11 | 10 | 11 | 10 |
| 10 | 9.7 | 8.8 | 10 | 9.7 |

**Table S5.11.** Calculated charge and discharge capacity from $CuCrO_2$ chronopotentiograms washed in acidic solution for 36 and 48 hours.

| | 36 Hours | | 48 Hours | |
|---|---|---|---|---|
| Cycle # | Charge Capacity $(\frac{\text{mAh}}{\text{g}})$ | Discharge Capacity $(\frac{\text{mAh}}{\text{g}})$ | Charge Capacity $(\frac{\text{mAh}}{\text{g}})$ | Discharge Capacity $(\frac{\text{mAh}}{\text{g}})$ |
| 2 | 19 | 21 | 38 | 47 |
| 3 | 17 | 17 | 37 | 41 |
| 4 | 15 | 15 | 34 | 37 |
| 5 | 13 | 12 | 31 | 33 |
| 6 | 11 | 10 | 29 | 29 |
| 7 | 9.3 | 8.9 | 27 | 26 |
| 8 | 8.2 | 7.9 | 24 | 23 |
| 9 | 7.3 | 7.0 | 21 | 21 |
| 10 | 6.5 | 6.3 | 20 | 19 |

**Table S5.12.** Calculated charge and discharge capacity from $CuCrO_2$ chronopotentiograms washed in acidic solution for 96 and 168 hours.

| | 96 Hours | | 168 Hours | |
|---|---|---|---|---|
| Cycle # | Charge Capacity $(\frac{\text{mAh}}{\text{g}})$ | Discharge Capacity $(\frac{\text{mAh}}{\text{g}})$ | Charge Capacity $(\frac{\text{mAh}}{\text{g}})$ | Discharge Capacity $(\frac{\text{mAh}}{\text{g}})$ |
| 2 | 70 | 74 | 106 | 62 |
| 3 | 65 | 64 | 62 | 46 |
| 4 | 60 | 57 | 47 | 36 |
| 5 | 55 | 51 | 37 | 30 |
| 6 | 50 | 45 | 31 | 25 |
| 7 | 45 | 30 | 27 | 22 |
| 8 | 40 | 35 | 23 | 20 |
| 9 | 36 | 32 | 21 | 14 |
| 10 | 33 | 29 | 16 | 12 |

**Table S5.13.** Calculated charge and discharge capacity from $CuCrO_2$ chronopotentiograms washed in acidic solution for 336 hours.

| | 336 Hours | |
|---|---|---|
| Cycle # | Charge Capacity ($\frac{mAh}{g}$) | Discharge Capacity ($\frac{mAh}{g}$) |
| 2 | 23 | 27 |
| 3 | 24 | 26 |
| 4 | 25 | 24 |
| 5 | 24 | 23 |
| 6 | 23 | 21 |
| 7 | 21 | 19 |
| 8 | 20 | 17 |
| 9 | 18 | 16 |
| 10 | 16 | 14 |

**Table S5.14.** Electrolyte sources and their respective cation charges in ascending order of ion radius size in pm.[42,43]

| Electrolyte Sources | Ion radius (pm) | Ion Charge |
|---|---|---|
| $Al(ClO4)_3$ | 53.5 | 3 |
| $Ga(ClO_4)_3$ | 62 | 3 |
| $Ni\ (ClO_4)_2$ | 69 | 2 |
| $Mg(ClO_4)_2$ | 72 | 2 |
| $Cu(ClO_4)_2$ | 73 | 2 |
| $Zn(ClO_4)_2$ | 74 | 2 |
| $LiClO_4$ | 76 | 1 |
| $Fe(ClO_4)_2$ | 78 | 2 |
| $Mn(ClO_4)_2$ | 83 | 2 |
| $Ca(ClO_4)_2$ | 100 | 2 |
| $NaClO_4$ | 102 | 1 |
| $La(ClO_4)_3$ | 103 | 3 |
| $KClO_4$ | 138 | 1 |
| $TMA(ClO_4)$ | 322 | 1 |
| $TBA\ (ClO_4)$ | 494 | 1 |

## *5.9 References*

1. Shin, D.; Foord, J. S.; Egdell, R. G.; Walsh, A. Electronic Structure of CuCrO2 Thin Films Grown on $Al_2O_3$ (001) by Oxygen Plasma Assisted Molecular Beam Epitaxy. *J. Appl. Phys.* **2012**, *112* (11), 113718.
2. Wang, W.; Banerjee, S.; Jia, S.; Steigerwald, M. L.; Herman, I. P. Ligand Control of Growth, Morphology, and Capping Structure of Colloidal CdSe Nanorods. *Chem. Mater.* **2007**, *19* (10), 2573–2580.
3. Adireddy, S.; Lin, C.; Palshin, V.; Dong, Y.; Cole, R.; Caruntu, G. Size-Controlled Synthesis of Quasi-Monodisperse Transition-Metal Ferrite Nanocrystals in Fatty Alcohol Solutions. *J. Phys. Chem. C* **2009**, *113* (49), 20800–20811.
4. Hu, J.; Chen, Z.; Li, M.; Zhou, X.; Lu, H. Amine-Capped Co Nanoparticles for Highly Efficient Dehydrogenation of Ammonia Borane. *ACS Appl. Mater. Interfaces* **2014**, *6* (15), 13191–13200.
5. Li, B.; Chen, J.; Han, L.; Bai, Y.; Fan, Q.; Wu, C.; Wang, X.; Lee, M.; Xin, H. L.; Han, Z.; Yin, Y. Ligand-Assisted Solid-State Transformation of Nanoparticles. *Chem. Mater.* **2020**, *32* (7), 3271–3277.
6. Garcia-Gutierrez, D. F.; Hernandez-Casillas, L. P.; Cappellari, M. V.; Fungo, F.; Martínez-Guerra, E.; García-Gutiérrez, D. I. Influence of the Capping Ligand on the Band Gap and Electronic Levels of PbS Nanoparticles through Surface Atomistic Arrangement Determination. *ACS Omega* **2018**, *3* (1), 393–405.
7. Folkman, S. J.; Zhou, M.; Nicki, M.; Finke, R. G. Alcohol Solvent Effects in the Synthesis of $Co_3O_4$ Metal-Oxide Nanoparticles: Disproof of a Surface-Ligand Thermodynamic Effect En Route to Alternative Kinetic and Thermodynamic Explanations. *Inorg. Chem.* **2018**, *57* (3), 1517–1526.
8. Nasser Abdelhamid, H.; Kumaran, S.; Wu, H.-F. One-Pot Synthesis of $CuFeO_2$ Nanoparticles Capped with Glycerol and Proteomic Analysis of Their Nanocytotoxicity against Fungi. *RSC Advances* **2016**, *6* (100), 97629–97635.
9. Ghosh Chaudhuri, R.; Paria, S. Core/Shell Nanoparticles: Classes, Properties, Synthesis Mechanisms, Characterization, and Applications. *Chem. Rev.* **2012**, *112* (4), 2373–2433.
10. Ma, J.; Li, W.; Morgan, B. J.; Światowska, J.; Baddour-Hadjean, R.; Body, M.; Legein, C.; Borkiewicz, O. J.; Leclerc, S.; Groult, H.; Lantelme, F.; Laberty-Robert, C.; Dambournet, D. Lithium Intercalation in Anatase Titanium Vacancies and the Role of Local Anionic Environment. *Chem. Mater.* **2018**, *30* (9), 3078–3089.
11. Jiang, T.; Li, X.; Bujoli-Doeuff, M.; Gautron, E.; Cario, L.; Jobic, S.; Gautier, R. Modulation of Defects in Semiconductors by Facile and Controllable Reduction: The Case of p-Type $CuCrO_2$ Nanoparticles. *Inorg. Chem.* **2016**, *55* (15), 7729–7733.
12. Lunca Popa, P.; Crêpellière, J.; Nukala, P.; Leturcq, R.; Lenoble, D. Invisible Electronics: Metastable Cu-Vacancies Chain Defects for Highly Conductive p-Type Transparent Oxide. *Appl. Mater. Today* **2017**, *9*, 184–191.
13. Scanlon, D. O.; Watson, G. W. Understanding the P-Type Defect Chemistry of $CuCrO_2$. *J. Mater. Chem.* **2011**, *21* (11), 3655.
14. Potiron, E.; Le Gal La Salle, A.; Sarciaux, S.; Piffard, Y.; Guyomard, D. E-$V_2O_5$: Relationships between Synthesis Conditions, Material Characteristics and Lithium Intercalation Behavior. *J. Power Sources* **1999**, *81–82*, 666–669.

15. Swider-Lyons, K. Improved Lithium Capacity of Defective $V_2O_5$ Materials. *Solid State Ionics* **2002**, *152–153*, 99–104.
16. Lunca-Popa, P.; Afonso, J.; Grysan, P.; Crêpellière, J.; Leturcq, R.; Lenoble, D. Tuning the Electrical Properties of the P-Type Transparent Conducting Oxide $Cu_{1-x}Cr_{1+x}O_2$ by Controlled Annealing. *Sci. Rep.* **2018**, *8* (1), 7216.
17. Xiong, D.; Xu, Z.; Zeng, X.; Zhang, W.; Chen, W.; Xu, X.; Wang, M.; Cheng, Y.-B. Hydrothermal Synthesis of Ultrasmall $CuCrO_2$ Nanocrystal Alternatives to NiO Nanoparticles in Efficient P-Type Dye-Sensitized Solar Cells. *J. Mater. Chem.* **2012**, *22* (47), 24760.
18. Amami, M.; Smari, S.; Tayeb, K.; Strobel, P.; Abdelhamid, B. S. Cationic Doping Effect on the Structural, Magnetic and Spectroscopic Properties of Delafossite Oxides $CuCr_{1-x}(Sc,Mg)_xO_2$. *Mater. Chem. Phys.* **2011**, *128*, 298–302.
19. Daou, R.; Frésard, R.; Eyert, V.; Hébert, S.; Maignan, A. Unconventional Aspects of Electronic Transport in Delafossite Oxides. *Sci. Technol. Adv. Mater.* **2017**, *18* (1), 919–938.
20. Elkhouni, T.; Amami, M.; Strobel, P.; Salah, A. B. Structural and Magnetic Properties of Substituted Delafossite-Type Oxides $CuCr_{1-x}Sc_xO_2$. *World J. Condens. Matter Phys.* **2013**, *3* (1), 1–8.
21. Manickam, R.; Yesuraj, J.; Biswas, K. Doped $CuCrO_2$: A Possible Material for Supercapacitor Applications. *Mater. Sci. Semicond. Process.* **2020**, *109*, 104928.
22. Wang, P.; Li, P.; Yi, T.-F.; Lin, X.; Zhu, Y.-R.; Shao, L.; Shui, M.; Long, N.; Shu, J. Fabrication and Electrochemical Properties of $CuCrO_2$ Anode Obtained by a Sol–Gel Method. *Ceram. Int.* **2015**, *41*.
23. Zhu, X.-D.; Tian, J.; Le, S.-R.; Chen, J.-R.; Sun, K.-N. Enhanced Electrochemical Performances of $CuCrO_2$–CNTs Nanocomposites Anodes by in-Situ Hydrothermal Synthesis for Lithium Ion Batteries. *Mater. Lett.* **2013**, *107*, 147–149.
24. Fu, G.; Wen, X.; Xi, S.; Chen, Z.; Li, W.; Zhang, J.-Y.; Tadich, A.; Wu, R.; Qi, D.-C.; Du, Y.; Cheng, J.; Zhang, K. H. L. Tuning the Electronic Structure of NiO via Li Doping for the Fast Oxygen Evolution Reaction. *Chem. Mater.* **2019**, *31* (2), 419–428.
25. Zhao, T.; Shu, H.; Shen, Z.; Hu, H.; Wang, J.; Chen, X. Electrochemical Lithiation Mechanism of Two-Dimensional Transition-Metal Dichalcogenide Anode Materials: Intercalation versus Conversion Reactions. *J. Phys. Chem. C* **2019**, *123* (4), 2139–2146.
26. Bredar, A. R. C.; Blanchet, M. D.; Comes, R. B.; Farnum, B. H. Evidence and Influence of Copper Vacancies in P-Type $CuGaO_2$ Mesoporous Films. *ACS Appl. Energy Mater.* **2019**, *2* (1), 19–28.
27. Komaba, S.; Takei, C.; Nakayama, T.; Ogata, A.; Yabuuchi, N. Electrochemical Intercalation Activity of Layered $NaCrO_2$ vs. $LiCrO_2$. *Electrochem. Commun.* **2010**, *12* (3), 355–358.
28. Croft, W. J.; Tombs, N. C.; England, R. E. Crystallographic Data for Pure Crystalline Silver Ferrite. *Acta Cryst* **1964**, *17* (3), 313–313.
29. Shannon, R. D.; Rogers, D. B.; Prewitt, C. T. Chemistry of Noble Metal Oxides. I. Syntheses and Properties of $ABO_2$ Delafossite Compounds. *Inorg. Chem.* **1971**, *10* (4), 713–718.
30. Wang, Z.; Cui, H.; Li, S.; Feng, X.; Aghassi-Hagmann, J.; Azizian, S.; Levkin, P. A. Facile Approach to Conductive Polymer Microelectrodes for Flexible Electronics. *ACS Appl. Mater. Interfaces* **2021**, *13* (18), 21661–21668.

31. Chen, Z.; Chen, Y.; Zhao, Y.; Qiu, F.; Jiang, K.; Huang, S.; Ke, C.; Zhu, J.; Tranca, D.; Zhuang, X. B/N-Enriched Semi-Conductive Polymer Film for Micro-Supercapacitors with AC Line-Filtering Performance. *Langmuir* **2021**, *37* (7), 2523–2531.
32. Wang, J.; Bard, A. J. On the Absence of a Diffuse Double Layer at Electronically Conductive Polymer Film Electrodes. Direct Evidence by Atomic Force Microscopy of Complete Charge Compensation. *J. Am. Chem. Soc.* **2001**, *123* (3), 498–499.
33. Nagata, T.; Oh, S.; Chikyow, T.; Wakayama, Y. Effect of UV–Ozone Treatment on Electrical Properties of PEDOT:PSS Film. *Org. Electron.* **2011**, *12* (2), 279–284.
34. Lee, W.; Song, M.; Park, S.; Nam, S.; Seo, J.; Kim, H.; Kim, Y. Acidity-Controlled Conducting Polymer Films for Organic Thermoelectric Devices with Horizontal and Vertical Architectures. *Sci. Rep.* **2016**, *6* (1), 33795.
35. Wu, W.; Sun, Q. Screening Topological Quantum Materials for Na-Ion Battery Cathode. *ACS Materials Lett.* **2022**, *4* (1), 175–180.
36. Alfaruqi, M. H.; Mathew, V.; Song, J.; Kim, S.; Islam, S.; Pham, D. T.; Jo, J.; Kim, S.; Baboo, J. P.; Xiu, Z.; Lee, K.-S.; Sun, Y.-K.; Kim, J. Electrochemical Zinc Intercalation in Lithium Vanadium Oxide: A High-Capacity Zinc-Ion Battery Cathode. *Chem. Mater.* **2017**, *29* (4), 1684–1694.
37. Truong, Q. D.; Kempaiah Devaraju, M.; Tran, P. D.; Gambe, Y.; Nayuki, K.; Sasaki, Y.; Honma, I. Unravelling the Surface Structure of $MgMn_2O_4$ Cathode Materials for Rechargeable Magnesium-Ion Battery. *Chem. Mater.* **2017**, *29* (15), 6245–6251.
38. Lindström, H.; Södergren, S.; Solbrand, A.; Rensmo, H.; Hjelm, J.; Hagfeldt, A.; Lindquist, S.-E. $Li^+$ Ion Insertion in $TiO_2$ (Anatase). 1. Chronoamperometry on CVD Films and Nanoporous Films. *J. Phys. Chem. B* **1997**, *101* (39), 7710–7716.
39. Randin, J.-P. Proton Diffusion in Tungsten Trioxide Thin Films. *J. Electrochem. Soc.* **1982**, *129* (10), 2349.
40. Bottiglieri, L.; Resende, J.; Weber, M.; Chaix-Pluchery, O.; Jiménez, C.; Deschanvres, J.-L. Out of Stoichiometry $CuCrO_2$ Films as a Promising P-Type TCO for Transparent Electronics. *Mater. Adv.* **2021**, *2* (14), 4721–4732.
41. Zhu, X.-D.; Tian, J.; Le, S.-R.; Zhang, N.-Q.; Sun, K.-N. Improved Electrochemical Performance of $CuCrO_2$ Anode with CNTs as Conductive Agent for Lithium Ion Batteries. *Mater. Lett.* **2013**, *97*, 113–116.
42. Christianson. 8.2: Atomic and Ionic Radius. *BU: Chem 103.* Chemistry LibreTexts. **2019**. https://chem.libretexts.org/Courses/Bellarmine_University/BU%3A_Chem_103_(Christianson)
43. Banait, J. S.; Sidhu, K. S.; Walia, J. S. Transference Numbers and Solvation Studies in *n* -Butanol. *Can. J. Chem.* **1984**, *62* (2), 303–305.